UNDRAINED BEHAVIOR OF PLATE ANCHORS

SUBJECTED TO GENERAL LOADING

A Dissertation

by

MING YANG

Submitted to the Office of Graduate Studies of
Texas A&M University
in partial fulfillment of the requirements for the degree of

DOCTOR OF PHILOSOPHY

December 2008

Major Subject: Civil Engineering

UNDRAINED BEHAVIOR OF PLATE ANCHORS

SUBJECTED TO GENERAL LOADING

A Dissertation

by

MING YANG

Submitted to the Office of Graduate Studies of
Texas A&M University
in partial fulfillment of the requirements for the degree of

DOCTOR OF PHILOSOPHY

Approved by:

Co-Chairs of Committee, Charles P. Aubeny
James D. Murff
Committee Members, Robert L. Lytton
Hongbin Zhan
Jun Zhang
Head of Department, David V. Rosowsky

December 2008

Major Subject: Civil Engineering

ABSTRACT

Undrained Behavior of Plate Anchors Subjected to General Loading. (December 2008)

Ming Yang, B.S., Southwest Jiaotong University, China;

M.S., Southwest Jiaotong University, China;

M.S., University of Illinois at Chicago

Co-Chairs of Advisory Committee: Dr. Charles P. Aubeny
Dr. James D. Murff

This study presents a method for predicting the undrained behavior of plate anchors, including out-of-plane loading of simple plates and performance of suction embedded plate anchors (SEPLA). Three dimensional finite element models are used to investigate the behavior of square and rectangular plate anchors under normal loading with eccentricity in any direction. Upper bound analyses are performed for parallel loading and torsion loading. A simple model is then fitted to the FE and upper bound solutions to determine required fitting parameters for both square and rectangular plates. The simple models can, in turn, be used both to predict anchor capacity and as yield surfaces for conducting plastic limit analyses, a method capable of predicting post yield anchor trajectory. The model predictions are shown in reasonably good agreement with the experimental results. For SEPLA, a theoretical model of plastic limit analysis is developed to predict the trajectory during the “keying” process and the ultimate capacity after the “keying” is complete. The predicted results are consistent with relevant known solutions.

ACKNOWLEDGEMENTS

This research was sponsored by ABS Consulting and GEMS, Inc. and their support is gratefully acknowledged.

I would like to express my sincere thanks to my advisors, Dr. Charles Aubeny and Dr. Don Murff, for their invaluable guidance, warm encouragement and suggestions during my Ph.D. study. I am deeply impressed by their knowledge, caring and philosophy of life, which will affect me throughout my life.

I would also like to thank Dr. Robert L. Lytton, Dr. Hongbin Zhan and Dr. Jun Zhang for serving on the advisory committee.

I would like to extend my thanks to all my friends who helped me during my study. Finally, I greatly appreciate my family for their enduring love and support.

TABLE OF CONTENTS

Page

ABSTRACT……iii

ACKNOWLEDGEMENTS……iv

TABLE OF CONTENTS……v

LIST OF FIGURES……..vii

LIST OF TABLES……...xii

CHAPTER

I INTRODUCTION…….....….1

1.1 General……..1
1.1.1 Concepts of Mooring Systems and Plate Anchors……..…….1
1.1.2 Installation of Plate Anchors……5
1.1.3 Issues…….……...7
1.2 Objectives of Research…….…9
1.3 Outline of Research…….10

II THEORETICAL BACKGROUND……..12

2.1 Concepts of Soil Plasticity……...12
2.2 Plastic Limit Analysis……..15
2.2.1 Lower Bound Method…….15
2.2.2 Upper Bound Method…….17
2.2.3 Application of Plastic Limit Analysis to Plate Anchors…….21
2.3 Finite Element Analysis……...23

III OUT-OF-PLANE LOADING ON PLATE ANCHORS……..26

3.1 Idealized Plate Anchors……...26
3.2 Two-dimensional Analyses (In-Plane Loading)……..27
3.2.1 Two-dimensional Finite Element Model……27
3.2.2 Two-dimensional FE Results and Comparisons with Previous Studies…….28
3.3 Three-dimensional Finite Element Analyses……...39

CHAPTER Page

3.3.1 3-D Finite Element Model……..39
3.3.2 3-D Finite Element Results for Square Plate Anchor…….43
3.3.3 3-D Finite Element Results for Rectangular Plate Anchor…….52
3.3.4 Comparison of Model Predictions with Experiment……...61
3.4 Torsion-Parallel Load Interaction…….64
3.4.1 Upper Bound Calculations……...64
3.4.2 Finite Element Verification of Upper Bound Solutions……..70
3.4.3 Extension of Interaction Model to Include Parallel and Torsion Loadings……..76
3.5 Trajectory Prediction……80
3.5.1 Prediction Method……...80
3.5.2 Example Predictions……83

IV PERFORMANCE OF SUCTION EMBEDDED PLATE ANCHORS……...88

4.1 Theoretical Model for Suction Embedded Plate Anchors (SEPLAs)…..88
4.1.1 Plate Anchor Capacity…….89
4.1.2 Anchor Chain Interaction……90
4.1.3 Generalized Plastic Limit Analysis…….93
4.1.4 Suction Embedded Plate Anchor (SEPLA)…….95
4.2 Results of Prediction……...103
4.2.1 SEPLA without Flap……..103
4.2.2 SEPLA with Flap……...108
4.2.3 Comparisons of SEPLA without Flap and with Flap…….....112
4.3 Conclusions……116

V CONCLUSIONS AND RECOMMENDATIONS…….118

5.1 Conclusions…….118
5.2 Recommendations……...120

REFERENCES……...121

APPENDIX…….124

VITA……...142

LIST OF FIGURES

FIGURE Page

1.1 Development of deepwater systems...….....2

1.2 Two main types of mooring systems (Ruinen, 2000)……...……...3

1.3 Typical types of plate anchors...……...……...4

1.4 Schematic of drag embedment installation…...……..…….5

1.5 Schematic of SEPLA installation (Dove et al., 1998)...……..6

1.6 Partial failure of mooring system….....……...8

2.1 Behavior of plasticity for stable materials..……...…….13

2.2 Example of lower bound method (Murff, 2006)...……16

2.3 Dissipation along slip surface (Murff, 2006)...……..19

2.4 Upper bound mechanism for strip plate anchor (O'Neill et al. 2003)…...……21

2.5 Stress and velocity fields for circular plate anchor (Martin and Randolph, 2001)……....23

2.6 Typical finite element mesh (detail on right)...…….24

2.7 Interaction curves in normal-parallel and normal-moment space (bonded).....25

3.1 Schematic of idealized plate anchors……...……..26

3.2 Finite element mesh for plane strain analysis of a plate anchor (L/t = 7)...…..28

3.3 Plate anchor response under normal and parallel load for plane strain conditions..…...…….…30

3.4 Plate anchor response under pure moment for plane strain conditions...……..30

3.5 Interaction surface for normal and parallel loading for plane strain conditions..……32

FIGURE Page

3.6 Interaction surface for normal and moment loading for plane strain conditions...…….…..32

3.7 Interaction surface for parallel and moment loading for plane strain conditions…...……...33

3.8-A Results comparison of FEM and Eq. 3.2 for moment vs. normal load…..…...35

3.8-B Results comparison of FEM and Eq. 3.2 for moment vs. parallel load…….....36

3.8-C Results comparison of FEM and Eq. 3.2 for parallel load vs. normal load…..36

3.9-A Plastic strain contours: initiation of yielding….……...38

3.9-B Plastic strain contours: progression of yielding……..……..38

3.9-C Plastic strain contours- incipient failure.....……..39

3.10 Out-of-plane loading on plate anchor……...40

3.11-A Finite element framework for vertically loaded plate anchor embedded in soil…...…….…42

3.11-B Detailed finite element mesh for 3-D analysis of plate anchor……42

3.12 Upper bound mechanism for circular plate…….…….44

3.13 Square plate anchor response under pure normal load…….45

3.14 Square plate anchor response under pure moment……...45

3.15 Interaction of normal load and moment for square plate anchor…….….48

3.16 Interaction of moments for square plate anchor.……..49

3.17 Multi-axial yield surface for the square plate anchor…….……..51

3.18 Capacity of the square plate anchor vertically loaded with the eccentricity of *e*/*L*…….……52

3.19 Plate anchor response under pure normal load for a rectangular plate (W/L=2)……54

FIGURE Page

3.20 Plate anchor response under pure moment about the long axis for a rectangular plate (W/L = 2)..……55

3.21 Plate anchor response under pure moment about the short axis for a rectangular plate (W/L = 2).……56

3.22 Interaction of normal load and moment for a rectangular plate anchor (W/L = 2)...……...57

3.23 Interaction of two components of the moment for a rectangular plate anchor ($W / L = 2$)..……..58

3.24 Capacity of the rectangular plate anchor loaded eccentrically in various offset directions...……60

3.25-A Comparisons of model predictions and experiment for square plate...……63

3.25-B Comparisons of model predictions and experiment for rectangular plate……63

3.26 Schematic for upper bound calculations.……..64

3.27 Interaction curves of parallel and torsional loads for infinitely thin plates…..68

3.28-A Parallel resistances of the rectangular plate vs. load offset (L/W=1:2)……69

3.28-B Parallel resistance of the rectangular plate vs. load angle (L/W=1:2)……..69

3.29 Plate anchor with buffer zone.……..70

3.30 Comparison of interactions of parallel and torsional loads by FE and upper bound method for square plate.……..72

3.31 Interaction of rotational moment and torque by FE for square plate……73

3.32 Interaction of normal load and torque by FE for square plate……..73

3.33 Interaction of parallel load and rotational moment by FE for square plate…..74

3.34 Comparison of interactions of parallel and torsional loads by FE and upper bound method for rectangular, 2:1, plate.……76

FIGURE Page

3.35 Results comparison of upper bound and Eq. 3.19 for torsion and parallel load for square plate..……78

3.36 Results comparison of modified FE and Eq. 3.19 for torsion and rotational moment for square plate.……...78

3.37 Results comparison of modified FE and Eq. 3.19 for torsion and normal load for square plate.……79

3.38 Results comparison of upper bound and Eq. 3.19 for torsion and parallel load for rectangular plate with aspect ration of 2:1…….……..79

3.39 Anchor trajectory and orientation for a square plate loaded at eccentricity of 0.25 ft.……84

3.40 Trajectory predictions for 1.0 ft^2 square plate anchor, embedded 10 feet BML, at varying eccentricities during pull-out..……...85

3.41 Resistance predictions for 1.0 ft^2 square plate anchor, embedded 10 feet BML, at varying eccentricities during pull-out.…….……...87

4.1 Schematic of SEPLA installation...……...88

4.2 Schematic of anchor chain force...…….91

4.3 Configuration of SEPLA…...……95

4.4 Critical condition for the flap rotating backward relative to the fluke...……...97

4.5 Schematic of force equilibrium of the SEPLA...……...……98

4.6-A Trajectories of SEPLA without flap, not including anchor chain interaction…….…...104

4.6-B Capacities of SEPLA without flap, not including anchor chain interaction.……...104

4.7-A Trajectories of SEPLA without flap, including anchor chain interaction..…105

4.7-B Capacities of SEPLA without flap, including anchor chain interaction.……105

FIGURE Page

4.8-A Trajectories of SEPLA with flap, not including anchor chain interaction.…109

4.8-B Capacities of SEPLA with flap, not including anchor chain interaction.…...110

4.9 Final orientation of SEPLA...…….111

4.10-A Comparisons of trajectories of SEPLA with flap and without flap under different angles of pullout……...114

4.10-B Comparisons of capacities of SEPLA with flap and without flap under different angles of pullout……...115

LIST OF TABLES

TABLE Page

3.1 Bearing Capacity Factors..……..……..…31

3.2 Exponents in Eq. 3.2.…….……..35

3.3 Exponents in Eq. 3.5.……...50

3.4 Exponents in Eq. 3.12.…….59

3.5 Summary of Anchor Capacity Factors by Experiment and Interaction Model...61

3.6 Summary of Exponents in Various Interaction Models.…….77

4.1 Values of Exponents in Eq. 4.4.…….....90

4.2 Summary of Results Predicted by Model.…….112

CHAPTER I

INTRODUCTION

1.1 General

The development of offshore hydrocarbon fields has experienced a rapid growth in the past 30 years. The drilling operations have ventured into deep and ultra-deep water with depths approaching 2000 m and more (Aubeny et al., 2001; Randolph et al., 2005). As a result, the offshore production facilities have evolved from jacket or gravity platforms used in shallower water to floating structures that are tethered to the seabed, as shown in Fig. 1.1. These floating structures include tension leg platforms (TLP), spar platforms (SP), floating production systems (FPS) and floating production storage and offloading vessels (FPSO). The reliance on floating structures has focused greater attention on the anchoring system that withstands significant lateral and uplift loads imposed on floating structures. Plate anchors are a common anchoring system which is cost-effective and geotechnically efficient compared to other types of anchors such as anchor piles, suction caissons, gravity anchors and dynamically penetrating anchors (Torpedo). Unfortunately, plate anchors have not so far been preferred for permanent mooring because of the large uncertainties in predicting the anchor performance.

1.1.1 Concepts of Mooring Systems and Plate Anchors

The loads from floating structures acts on plate anchors through the mooring line (or anchor line) and hence the performance of plate anchors is affected by the profile

---

This dissertation follows the style and format of the *Journal of Geotechnical and Geoenvironmental Engineering.*

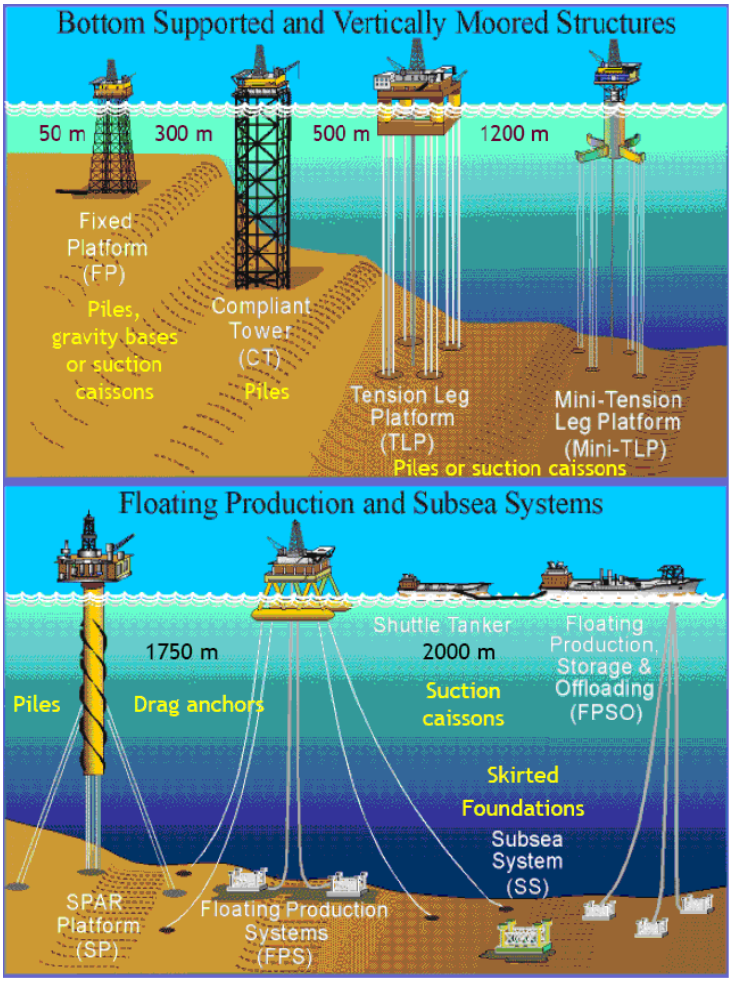

Courtesy: Minerals Management Services

Fig. 1.1 Development of deepwater systems

of the mooring line. Depending on the mooring line profile, the mooring systems can be divided into two categories: catenary mooring and taut or semi-taut leg mooring. The catenary mooring is most commonly used for mooring systems in shallow to deep water. The mooring line forms a standard catenary shape between the floating structure and the seabed and is horizontal along the seabed, as shown in Fig. 1.2. There is generally a significant length of the mooring line resting on the seabed with a trend toward

decreasing the length of the mooring line and maintaining the line angle above zero at all points (D'Souza et al., 1993). The mooring line cuts into the soil in the approximate shape of a reverse catenary, making a small angle with the horizontal at the padeye of the anchor such that the anchor is mainly loaded in a horizontal direction. The catenary mooring line generally consists of chain and steel cable that are relatively heavy. The weight of the mooring line can be a concern that limits the design of the floating structures in deep to ultra-deep water (Ruinen, 2000). The large extent of the anchor footprint on the seabed can also cause complications. Accordingly, the taut leg mooring (Fig. 1.2) is an alternative that primarily uses light weight mooring line such as polyester rope. In the taut leg mooring, the mooring line intersects the seabed at a significant angle such that the anchor will be subjected to an inclined load with a significant vertical component. In addition, an advantage of the taut leg mooring over the catenary mooring is that the footprint of the taut leg mooring is smaller than that of the catenary mooring for a similar application. It is therefore less likely to interfere with neighboring moorings or other subsea facilities (Ruinen and Degenkamp, 1999).

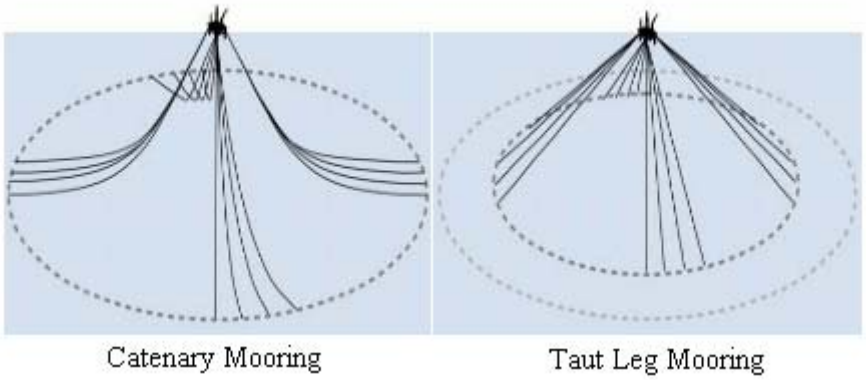

Fig. 1.2 Two main types of mooring systems (Ruinen, 2000)

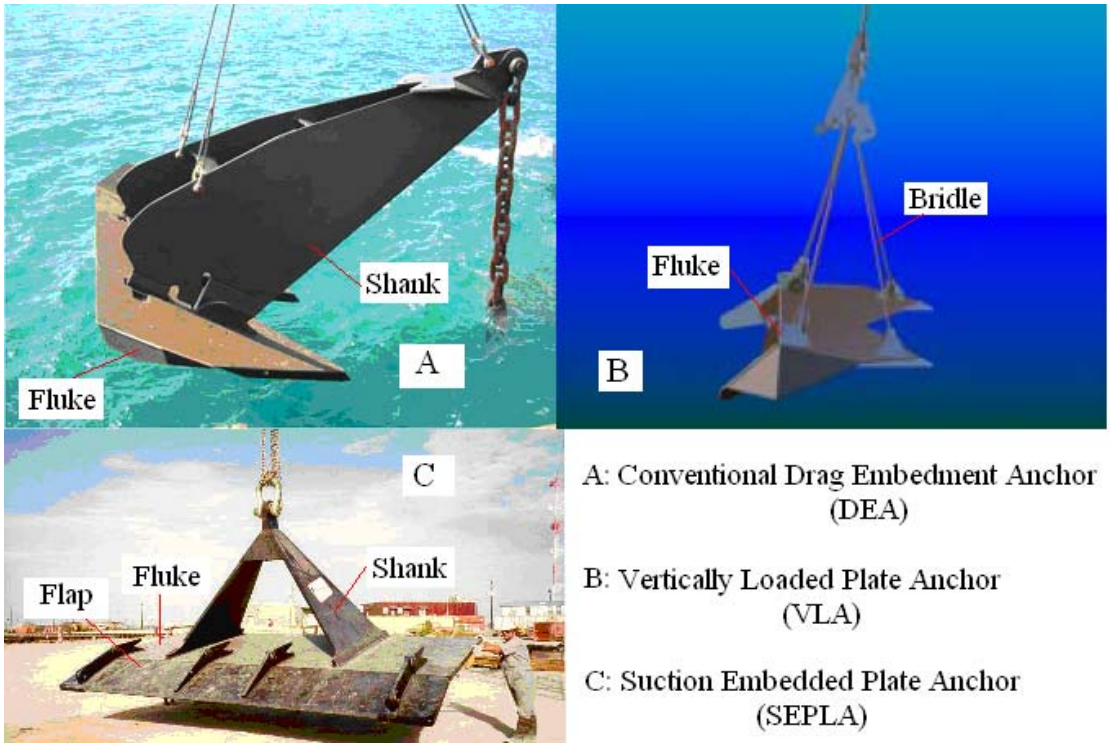

Fig. 1.3 Typical types of plate anchors

Compared with that of conventional ship anchors, the art of plate anchors has evolved to a very sophisticated level. There have been three main types of plate anchors employed to moor offshore floating structures: conventional drag embedment anchor (DEA), vertically loaded plate anchor (VLA) and suction embedded plate anchor (SEPLA). Examples of these anchor types are shown in Fig. 1.3. An important feature of the DEAs is that the shank is fixed to the fluke at an angle of approximately 50° for soft clay and 30° for sand or medium to hard clay (Randolph et al., 2005). The DEAs are not designed to resist significant vertical load components and hence are used for catenary moorings that impose an approximately horizontal load. For the taut leg moorings, however, anchors are needed to withstand an inclined load with a significant vertical

component. To satisfy this requirement, a new concept of drag embedment plate anchor was developed in which a flexible bridle (or thinner shank) can be manipulated after installation such that the anchor line force is to be normal to the fluke. This is the so-called vertically loaded plate anchor (VLA) which is designed to mobilize the maximum bearing capacity of the fluke. The most widely used VLAs are Vryhof Stevemanta and Bruce Dennla. Although the VLAs are still installed by means of drag embedment like the DEAs, they penetrate relatively deeper. Because of uncertainties in trajectory for DEAs and VLAs due to drag embedment, the suction embedded plate anchor (SEPLA) was conceived. The SEPLA uses a suction caisson to penetrate a plate anchor to the design depth and then retracts the suction caisson out of soil, leaving the anchor in place (Dove et al, 1998). The advantage of the SEPLAs is that the anchors can be penetrated to the target location and embedment depth.

1.1.2 Installation of Plate Anchors

Drag embedment is a widely used installation method for plate anchors (DEAs and VLAs), as shown schematically in Fig. 1.4. It includes the following procedures: first the anchor is lowered to the seabed in the correct orientation; then the anchor is

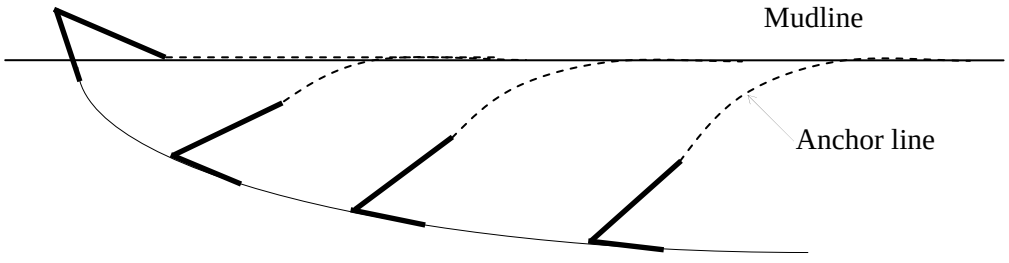

Fig. 1.4 Schematic of drag embedment installation

pulled horizontally by tensioning the anchor line at the mudline. The anchor then penetrates into soil initially along a trajectory roughly parallel to the fluke. As the anchor line makes a steeper angle with the horizontal the anchor rotates until it is translating approximately horizontally. For the VLAs, the bridle (or shank) can be adjusted such that the anchor line load is normal to the fluke. However, uncertainties in determining the exact depth of embedment and location of the anchor are why DEAs and VLAs have not been preferred for permanent moorings.

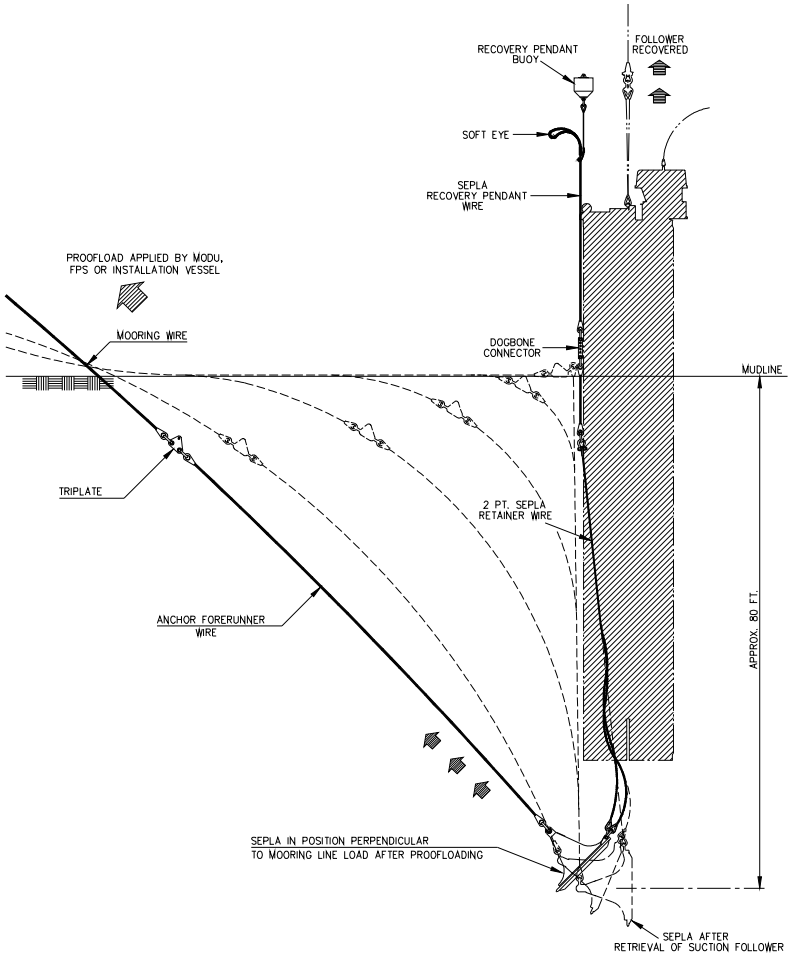

Fig. 1.5 Schematic of SEPLA installation (Dove et al., 1998)

To overcome the limitations of drag embedment, the SEPLA exploits the benefits of both suction caissons and VLAs. The anchor can be penetrated to the design depth at a specific location and "keyed" to develop the full capacity of the plate. In the configuration of the SEPLA, a flap is attached to the plate under the assumption that the flap helps the anchor "keying", as shown in Fig. 1.3. The SEPLA installation consists of three steps: caisson penetration, caisson retraction and anchor "keying", shown schematically in Figure 1.5. First the caisson with a SEPLA slotted vertically in its base is lowered to the seabed and penetrates into soil under its dead weight until the skin friction and end-bearing resistance equal the dead weight. Then the vent valve on the top of the caisson is closed and the water trapped inside is pumped out. The ensuing differential pressure drives the caisson to further penetrate to the design depth. The SEPLA is then released and the water is pumped back into the caisson, pushing the caisson out of the soil, leaving the anchor in place. The caisson is retracted from the seabed and prepared to be used for next installation. After the retraction of the caisson, the SEPLA is oriented vertically in the soil. The anchor line is tensioned and as the anchor line cuts into soil along the design direction the anchor starts to rotate or "key". It finally reaches the target orientation perpendicular to the direction of anchor line loading such that the maximum capacity of the anchor can be mobilized.

1.1.3 Issues

1.1.3.1 Out-of-Plane Loading on Plate Anchors

Mooring system failures caused seventeen deepwater mobile offshore drilling units (MODU's) to go adrift during hurricanes Ivan, Katrina and Rita in 2005. Drifting

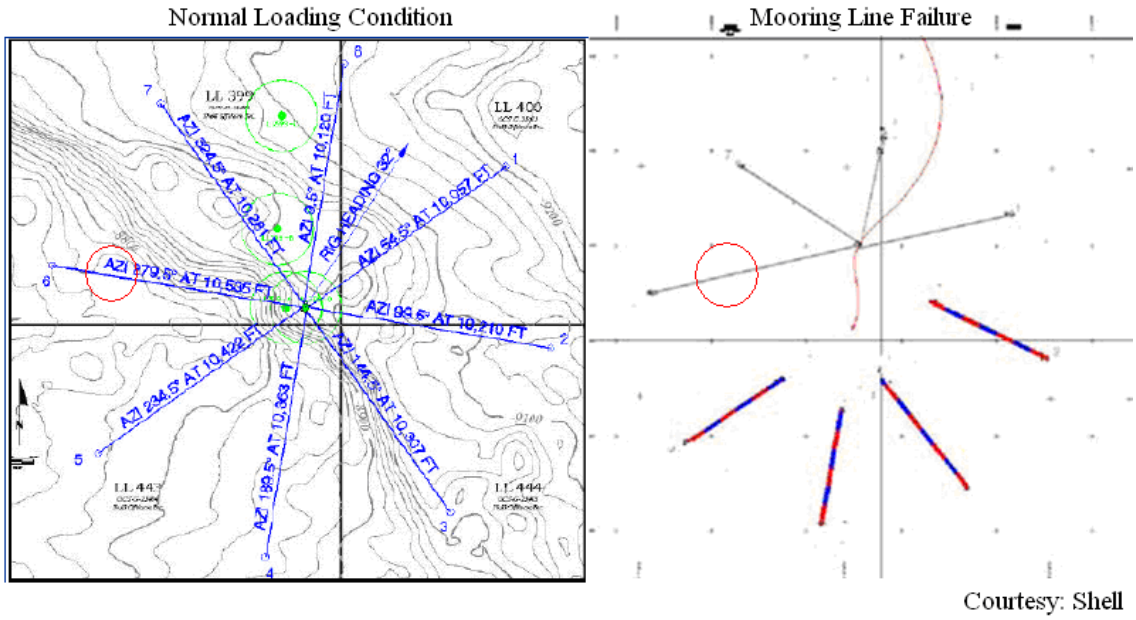

Fig. 1.6 Partial failure of mooring system

MODU's can potentially damage other critical elements of the offshore oil and gas infrastructure, e.g., colliding with floating or fixed production systems and transportation hubs, or damaging pipelines by dragging anchors. A critical problem is the performance of mooring anchors under conditions of partial failure of the mooring system, as shown in Fig. 1.6. Plate anchors for mooring systems for MODU's are typically designed to be loaded in the plane of the major axis of the anchor. This design assumption is reasonable for the normal loading (in-plane) conditions. However, if one or more of the mooring lines fail, the remaining anchors will be subjected to out-of-plane anchor line loads. The mooring line circled in Fig. 1.6 shows how the load varies from the in-plane condition to the out-of-plane condition. The out-of-plane loads can significantly reduce the capacity of the plate anchor at a given location in the soil. There are no established methods for

estimating the capacity, penetration and drag performance of plate anchors under various conditions of out-of-plane loading. Therefore, developments are needed to fill this gap in the current state of understanding of anchor performance.

1.1.3.2 Suction Embedded Plate Anchors

The installation of the SEPLA is more controlled that the DEA, but there are two problems that arise. The first one is that the soil in the vicinity of the SEPLA is disturbed because of caisson penetration and anchor "keying" and hence the soil strength is reduced. The second one is that the "keying" process gives rise to the loss of embedment depth, which leaves the plate in weaker soil in typical soil condition. The reduced soil strength can be recovered in time by soil reconsolidation, but the loss of embedment depth is irretrievable. Consequently, it is important to be able to accurately estimate the loss of embedment depth during the "keying" process.

1.2 Objectives of Research

To solve the problems presented above, the research proposed herein has two major objectives. The first is to develop a computational model that can be used to estimate the undrained performance of plate anchors subjected to general three dimensional (out-of-plane) loading and develop an understanding of anchor performance under these conditions. The computational model will address both anchor capacity and trajectory prediction. The second major objective is to develop an analytical model for predicting the trajectory during the "keying" process and the ultimate capacity of the SEPLA after the "keying" is complete. The study explores the effect of the flap on the performance of the SEPLA and provides a theoretical basis for the design of the SEPLA

plate configuration including the flap.

1.3 Outline of Research

This research consists of two parts: out-of-plane loading of plate anchors and the behavior of suction embedded plate anchors (SEPLAs).

For out-of-plane loading on plate anchors, the work is focused on the plate anchors of square and rectangular (aspect ratio 1:2) shapes. The study is carried out in the following steps. Two dimensional finite element analyses are performed and compared to previous work to verify the accuracy of the FE models used in this study. Three dimensional FE analyses are then conducted to investigate the interaction effects between normal and moment loading, including the limiting conditions of pure normal load and pure moment. The ultimate values of anchor capacity under pure loading are compared with known solutions or upper bound solutions in order to validate the results. In addition, upper bound analyses are conducted for the interaction of parallel load and torque. Finally, a computational model is obtained by fitting an empirical equation to the FEM and upper bound results. This model can be used to estimate the capacities of plate anchors under general loading conditions. Using this model, a method is developed for predicting anchor trajectories using the associated flow rule of plasticity theory. Parallel experiments have been conducted on the out-of-plane loading of plate anchors at the University of Texas at Austin. The experimental results are used to verify the proposed computational model.

For the behavior of the SEPLAs, the study will take account of two cases: the SEPLA without a flap and the SEPLA with a flap. Based on the yield function for strip

plate, a plastic limit model is developed to calculate the trajectory and corresponding capacities of the SEPLA, and to estimate the loss of embedment depth and anchor orientation during the “keying” process and the capacity subsequent to “keying”. The model incorporates the anchor-chain interaction, and the results are verified by some known solutions. The effect of the flap on the behavior of the SEPLAs is studied by comparing the behavior of the SEPLA without a flap with the SEPLA with a flap.

CHAPTER II

THEORETICAL BACKGROUND

2.1 Concepts of Soil Plasticity

The theory of plasticity has played an important role in soil mechanics since Coulomb established the limit equilibrium method based on the Coulomb's failure criterion in the 1770's. Plastic behavior is described by three components: the yield criterion, the flow rule and the hardening (softening) law. The yield criterion is a central concept in plasticity, referred to as a stress level at which the elastic limit is attained. The elastic limit is defined by a specific condition on the stress state:

$$f(\sigma_{ij}) = 0 \tag{2.1}$$

where σ_{ij} represents stress components; f is the so-called yield function (or yield surface). The state of $f(\sigma_{ij}) < 0$ corresponds to elastic behavior, and $f(\sigma_{ij}) = 0$ defines yield and loading beyond this point leads to accumulation of plastic deformation.

A commonly used yield criterion for undrained analysis in soil mechanics is the Tresca criterion, which is written as

$$\frac{\sigma_1 - \sigma_3}{2} = s_u \tag{2.2}$$

where σ_1 and σ_3 are the major and minor principal stresses, respectively; s_u is the undrained strength of soil. The Tresca criterion is a simple expression to deal with two dimensional problems but becomes very complicated when written in general three-dimensional form. An alternative criterion is the von Mises yield condition that

considers the effects of shear in all directions (Murff, 2006). This yield criterion is expressed in the form of

$$J_2^{1/2} - k = 0 \tag{2.3}$$

where J_2 is the second invariant of stress deviator; k is a constant related to shear strength. J_2 is written in terms of principal stresses as

$$J_2 = \frac{1}{6}\left[\left(\sigma_1 - \sigma_2\right)^2 + \left(\sigma_2 - \sigma_3\right)^2 + \left(\sigma_3 - \sigma_1\right)^2\right] \tag{2.4}$$

If expressed for plane strain condition, both Tresca criterion and von Mises criterion have the same form.

The yield criterion characterizes the transition of material from an elastic state to a flow (or plastic) state. In soils, it is notable that plastic deformations occur well before a failure condition is achieved but it is common to assume that the material is

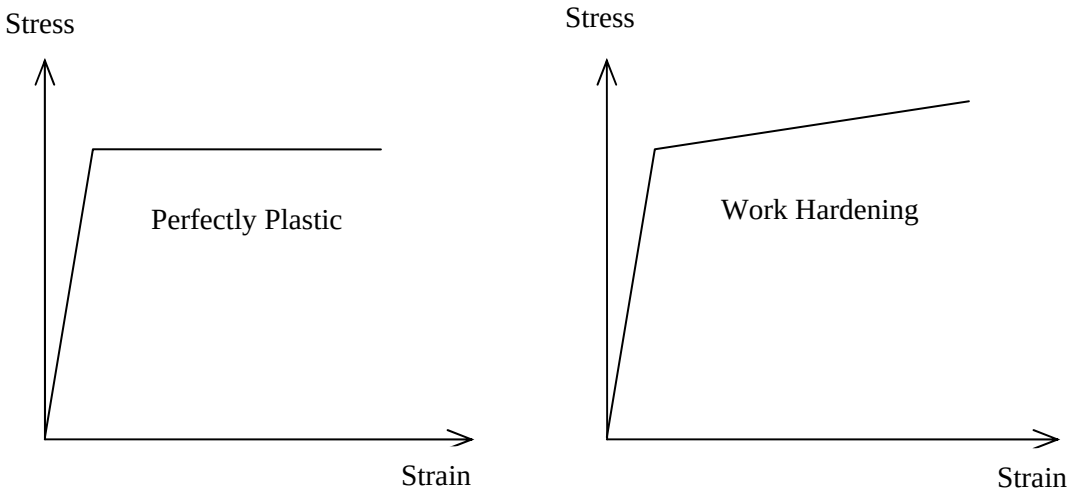

Fig. 2.1 Behavior of plasticity for stable materials

elastic below yield (Murff, 2006). For materials obeying Drucker's stability postulate (non-softening), there exist two kinds of plastic behaviors: perfectly plastic and work hardening. In perfect plastic materials the strain increases indefinitely under a constant state of yield stresses whereas in materials with hardening the yield stresses continue to increase as the plastic strain proceeds, as shown in Fig. 2.1. The commonly used models of hardening include isotropic, kinematic and mixed hardening. In an isotropic hardening model the initial yield surface expands symmetrically in stress space whereas in a kinematic hardening model the yield surface translates around in stress space (Murff, 2006). The mixed hardening arises from a combination of isotropic and kinematic models that becomes more general for describing the plastic behavior of materials.

For perfectly plastic materials, the yield surface is fixed for a given stress state. If the yield surface is continuous, the increment of plastic strain $\dot{\varepsilon}_{ij}$ follows the direction of the outward normal to the yield surface $f(\sigma_{ij}) = 0$, which is written in the form of

$$\dot{\varepsilon}_{ij} = \lambda \frac{\partial f}{\partial \sigma_{ij}} \tag{2.5}$$

where λ is a positive scale factor that cannot be uniquely determined for perfectly plastic materials but can be specific for work hardening materials. The yield surface is therefore a plastic potential surface here, and Eq. 2.5 is called the associated flow rule. This is a consequence of Drucker's general stability postulate. Drucker's stability postulate also indicates that if the yield criterion is not continuous (has corners for example) the increment of plastic strain necessarily lies inside the hypercone formed by all external normals of the yield surface.

2.2 Plastic Limit Analysis

Unlike the conventional limit equilibrium method, plastic limit analysis incorporated stress-strain relations that form the basis for a theory of continuum mechanics of deformable solids (Chen and Liu, 1990). Chen and Liu (1990) summarized the three ideal properties that a body must have for the plastic limit theorems to be valid: (1) The material is perfectly plastic; (2) The yield surface is convex and the increment of plastic strain is defined by the associated flow rule, i.e. the material obeys Drucker's stability postulate; (3) The variations in geometry of the body that occur at the limit load are insignificant such that the principle of virtual work can be valid.

2.2.1 Lower Bound Method

Calladine (1969) stated the lower bound theorem as follows: "If any stress distribution throughout the structure can be found which is everywhere in equilibrium internally and balances certain external loads and at the same time does not violate the yield condition, these loads will be carried safely by the structure." The stress field described above is termed a statically admissible stress field (Chen, 1975). A stress field satisfying internal equilibrium can be expressed by the following equation

$$\frac{\partial \sigma_{ij}}{\partial x_j} + F_i = 0 \tag{2.6}$$

where F_i denotes body forces. At yield, the equilibrium equation can be combined with $f(\sigma_{ij}) = 0$ and solved to give a rigorous solution using the method of characteristics where some useful but highly idealized solutions are available. The solution by the method of characteristics is not a lower bound solution until the stress field is extended

from the yielding zone to the rigid regions surrounding this zone such that it is statically admissible. These solutions are limited to very idealized conditions, and the calculations are often quite complicated (Murff, 2006).

A commonly used approach for lower bound solution is to divide the stress field into some discontinuous fields that have a constant state of stress throughout each of them. These constant states of stresses satisfy internal equilibrium and stress boundary conditions, and do not violate the yield criterion. The interfaces of discontinuous stresses are allowed but must still satisfy the equilibrium equations at every point. Fig. 2.2 shows a simple example of this approach in which the bearing capacity solution of $p = 4s_u$ is easily obtained. The lower bound method is a powerful tool for providing conservative solutions which are what engineers generally prefer. However, there exists much difficulty in applying the method to complex conditions such as irregular boundary conditions and nonhomogeneous and anisotropic strength.

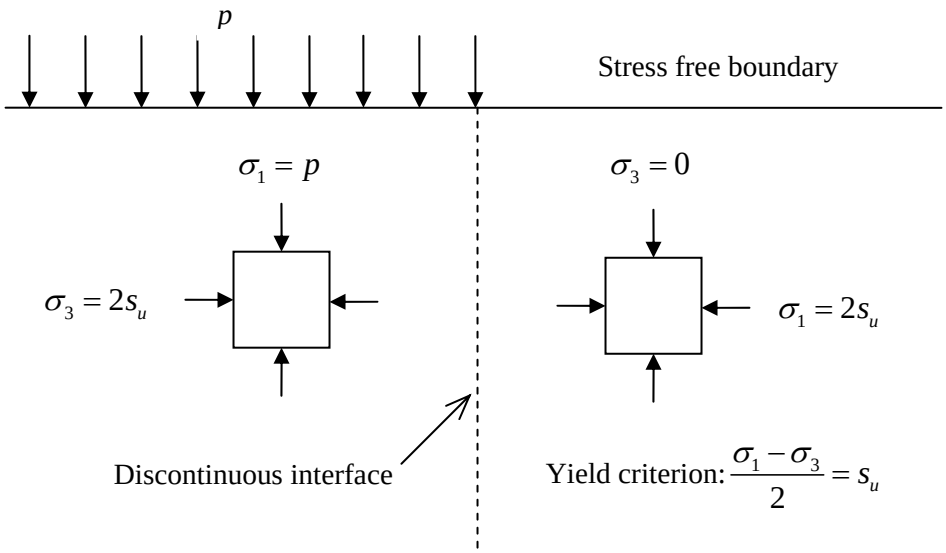

Fig. 2.2 Example of lower bound method (Murff, 2006)

2.2.2 Upper Bound Method

The upper bound theorem was stated by Calladine (1969) as follows: “If an estimate of the plastic collapse load of a body is made by equating internal rate of dissipation of energy to the rate at which external forces do work in any postulated mechanism of deformation of the body, the estimate will be either high or correct.” A major requirement of the upper bound method is to ensure a kinematically admissible mechanism for the failure of materials is selected. The principle of virtual work leads to a governing equation by equating the internal dissipation rate to the external work rate for the mechanism in question. If any geometric parameters are involved in the mechanism, a minimum upper bound solution can be obtained by optimizing the solution with respect to these parameters.

The rate of internal dissipation for materials obeying the associated flow rule can be calculated as follows

$$\dot{D} = \sigma_{ij}\dot{\varepsilon}_{ij} = \lambda\sigma_{ij}\frac{\partial f}{\partial \sigma_{ij}} \tag{2.7}$$

where $\dot{D}$ is the energy dissipation rate for the mechanism and f is the yield function. Thus, $\dot{D}$ has different forms corresponding to different yield criteria. For undrained analysis, the von Mises criterion and the Tresca criterion are considered herein.

For the von Mises criterion, substituting Eq. 2.3 into Eq. 2.7 gives rise to

$$\dot{D} = \frac{\lambda}{2k}\sigma_{ij}\frac{\partial J_2}{\partial \sigma_{ij}} = \lambda k \tag{2.8}$$

The increments of strain can be written in the following form by substituting Eq. 2.3 into Eq. 2.5

$$\begin{pmatrix} \dot{\varepsilon}_x \\ \dot{\varepsilon}_y \\ \dot{\varepsilon}_z \\ \dot{\varepsilon}_{xy} \\ \dot{\varepsilon}_{yz} \\ \dot{\varepsilon}_{zx} \end{pmatrix} = \frac{\lambda}{2k} \begin{pmatrix} \frac{1}{3} & 0 & -\frac{1}{3} & 0 & 0 & 0 \\ -\frac{1}{3} & \frac{1}{3} & 0 & 0 & 0 & 0 \\ 0 & -\frac{1}{3} & \frac{1}{3} & 0 & 0 & 0 \\ 0 & 0 & 0 & 1 & 0 & 0 \\ 0 & 0 & 0 & 0 & 1 & 0 \\ 0 & 0 & 0 & 0 & 0 & 1 \end{pmatrix} \begin{pmatrix} \sigma_x - \sigma_y \\ \sigma_y - \sigma_z \\ \sigma_z - \sigma_x \\ \tau_{xy} \\ \tau_{yz} \\ \tau_{zx} \end{pmatrix} \tag{2.9}$$

The equations including $\dot{\varepsilon}_x$, $\dot{\varepsilon}_y$ and $\dot{\varepsilon}_z$ are not linearly independent because the sum of $\dot{\varepsilon}_x$, $\dot{\varepsilon}_y$ and $\dot{\varepsilon}_z$ is zero for incompressible materials (undrained behavior of soil). The equation $(\sigma_x - \sigma_y) + (\sigma_y - \sigma_z) + (\sigma_z - \sigma_x) = 0$ is used to replace one of them. Inverting the updated Eq. 2.9 gives

$$\begin{pmatrix} \sigma_x - \sigma_y \\ \sigma_y - \sigma_z \\ \sigma_z - \sigma_x \\ \tau_{xy} \\ \tau_{yz} \\ \tau_{zx} \end{pmatrix} = \frac{2k}{\lambda} \begin{pmatrix} \dot{\varepsilon}_x - \dot{\varepsilon}_y \\ \dot{\varepsilon}_y - \dot{\varepsilon}_z \\ \dot{\varepsilon}_z - \dot{\varepsilon}_x \\ \dot{\varepsilon}_{xy} \\ \dot{\varepsilon}_{yz} \\ \dot{\varepsilon}_{zx} \end{pmatrix} \tag{2.10}$$

Substituting Eq. 2.10 back into Eq. 2.3 and then solving for λ leads to

$$\lambda = \sqrt{2\dot{\varepsilon}_{ij}\dot{\varepsilon}_{ij}} \tag{2.11}$$

Therefore, from Eq. 2.8 the rate of internal energy dissipation is

$$\dot{D} = \lambda k = k\sqrt{2\dot{\varepsilon}_{ij}\dot{\varepsilon}_{ij}} \tag{2.12}$$

Eq. 2.12 is used to calculate the dissipation rate for a continuously deforming region in three dimensions. For the dissipation along a slip surface, the deformation mode considered here is shown in Fig. 2.3. A sheared zone whose thickness is *t* is assumed to exist between two rigid blocks. The bottom block is stationary whereas the top block has

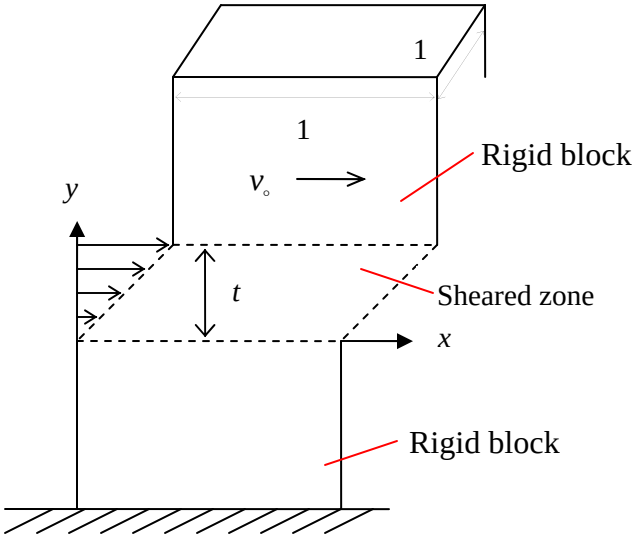

Fig. 2.3 Dissipation along slip surface (Murff, 2006)

a virtual velocity $v_\circ$. The velocity field in the sheared zone is

$$\dot{u}_i = \frac{v_\circ}{t} y\,,\ \dot{v} = 0 \text{ and } \dot{\omega} = 0 \tag{2.13}$$

Therefore, the non-zero strain rate is

$$\dot{\varepsilon}_{xy} = \dot{\varepsilon}_{yx} = \frac{v_\circ}{2t} \tag{2.14}$$

Substituting Eq. 2.14 into Eq. 2.12 gives the dissipation per unit volume

$$\dot{D} = \frac{kv_\circ}{t} \tag{2.15}$$

Integrating Eq. 2.15 over the sheared zone gives the total dissipation rate

$$\dot{D}_t = \int_{x=0}^{1}\int_{y=0}^{t} \frac{kv_\circ}{t}\,dydx = kv_\circ \tag{2.16}$$

Eq. 2.16 shows that the total dissipation rate is independent of the thickness of the

sheared zone. Therefore, when the thickness *t* approaches zero, i.e. the sheared zone becomes a slip surface, the rate of internal dissipation is

$$\dot{D} = kv_{\circ} \tag{2.17}$$

For the Tresca criterion, principal stresses and strains are employed for calculation due to the complexity of the yield function in three dimensions. Two conditions need to be considered in principle stress space. The first condition is that the strain increment is normal to the yield surface (not including corners). In this case, the intermediate principal strain increment $\dot{\varepsilon}_2 = 0$, so we have $\dot{\varepsilon}_1 = -\dot{\varepsilon}_3$ due to the incompressibility of undrained soils. Substituting into Eq. 2.7 gives the rate of internal dissipation as

$$\dot{D} = 2s_u \left|\dot{\varepsilon}_1\right| \tag{2.18}$$

where $\dot{\varepsilon}_1$ is the largest absolute principal strain increment. The second condition is that the strain increment occurs at the corner. In this case, $\sigma_2 = \sigma_3$ and $\dot{\varepsilon}_1 = -(\dot{\varepsilon}_2 + \dot{\varepsilon}_3)$. Substituting into Eq. 2.7 leads to the same result as Eq. 2.18. For the dissipation along the slip surface, the calculation is similar to von Mises criterion. Transforming the strain rate in Eq. 2.14 to the state of principal strain and substituting into Eq. 2.18, we have the rate of internal dissipation

$$\dot{D} = s_u v_{\circ} \tag{2.19}$$

which has the same form as Eq. 2.17. Writing Eqs. 2.12 and 2.18 for plane strain conditions gives identical forms, that is

$$\dot{D} = 2s_u \sqrt{\dot{\varepsilon}_x{}^2 + \dot{\varepsilon}_{xy}{}^2} \tag{2.20}$$

Although the form of the equation is the same for both criteria, the value of s_u may differ based on the same tests. For example, for an unconfined compression test, $s_u = \frac{\sigma_1}{\sqrt{3}}$ for von Mises and $s_u = \frac{\sigma_1}{2}$ for Tresca.

2.2.3 Application of Plastic Limit Analysis to Plate Anchors

Compared to the conventional limit equilibrium method, plastic limit analysis exhibits great flexibility in predicting the ultimate capacities of plate anchors. However, it may also be difficult to get an ideal solution for some complex conditions. Some relevant solutions can be found in the works of Rowe (1978), Bransby and O'Neill (1999), O'Neill et al. (2003), Merifield et al. (2001) and Martin and Randolph (2001). Here we summarize cases for deeply embedded, rigid plate anchors where the soil is

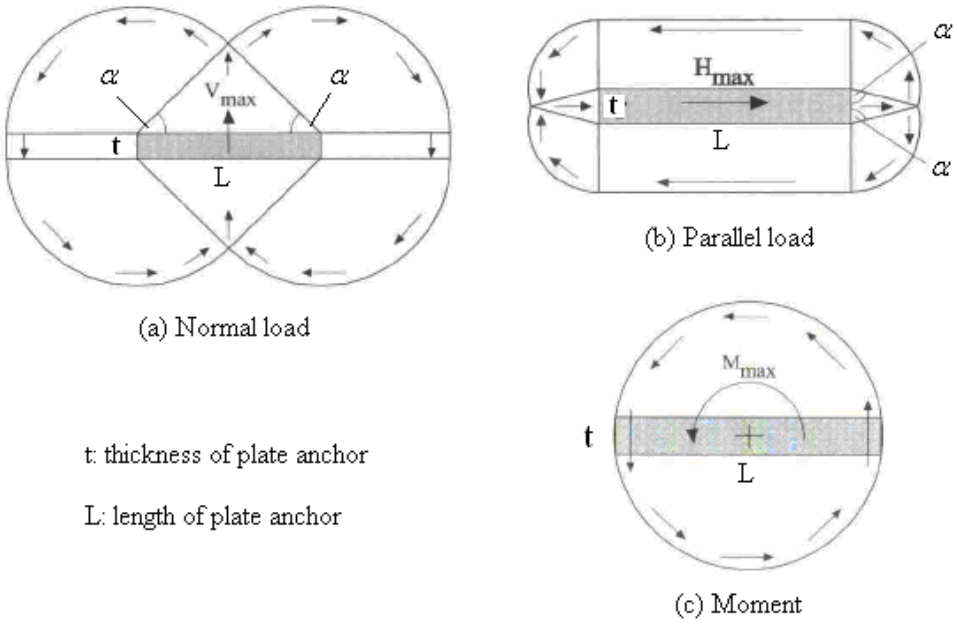

Fig. 2.4 Upper bound mechanism for strip plate anchor (O'Neill et al. 2003)

uniform and fully bonded to the plate anchor, i.e. no separation of the soil from the back of the anchor occurs. Kinematically admissible velocity fields were proposed by O'Neill et al. (2003) for a thin strip plate anchor subjected to pure normal, parallel and moment loadings, as shown in Fig. 2.4. The upper bound solutions are presented as non-dimensional capacity factors as follows:

$$N_p = \frac{F_{n\max}}{Ls_u} = 4\left(\pi - \alpha + \frac{\tan\alpha}{2}\right) + 4\frac{t}{L}\left(\frac{1}{2} + \cos\alpha\right) \tag{2.21}$$

$$N_s = \frac{F_{s\max}}{Ls_u} = 2\left(1 + N_{tip}\frac{t}{L}\right) \approx 2 + 15\frac{t}{L} \tag{2.22}$$

$$N_m = \frac{M_{\max}}{L^2 s_u} = \frac{\pi}{2}\left(1 + \left(\frac{t}{L}\right)^2\right) \tag{2.23}$$

where α is the angle subtended by the failure wedge that is varied to give the minimum upper bound solutions. A lower bound solution for a vanishingly thin, strip plate anchor under pure normal loading was given by Rowe (1978) as $N_p = 10.28$. Martin and Randolph (2001) employed the method of characteristics to generate stress fields for a vanishingly thin, circular plate anchor and then extended them to infinity, as shown in Fig. 2.5. The ensuing statically admissible stress fields lead to rigorous lower bound solutions of $N_p = 12.42$ for smooth surface and $N_p = 13.11$ for rough surface. The consistent velocity fields, shown in Fig. 2.5, were then established corresponding to stress fields for both smooth and rough surfaces, which give rise to the upper bound solutions that appear to be the same as the lower bounds. The agreement of lower and upper bounds indicates that the solutions are the exact theoretical solutions.

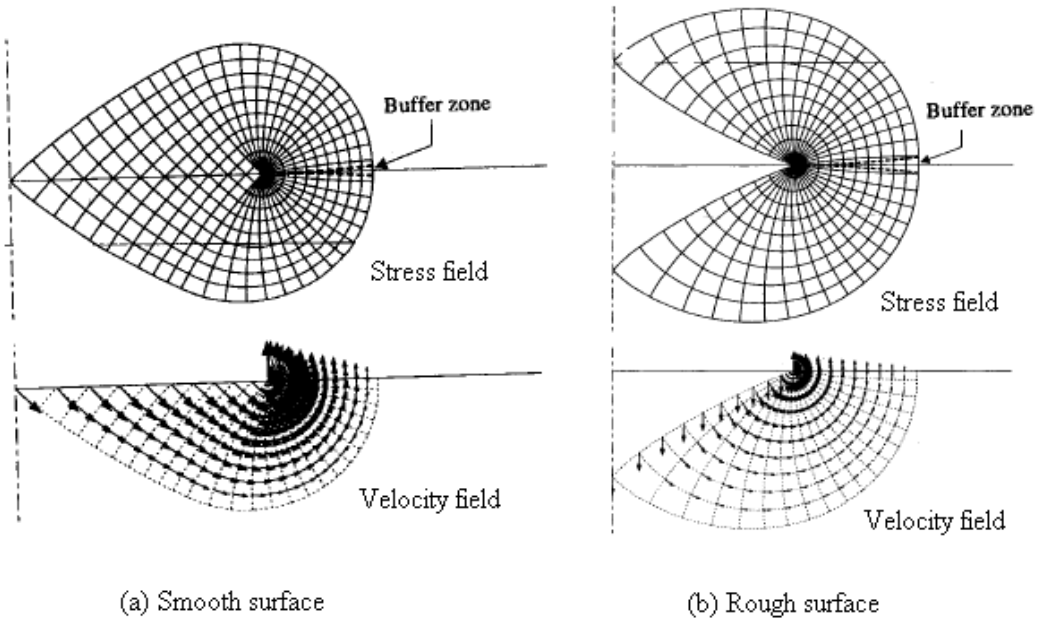

Fig. 2.5 Stress and velocity fields for circular plate anchor (Martin and Randolph, 2001)

2.3 Finite Element Analysis

The analytical plastic limit solutions are limited to the problems in which a specific velocity (stress) field can be reasonably postulated and are difficult to obtain for complex conditions. The finite element method is a powerful numerical way of dealing with complicated elasto-plastic behavior. The theory of finite elements can be found in many related textbooks, and thus it is not discussed herein. Rowe and Davis (1982) conducted an elasto-plastic finite element study on a vanishingly thin, strip plate anchor subjected to a pure normal loading using k_4 failure criterion (k_4 failure load corresponds to an apparent stiffness of one quarter of the elastic stiffness) and obtained a solution of $N_p = 11.95$, which is 4.6% higher than the upper bound solution of 11.42 that can be calculated by Eq. 2.21. O'Neil et al. performed analyses for a strip plate with the length

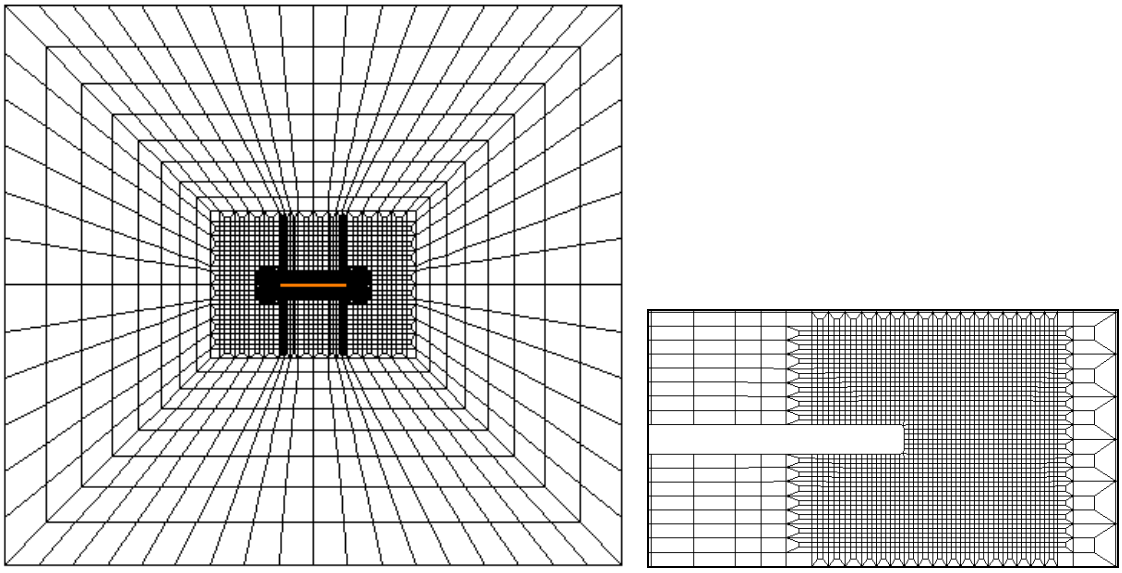

Fig. 2.6 Typical finite element mesh (detail on right)

to thickness ratio of $L/t = 7$ that is similar to that of a Vryhof Stevpris anchor fluke (Vryhof Anchors 2005). They considered a combined loading with normal, parallel and moment components and obtained the interactions between different loading components, in which the capacity factors under pure loading are $N_p = 11.87$, $N_s = 4.29$ and $N_m = 1.49$. Allowing for different roughnesses of the anchor surface, an industry sponsored study (API project, Anderson et al. 2003; Murff et al. 2005) was carried out to simulate a range of length to thickness ratios including $L/t = 5$, 6, 7, 8, 9, 10, 15, 20. Fig. 2.6 shows a typical finite element mesh where the problems due to singularities at the corners are minimized by using the mesh of high density. Interaction curves for the length to thickness ratio of $L/t = 7$ are shown in Fig. 2.7 where the capacity factors under pure loading are $N_p = 11.58$, $N_s = 4.49$ and $N_m = 1.74$. The finite element results were fitted to a yield model that can be used for predicting the strip anchor capacity

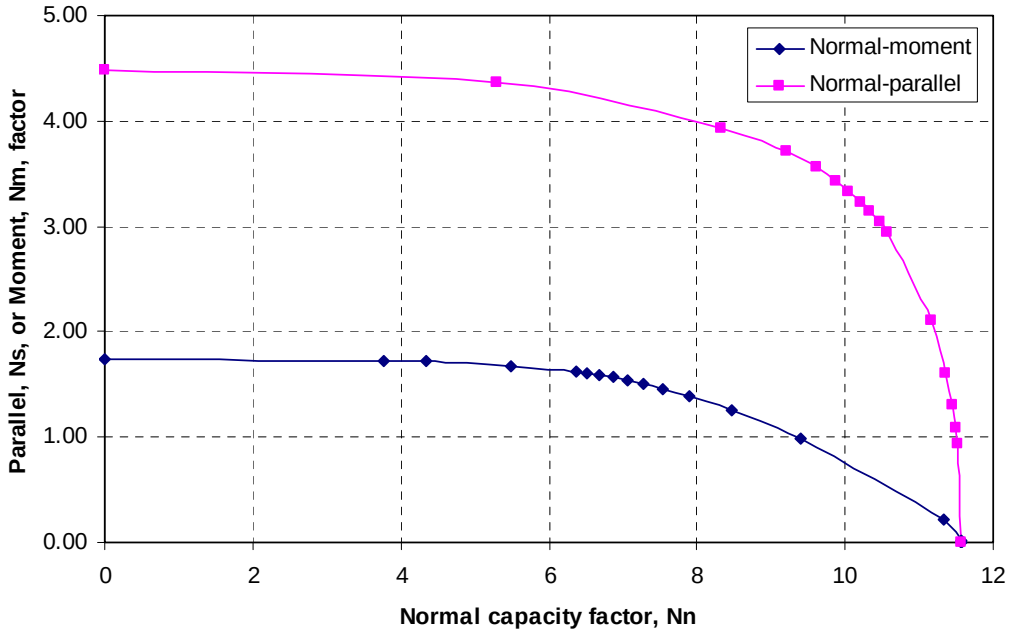

Fig. 2.7 Interaction curves in normal-parallel and normal-moment space (bonded)

under any combined loading condition.

Limited work has been performed for three-dimensional problems for plate anchors due to their complexity. Merifield et al. (2003) applied three-dimensional finite element limit analysis to estimate the effect of plate shape on the pullout capacity of anchors. Not allowing for the suction at the back of plate anchor (immediate breakaway), they obtained a solution of $N_p = 11.9$ for the normal capacity of a vanishingly thin, square plate anchor.

CHAPTER III

OUT-OF-PLANE LOADING ON PLATE ANCHORS

3.1 Idealized Plate Anchors

To simplify their analysis, plate anchors such as DEAs, VLAs and SEPLAs are generally idealized as standard rectangular or square plates. They are typically designed to be loaded within the vertical plane (in-plane loading) containing the major axis of the anchor and hence can be considered as a plane strain problem as an approximation. The shank (or bridle) makes the load eccentric from the plate centroid such that a rotational moment is generated. For plane strain conditions, the equivalent loading can be generalized as normal, parallel or shear, moment components acting at the centroid, as shown in Fig. 3.1 (a). The failure of one or more mooring lines can result in the loading being out of the plane. In this case the loading condition becomes a three-dimensional

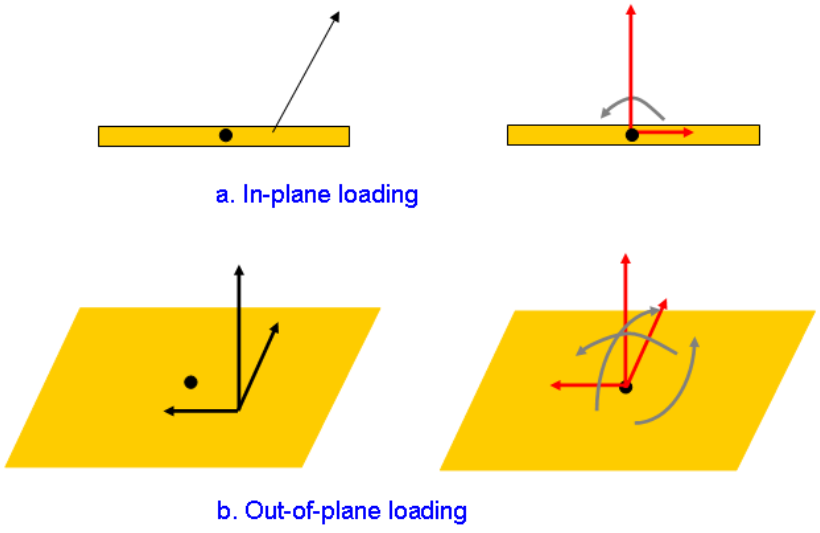

Fig. 3.1 Schematic of idealized plate anchors

problem. A general loading can be resolved into six components acting at the plate centroid, which include the normal load, two parallel or shear loads, two rotational moments and one torsional moment, as shown in Fig. 3.1 (b).

3.2 Two-Dimensional Analyses (In-plane Loading)

3.2.1 Two-Dimensional Finite Element Model

In the previous API/Deepstar study (Anderson et al, 2003), solutions were obtained for in-plane loading of a two dimensional plate i.e. a slice of unit width embedded in soil with uniform strength. These results were obtained for a plate with varying thickness using finite element analyses. To verify/calibrate the methods used in this study, we first repeated some of the 2-D analyses for similar plate anchor models.

The commercial program, ABAQUS (HKS, 2006), was used to carry out these calculations. The perfectly plastic model with von Mises yield criterion and associated flow rule was assumed for the soil. The Young's modulus was given by a ratio of the modulus to the undrained shear strength of soil, $E/S_u = 500$, and the Poisson's ratio was set at 0.49 to simulate undrained behavior. It is important to note that the elastic properties have no effect on anchor capacity but are required for FEM analysis (Chen, 1975). The plate anchor was considered to be a rigid body of thickness t, whose motion is controlled by a reference point (RP), i.e. the motion can be prescribed by applying boundary conditions at RP. The plate is assumed to be fully "bonded" to the soil around it. The 4-node bilinear plane strain quadrilateral, hybrid element was used to generate the FEM mesh, shown in Fig. 3.2. This mesh consists of about 26778 elements, 80811 degrees of freedom, and requires approximately 120 minutes of SGI Origin 3800

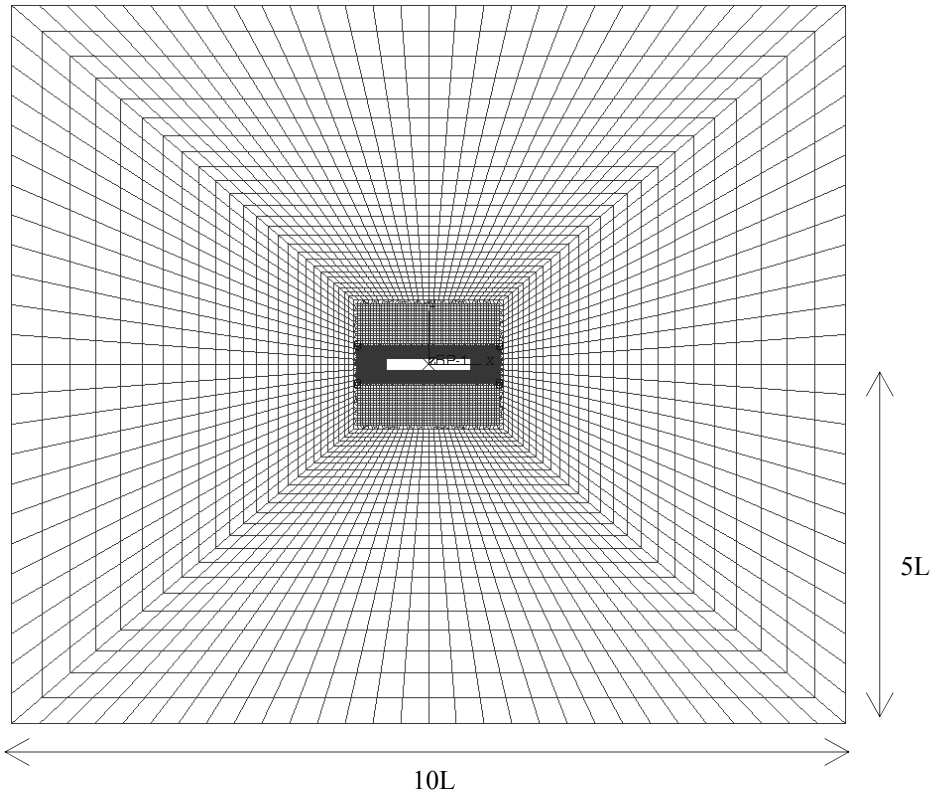

Fig. 3.2 Finite element mesh for plane strain analysis of a plate anchor (L/t = 7)

computer time for a complete non-linear solution that is to determine the ultimate load capacity of the plate. All analyses were performed under "displacement-control" conditions, in which a vertical, parallel or rotational displacement was applied to the plate anchor through the reference point to investigate its behavior. The soil forces on the anchor were then determined from the integration of the resulting nodal loads.

3.2.2 Two-Dimensional FE Results and Comparisons with Previous Studies

The various capacities of a thin plate anchor in undrained soil can be characterized by the following non-dimensional factors:

$$N_p = \frac{F_{n\max}}{Ls_u};\ N_s = \frac{F_{s\max}}{Ls_u};\ \ N_m = \frac{M_{\max}}{L^2 s_u} \tag{3.1}$$

where L is the length of the plate anchor (in the intended plane of loading); $F_{n\max}$, $F_{s\max}$ and $M_{\max}$ are the normal, parallel and rotational capacities per unit width (normal to the intended plane of loading), respectively. Thus, once we have determined the capacities for a specific plate length and soil strength for a pure loading condition (such as pure normal load) then we can determine the non-dimensional factors and hence immediately estimate the capacity for a plate of any length in a soil of any strength. This solution is strictly valid for an infinitely wide plate. A crude estimate of capacity for a finite width plate can be made by simply multiplying the solution for a unit width by the actual width. The effect of this limitation will be discussed in a later section. Here we are neglecting the effect of the ratio of plate thickness to length (t/L). This effect is small for normal and moment loading but can be more important for parallel or shear loading.

3.2.2.1 Bearing Capacities under Pure Loading

Fig. 3.3 and Fig. 3.4 show the finite element prediction for the responses of plate anchors subjected to pure translational or rotational loading. The response is approximately linear at the beginning of loading until reaching about 70% of the ultimate normal resistance and about 90% of the ultimate moment resistance. The non-linear behavior of the parallel resistance is more pronounced at lower levels of loading. After significant non-linear behavior of the curves shown in Fig. 3.3, the normal and parallel resistances both approach a plateau. The capacity (ultimate resistance) is taken to be the plateau value before the normal and parallel displacement reach 10% of the anchor length (the length is the anchor dimension in a vertical plane through the plate axis parallel to the intended loading direction). Fig. 3.4 shows that the moment

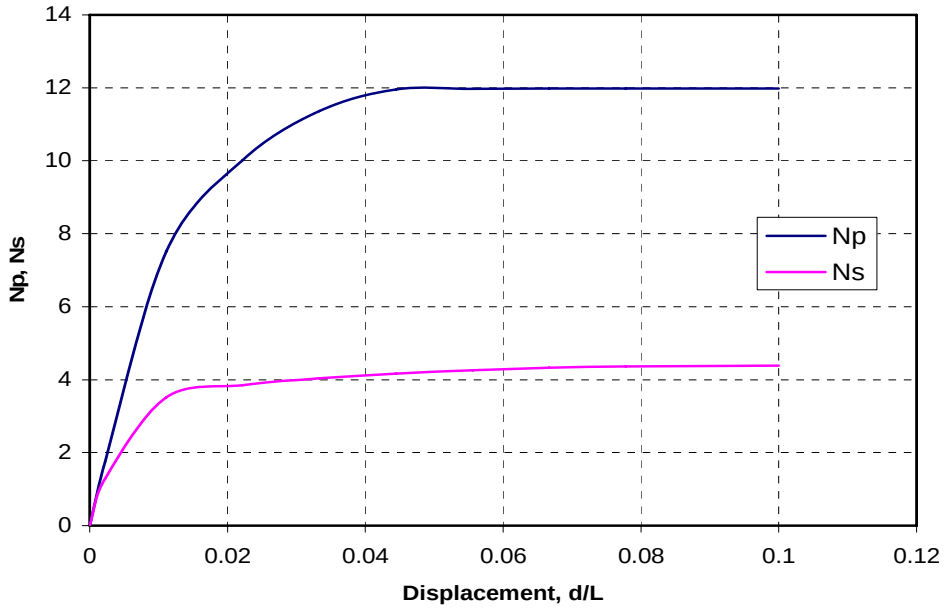

Fig. 3.3 Plate anchor response under normal and parallel load for plane strain conditions

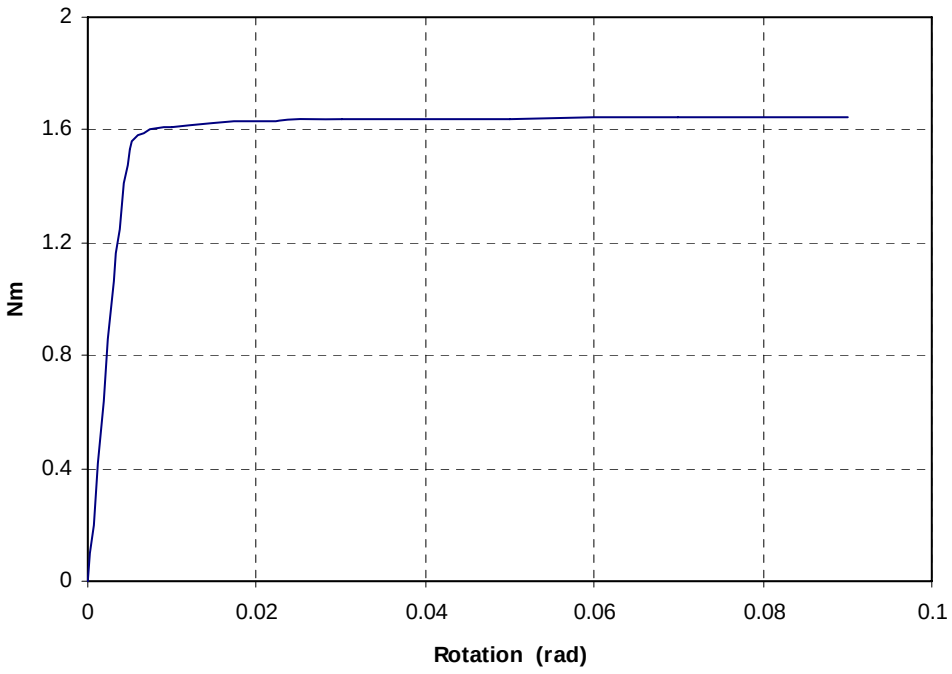

Fig. 3.4 Plate anchor response under pure moment for plane strain conditions

Table 3.1 Bearing Capacity Factors

Bearing Capacity Factor	Current	API/Deepstar
N_p	11.98	11.58
N_s	4.39	4.49
N_m	1.645	1.74

resistance is mobilized such that the ultimate value is reached at a rotation of less than 3°. The capacity factors shown in Fig. 3.3 and Fig. 3.4 are tabulated in Table 3.1 along with values obtained in the API/Deepstar Study (Andersen et al., 2003). Note again that the failure loads in any of these analyses are independent of the elastic properties assumed for the soil. Generally speaking, the two sets of solutions compare very well. N_p is 3% higher than the solution given in the API/Deepstar Study (Andersen et al., 2003), whereas N_s and N_m are 2% and 5% lower, respectively. These slight discrepancies might be caused by different mesh configurations and other minor details of the model.

3.2.2.2 Interaction Surfaces for Planar Loading of Plate Anchors

Finite element analyses were carried out to evaluate the interactions for three cases in the primary planes $M = 0$, $F_s = 0$ and $F_n = 0$. To compare with the previous API/Deepstar study (Andersen et al., 2003), all interaction surfaces are presented in Figs. 3.5, 3.6 and 3.7. The solutions obtained in the present study are in good agreement with the API/Deepstar curves. The $N_s : N_p$ curves in Fig. 3.5 drop abruptly at large values of N_p implying that parallel loading has little impact on the normal bearing capacity before it reaches $0.5\,F_{s\max}$, while the $N_m : N_p$ curves in Fig. 3.6 show a smaller negative slope

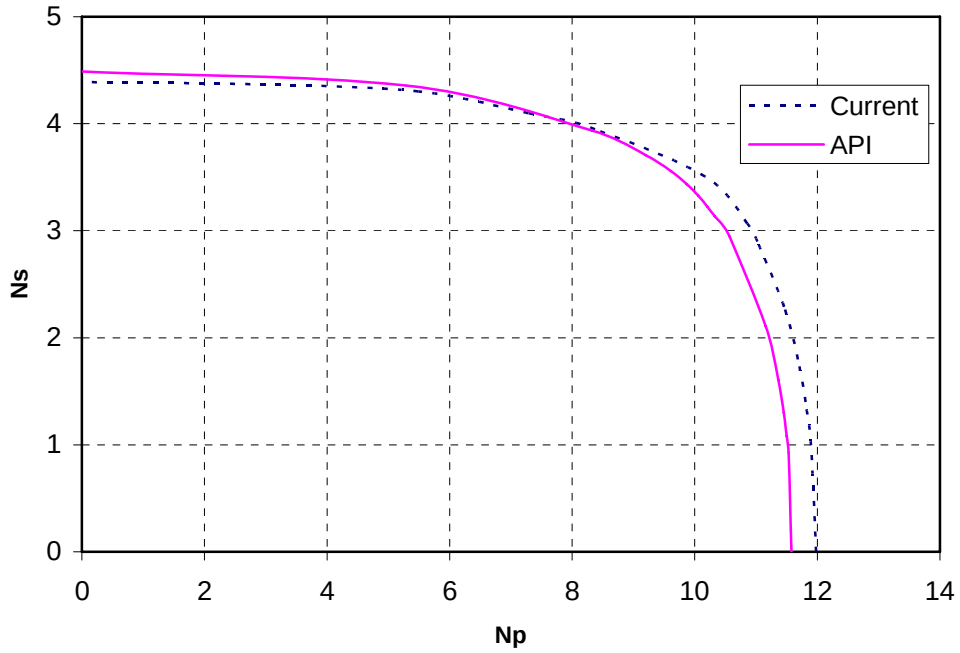

Fig. 3.5 Interaction surface for normal and parallel loading for plane strain conditions

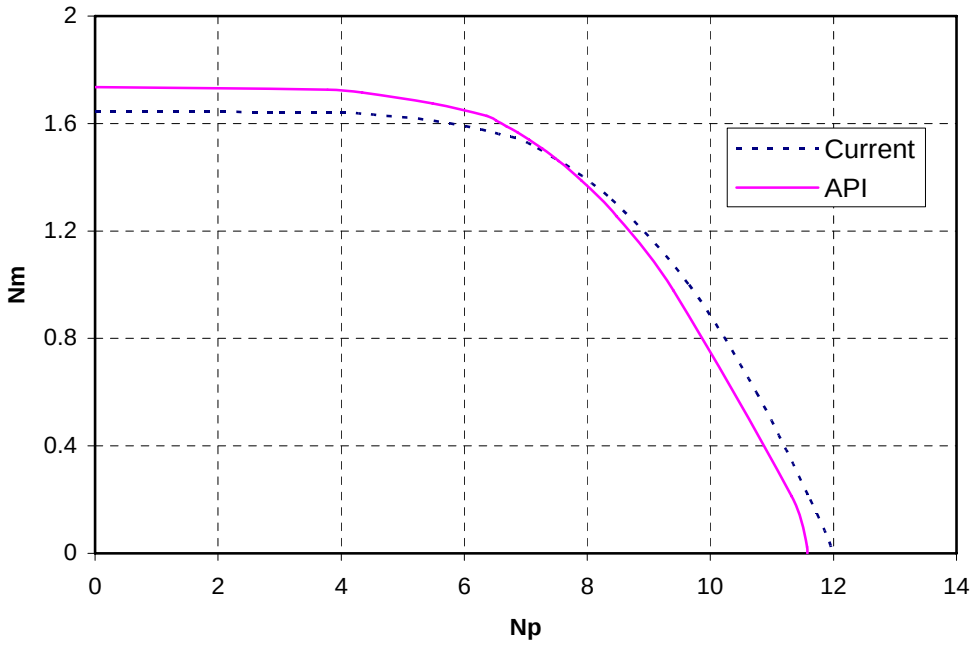

Fig. 3.6 Interaction surface for normal and moment loading for plane strain conditions

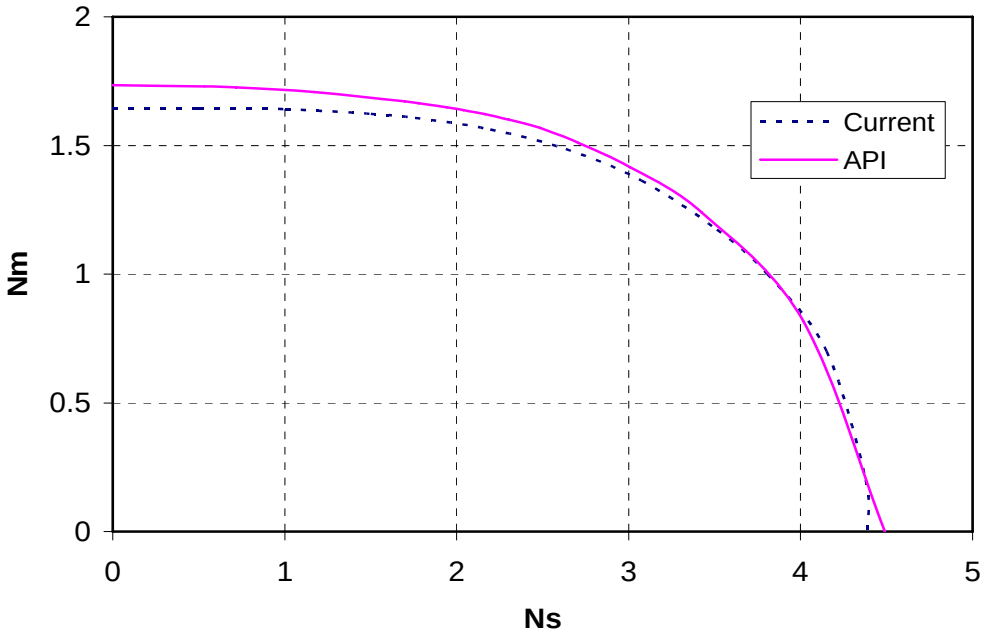

Fig. 3.7 Interaction surface for parallel and moment loading for plane strain conditions

implying the normal capacity is much more sensitive to rotation, and can thus be significantly reduced by a relatively small moment. For normal loads lower than $0.45\,F_{n\max}$, parallel loading as shown in Fig. 3.5, as well as moment loading as shown in Fig. 3.6, dominate the failure mechanism of the plate anchor. Compared to its impact on the normal capacity, the moment affects the parallel capacity a little less. It can be seen in Fig. 3.7 that the slope of the calculated curve is very steep for small moments, which indicates a slight rotation does not decrease the parallel capacity.

3.2.2.3 Empirical Interaction Model

The following interaction equation for plate anchors was proposed by Bransby and O'Neill (1999),

$$f = \left(\frac{F_n}{F_{n\max}} \right)^q + \left[\left(\frac{M}{M_{\max}} \right)^m + \left(\frac{F_s}{F_{s\max}} \right)^n \right]^{\frac{1}{p}} - 1 = 0 \qquad (3.2)$$

where F_n, F_s, and M are normal, shear or "parallel", and moment components of a combined loading at failure. $F_{n\max}$, $F_{s\max}$, and $M_{\max}$ are the failure values for pure normal, shear and moment load (i.e. without interaction), which can be calculated using Eq. 3.1. The exponents q, m, n and p are determined by a least squares fit of Eq. 3.2 to the finite element solutions. The values of m, n, p and q determined here (current study) and in the API/Deepstar study are tabulated in Table 3.2, respectively.

To show the effectiveness of Eq. 3.2, we plot the interaction surfaces compared with finite element results in Fig. 3.8-A, B, C. The two sets of results agree very well with each other. Eq. 3.2 can therefore be used to determine the multi-axial capacity of a plate anchor embedded within a given soil profile subjected to a generalized loading. The interaction surface described by Eq. 3.2 can itself be treated as a macroscopic yield surface (Prager, 1959) where forces and moments play the role of stresses and displacements and rotations play the role of strains (these stresses and strains must be work-conjugate pairs). Then the classic plastic stress-strain increment relationships can be employed to determine the displacement and rotation increment directions allowing the trajectory of a plate anchor to be incrementally predicted in this way. This is discussed in more detail in a subsequent section.

Table 3.2 Exponents in Eq. 3.2

Exponent	Current	API/Deepstar
m	1.56	1.40
n	4.19	3.49
p	1.57	1.32
q	4.43	4.14

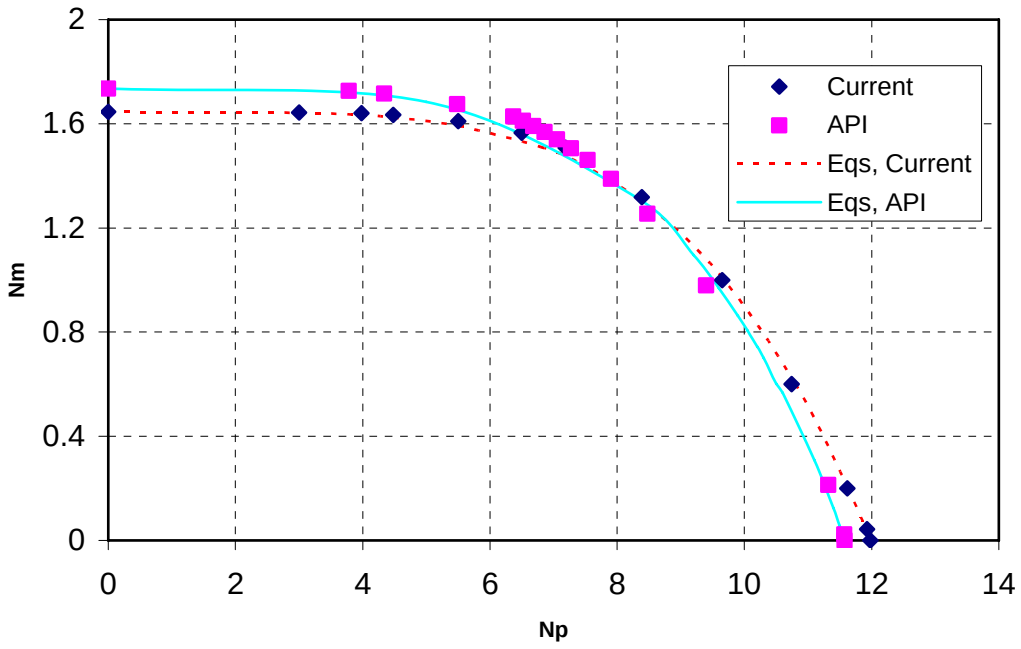

Fig. 3.8-A Results comparison of FEM and Eq. 3.2 for moment vs. normal load

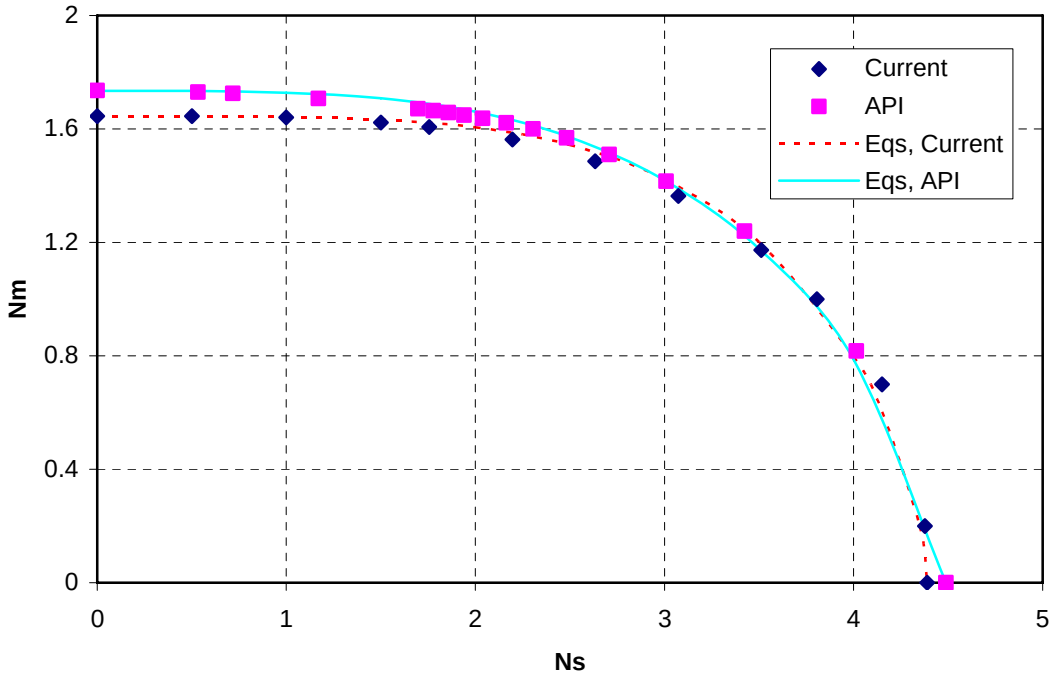

Fig. 3.8-B Results comparison of FEM and Eq. 3.2 for moment vs. parallel load

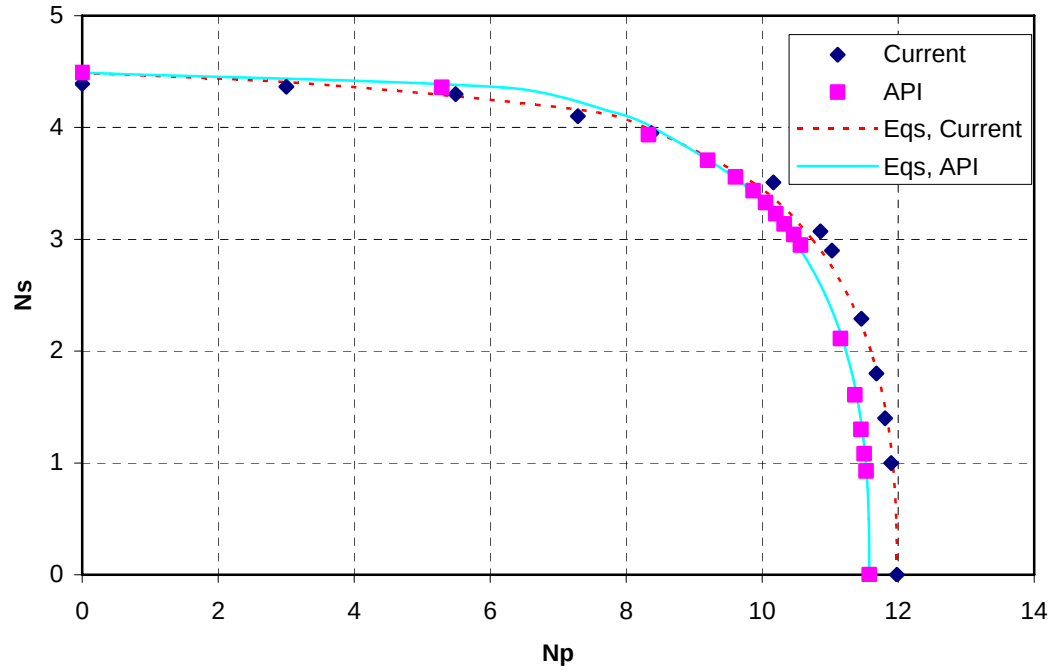

Fig. 3.8-C Results comparison of FEM and Eq. 3.2 for parallel load vs. normal load

3.2.2.4 Plastic Strain Contours

The development of a failure mechanism of the plate anchor can be demonstrated by plastic strain contours of the soil around it at various load intensities. As an example of the finite element results, Fig. 3.9-A, B and C show the case in which the plate anchor is subjected to a concentrated normal load acting at the centroid. The black rectangle is the plate anchor which is modeled as a rigid inclusion. In Fig. 3.9-A, the multicolored "wings" on either end of the plate indicate where the yielding has just started. The plastic yielding region of the soil progresses symmetrically on either side of the plate anchor such that significant portions of soil are involved (Fig. 3.9-B). Fig. 3.9-C shows the plastic strain where the soil is "flowing" around the plate anchor, indicating a complete plastic failure mechanism has formed as the failure load is reached. The dark blue triangles on either side of the plate are soil wedges that do not experience plastic strain but move essentially rigidly with the plate as it displaces. The maximum plastic strain occurs along the sides of the "rigid" soil wedges. This is exactly in accord with classical theory.

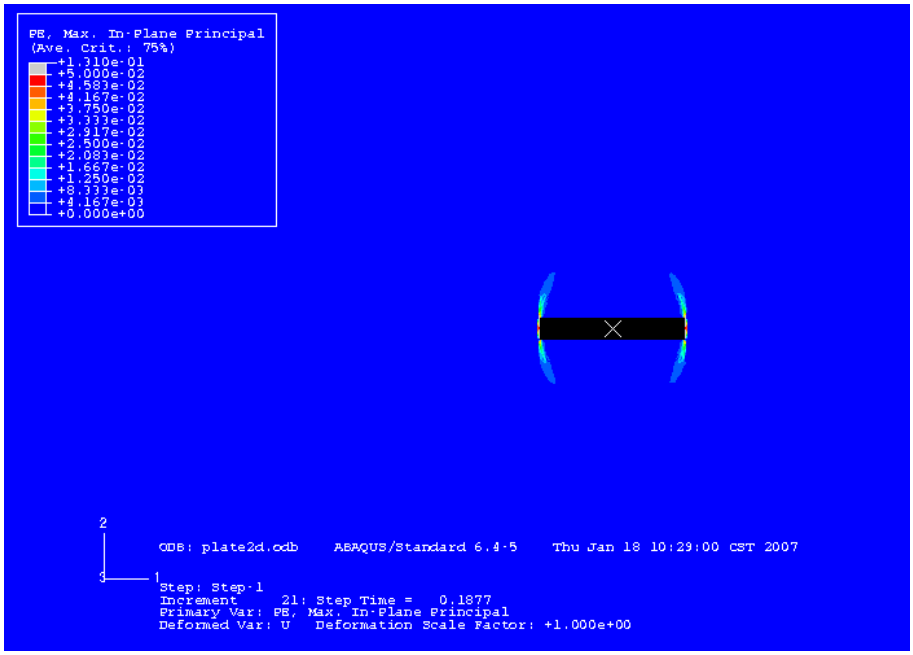

Fig. 3.9-A Plastic strain contours: initiation of yielding

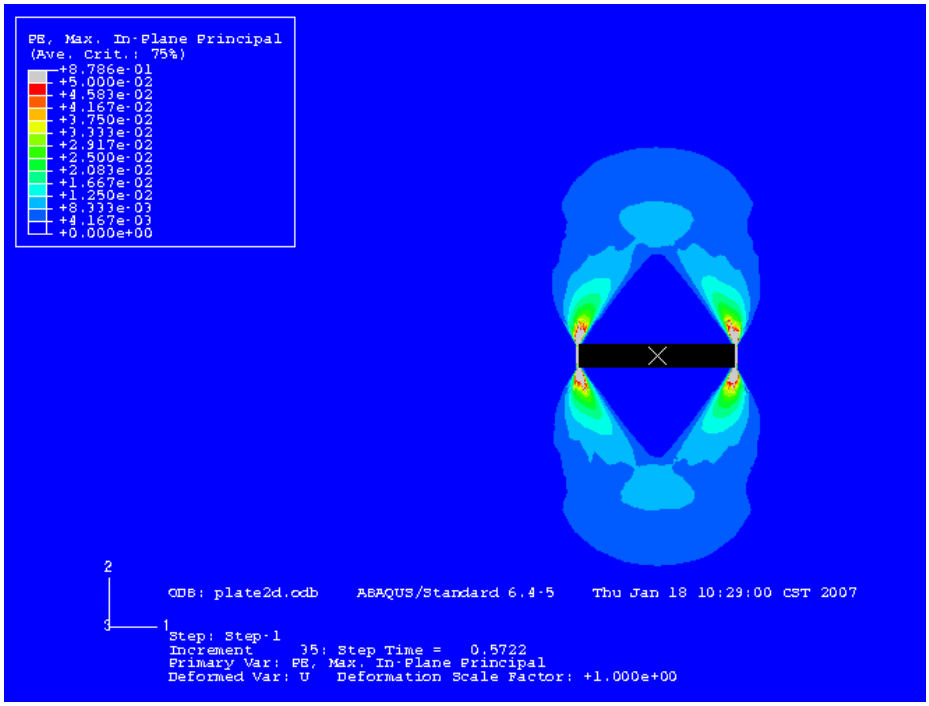

Fig. 3.9-B Plastic strain contours: progression of yielding

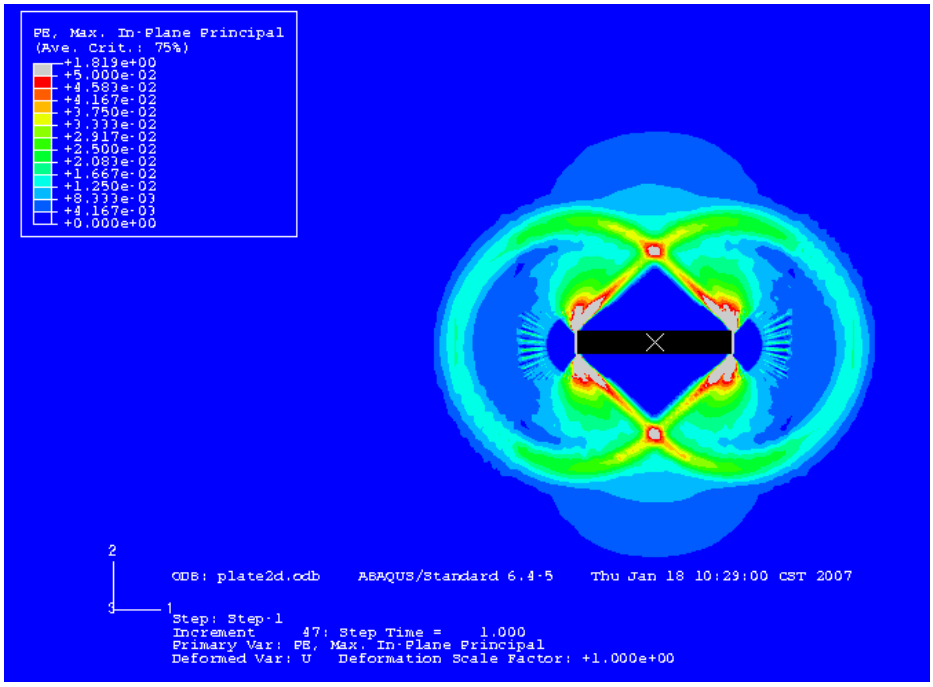

Fig. 3.9-C Plastic strain contours: incipient failure

3.3 Three-Dimensional Finite Element Analyses

3.3.1 3-D Finite Element Model

The general plate anchor problem must be modeled as a three-dimensional problem where the plate anchor is loaded eccentrically as shown in Fig. 3.10. A square plate anchor and a rectangular one (ratio of width to length of 2:1) were considered here. The width here is defined as the out-of-plane dimension of the plate. For this initial study, the thickness of plate anchors was assumed to be zero. As in 2-D analyses, the plate anchors are embedded in homogeneous soil under undrained conditions. It was again assumed that the soil obeys the von Mises yield criterion and associated flow rule with a uniform undrained shear strength S_u and the Young's Modulus $E = 500S_u$. The Poisson's ratio was taken to be 0.49 to simulate incompressible behavior of soil under

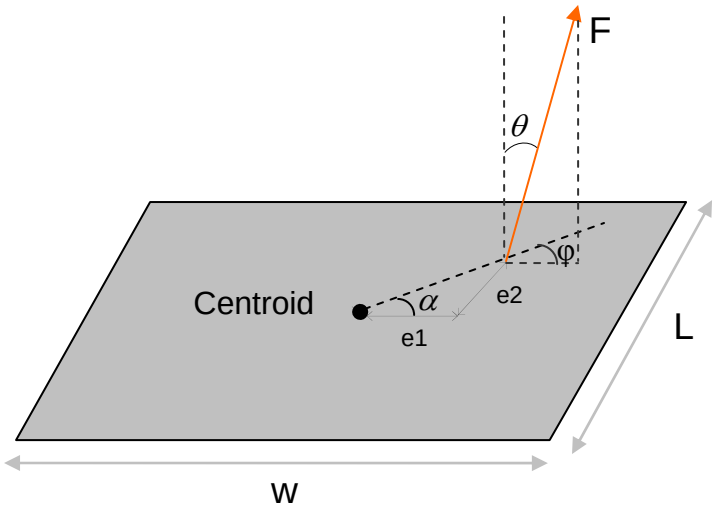

Fig. 3.10 Out-of-plane loading on plate anchor

undrained conditions. The plate anchors were considered as rigid bodies and assumed to be "fully" bonded to the soil around it.

The 8-node linear brick, hybrid elements were employed to generate the finite element mesh. It should be emphasized here how complex 3D modeling is. In a typical plate-soil model we used roughly 100,000 elements, with over 600,000 degrees of freedom. Because of this large model size one of the key issues in 3-D finite element analysis is how to minimize the run times while allowing enough mesh detail for accurate analysis. This requires that we use a fine mesh near the plate and a coarser one away from the plate where it has less influence. It is therefore very important that the transition from a dense mesh near the anchor to a coarse mesh at a distance is modeled as efficiently as possible. This directly affects the size of the model. One obvious approach to this problem is to use transition elements between the fine and coarse mesh such as a 4-node tetrahedron. However, this is computer time intensive. There are

several other ways to handle this in Abaqus, e.g. multi-point constraints, defining contact pairs and mesh tie constraints. The mesh tie constraints were used to make transition here. Compared to using the 4-node tetrahedron elements, automatically generated by Abaqus, the method of mesh tie constraints can reduce computer time by one-half in some cases and was therefore used in most of our analyses. Even with this added efficiency however, typical run times for a single analysis was on the order of 10 hours of SGI Altix 3700 computer time. As was done for the 2-D calculation, all analyses were performed under "displacement control" conditions, in which a translation or rotation was applied to the plate through the reference point (RP). A combination of several components of displacement was used to investigate the interactive behavior of the plate anchors under eccentric loading. To make the analyses of the square and the rectangular plate anchor comparable, the densities of mesh around each of them were set to be the same. The finite element mesh generated for plate anchors is shown in Fig. 3.11-A and B. Of course, a finer mesh may be used to obtain more accurate solutions, but even a small decrease in mesh size can result in large increases in computer time, especially for 3-D problems. The main purpose of this study is to define the interaction of forces acting on the anchor at failure. This was considered more important than the absolute value of the capacities so these finite element meshes were considered satisfactory. However, the absolute results were also compared with some known and approximate solutions and found to be in reasonable agreement.

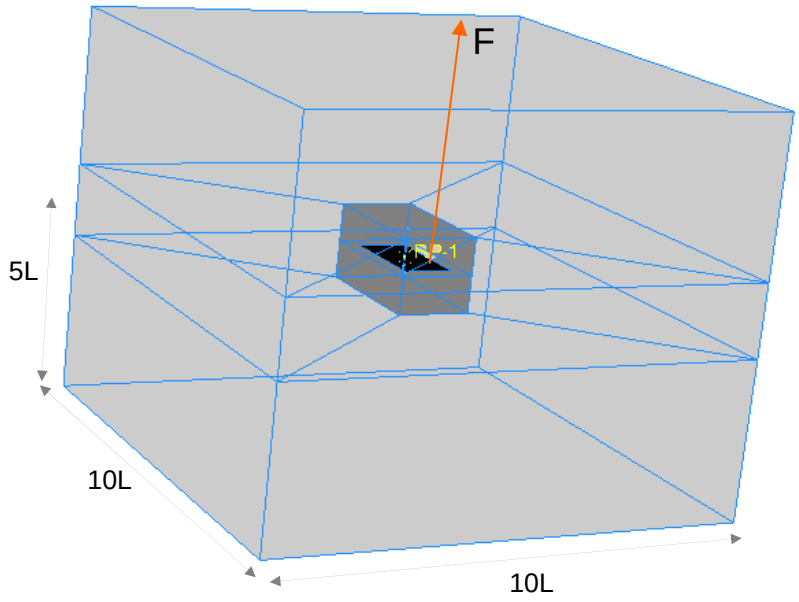

Fig. 3.11-A Finite element framework for vertically loaded plate anchor embedded in soil

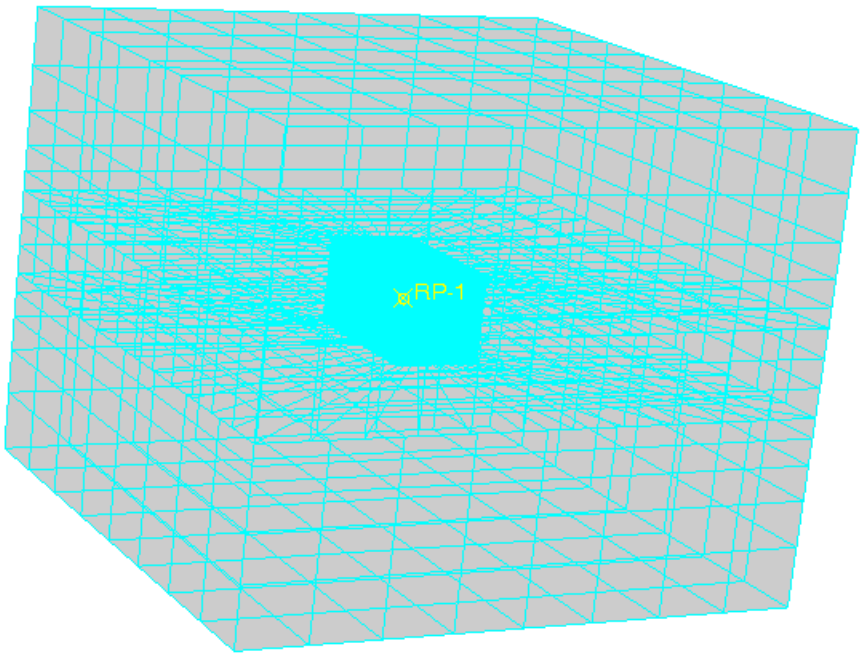

Fig. 3.11-B Detailed finite element mesh for 3-D analysis of plate anchor

3.3.2 3-D Finite Element Results for Square Plate Anchor

3.3.2.1 Bearing Capacities of Square Plate Anchor under Pure Loading

The capacities of the square plate anchor under undrained conditions are characterized by the non-dimensional factors as follows.

$$N_p = \frac{F_{n\max}}{L^2 s_u};\ N_s = \frac{F_{s\max}}{L^2 s_u};\ N_m = \frac{M_{\max}}{L^3 s_u};\ N_t = \frac{T_{\max}}{L^3 s_u} \tag{3.3}$$

where L is the length of a side of the square plate anchor; $F_{n\max}$, $F_{s\max}$, $M_{\max}$ and $T_{\max}$ are the pure normal, parallel, rotational and torsional capacities, respectively.

There are limited previous three-dimensional studies on the bearing capacities of plate anchors for comparison. Merifield et al. (2003) conducted three-dimensional lower bound finite element analysis for the bearing capacity of plate anchors under normal load. They did not consider the suction below the plate and obtained the normal bearing capacity factor of $N_p = 11.9$ for the square plate anchor. Gaudin et al. (2006) performed a series of centrifuge tests for suction embedded plate anchors and obtained the normal bearing capacity factors of square plate within a range of $N_p = 12.3 \sim 13.5$. Martin & Randolph (2001) performed lower and upper bound analysis for circular plate and obtained best estimates for normal bearing capacity factors of $N_p = 12.42$ and 13.11 for smooth and rough interfaces, respectively. Song & Hu (2005) carried out a finite element analysis for circular plate anchor with a thickness of 0.05D (D is diameter of circular plate) and obtained a solution of $N_p = 14.33$ for a rough interface. For the rotational case an upper bound solution is devised here for a circular plate assuming a spherical slip surface, shown as Fig. 3.12, which gives

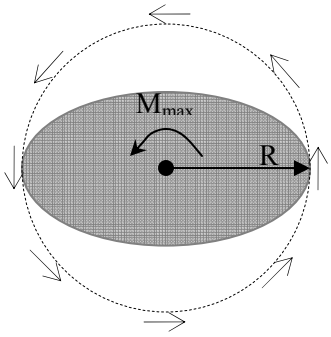

Fig. 3.12 Upper bound mechanism for circular plate

$$M_{\max} = \pi^2 R^3 s_u \tag{3.4}$$

where R is the radius of the circular plate. An approximate solution for a square plate can then be obtained by assuming that a square plate and a circular plate of the same area will have approximately the same moment capacity. An adjustment was made to the solution to account for the slightly larger moment of inertia of the square plate. The rotational capacity of $N_m = 1.9$ was thus estimated for the square plate anchor under pure moment about the major axes.

Fig. 3.13 and Fig. 3.14 show the finite element estimate for the responses of the square plate anchor under pure loadings. As in the plane strain analyses, the plate anchor begins with approximately linear elastic behavior until about 75% of the ultimate normal resistance and 90% of the ultimate moment resistance are mobilized. The curves approach a plateau before the normal displacement reaches 10% of the anchor length and the rotation reaches about 7°. The plateau values are taken to be the capacities of the plate anchor.

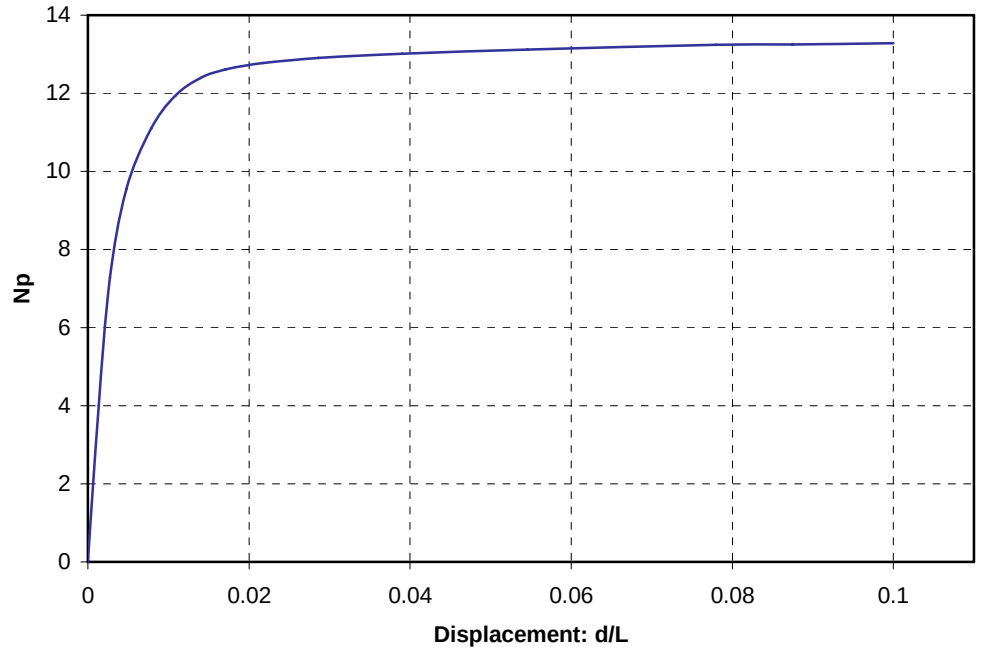

Fig. 3.13 Square plate anchor response under pure normal load

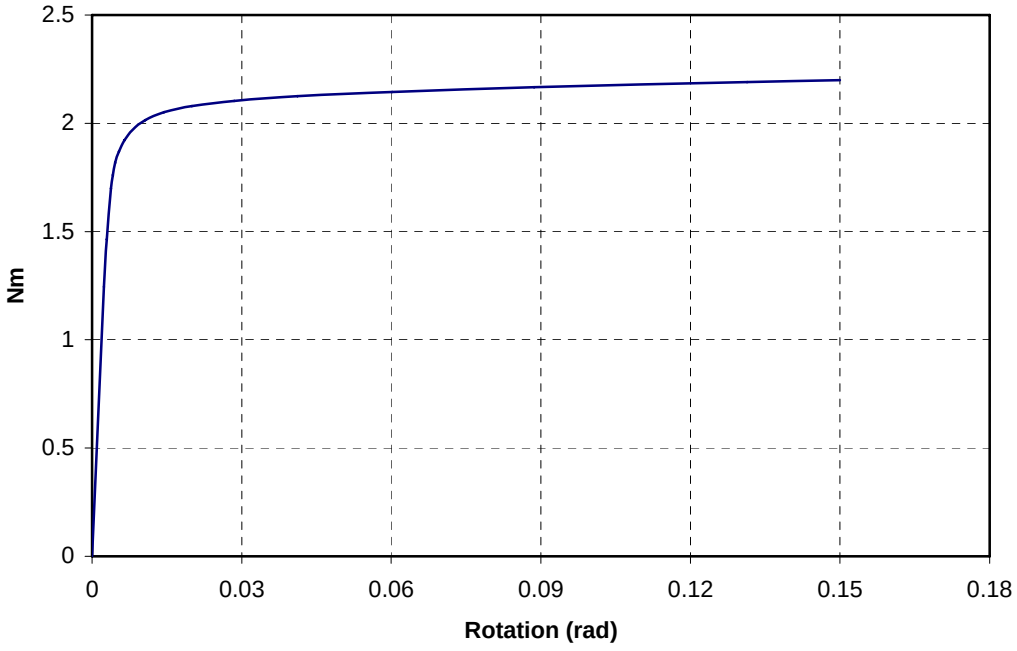

Fig. 3.14 Square plate anchor response under pure moment

Based on Martin & Randolph's solution (2001) for the circular plate, the theoretical solution for the normal capacity of the square plate is estimated to be between 12.5 and 12.8. The finite element prediction of $N_p = 13.28$ shown in Fig. 3.13 is then about 4-6% higher. We believe this is reasonable for 3-D finite element analysis. Compared with the estimated theoretical solution for moment capacity of $N_m = 1.9$, the finite element result of $N_m = 2.2$ shown in Fig. 3.14 overestimates about 16%. This difference is a little larger than typically obtained in these types of analyses. Some of this discrepancy is in fact due to the different geometries of the circular and the square plate although it not likely that the total difference can be attributed to geometry. Another likely contributor is the numerical effect arising from the stress concentrations that occur at the corners of the square plate in finite element analyses. As previously mentioned, the main aim of this study is to understand the overall interaction of forces acting on the plate when it fails, so the relative values of the forces at failure are more important for this purposes than the absolute values which can be calibrated using known solutions. These relative effects seem to be reasonably reflected in the finite element results.

As described in the discussion of the 2-D analyses, the parallel loading does not significantly reduce the normal capacity of the plate anchor before it reaches 50% of the ultimate value, so the current finite element work did not emphasize parallel loading. However, the parallel loading as well as torsion effects will be studied using upper bound method in a subsequent section.

3.3.2.2 Interaction Curves for Square Plate Anchor

The corner effect is believed to contribute to the difference in results between the square and the circular plate, so how the square behaves somewhat depends on the direction of eccentricity of the load. This is clearly not a factor for the circular plate. Fig. 3.10 shows a normal out-of-plane load acting on the plate anchor if assuming $\theta = 0$. The out-of-plane loading can thus be considered as a combination of a normal load acting at the centroid of the plate and a moment perpendicular to the direction that the load is offset from the centroid (or two components of the moment about the major axes simultaneously acting at the centroid of the plate anchor). As a load normal to the plate is displaced from the centroid in a specific direction, the displacement of the plate anchor will transition from a pure translation to a pure rotation as the load offset approaches infinity. That is, the plate will experience three corresponding stages in the following order: pure normal translation, translation combined with rotation and pure rotation. The capacities of the plate anchor under out-of-plane loading over this range can be described by failure interaction curves.

Due to the 8-fold symmetry of the square plate anchor, we only need consider here the region from a major axis to a diagonal of the plate i.e. $\alpha = 0^\circ$ to $\alpha = 45^\circ$ as shown in Fig. 3.10 (α here is different from the optimization variable α used in upper bound calculations). The interaction curves presented in Fig. 3.15 correspond to four different directions along which the normal load was moved. It can be seen that the rotational capacity of the square plate anchor does not change significantly when the direction of the load varies from the major axis ($\alpha = 0^\circ$) to the diagonal ($\alpha = 45^\circ$). The maximum

variation is less than 3%. This indicates that the direction from the centroid does not have a significant effect on the behavior of the square plate anchor. Therefore, it seems reasonable that an approximate solution for the square plate is obtained by adjusting the upper bound solution for the circular plate. Fig. 3.15 also shows that the interaction curves begin with an approximate plateau, that is, the moment capacity is unaffected by the normal load until the normal load is about 40% of its maximum value. After this the curves show that the normal capacity of the plate anchors is very sensitive to rotation, and can thus be significantly reduced by even a small moment. The curves almost overlap where N_m is less than 60% of its maximum value. The overlapping part indicates that the failure mechanism of the plate anchor is not affected by the load direction from the centroid at all when it is loaded within this region.

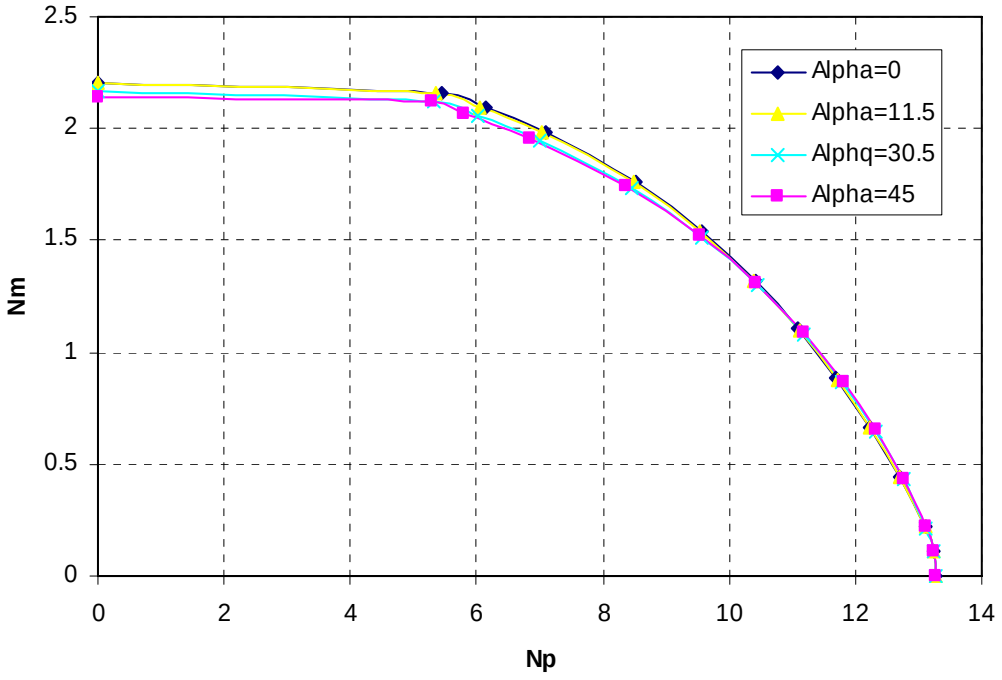

Fig. 3.15 Interaction of normal load and moment for square plate anchor

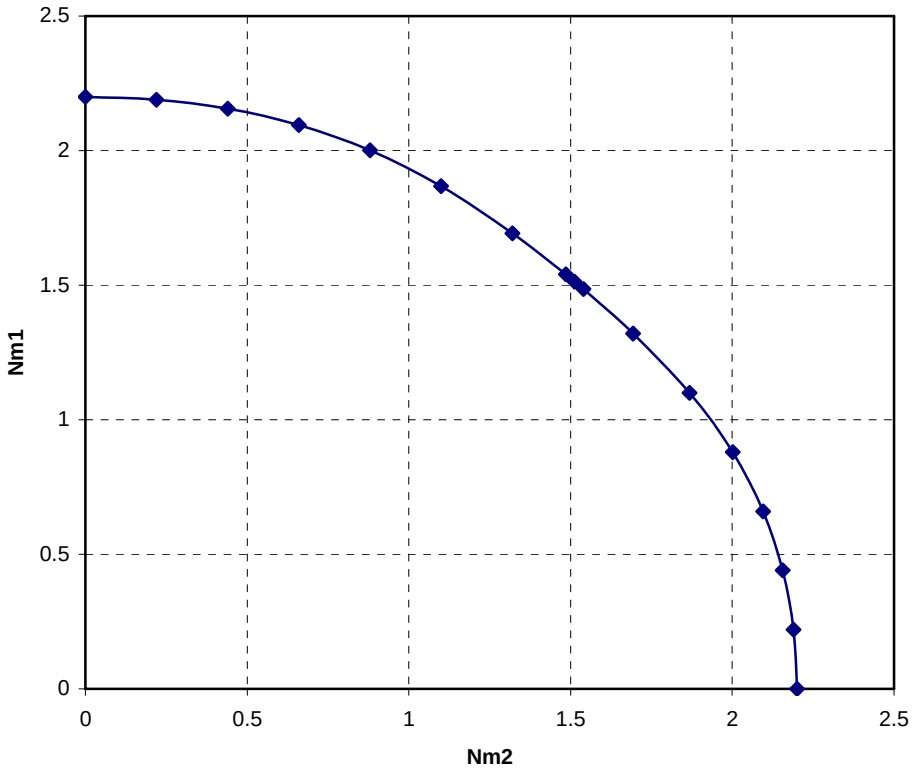

Fig. 3.16 Interaction of moments for square plate anchor

Fig. 3.16 shows the interaction curve for moment components about the major axes of the square plate anchor. As described above, the variation in the rotational capacity is less than 3% for different axis, so the interaction curve shown in Fig. 3.16 is very close to a circle.

3.3.2.3 Interaction Model for Normal Load and Moment on Square Plate Anchor

The interaction curves based on the FE analyses may be fitted by a single mathematical function in F_n - M_1 - M_2 space. The following interaction model for the square plate anchor, obtained by adjusting the Bransby & O'Neill (1999) equation, gives a good fit to the FE results,

$$f = \left(\frac{F_n}{F_{n\max}} \right)^q + \left(\frac{M_1^m + M_2^m}{M_{\max}^m} \right)^{\frac{1}{p}} - 1 = 0 \qquad (3.5)$$

where F_n, M_1 and M_2 are the normal and moment components of a combined loading at failure; $F_{n\max}$ and $M_{\max}$ are the ultimate values for pure normal and moment load and determined by Eq. 3.3 where $N_p = 12.5$ and $N_m = 1.9$. These values are estimated by known solutions to related problems, upper bound analyses and FE results. The exponents in Eq. 3.5 were determined by a least squares fit and are tabulated in Table 3.3. The interaction model described by Eq. 3.5 is plotted in three-dimensional space in Fig. 3.17. This three-dimensional plot represents the yield surface (it is also the plastic potential surface for associated flow rule calculations) for the square plate anchor subjected to eccentric normal loading.

For a vertically loaded plate anchor, i.e. $\theta = 0$ in Fig. 3.10, an out-of-plane load F can be represented as a normal load of F_n at the centroid and a moment

$$M = F_n \cdot e = F_n \cdot \sqrt{e_1^2 + e_2^2} \qquad (3.6)$$

or its two components about the major axes

$$M_1 = F_n \cdot e_1 \qquad (3.7)$$

and $$M_2 = F_n \cdot e_2 \qquad (3.8)$$

Table 3.3 Exponents in Eq. 3.5

Exponent	m	p	q
Value	1.91	1.56	3.26

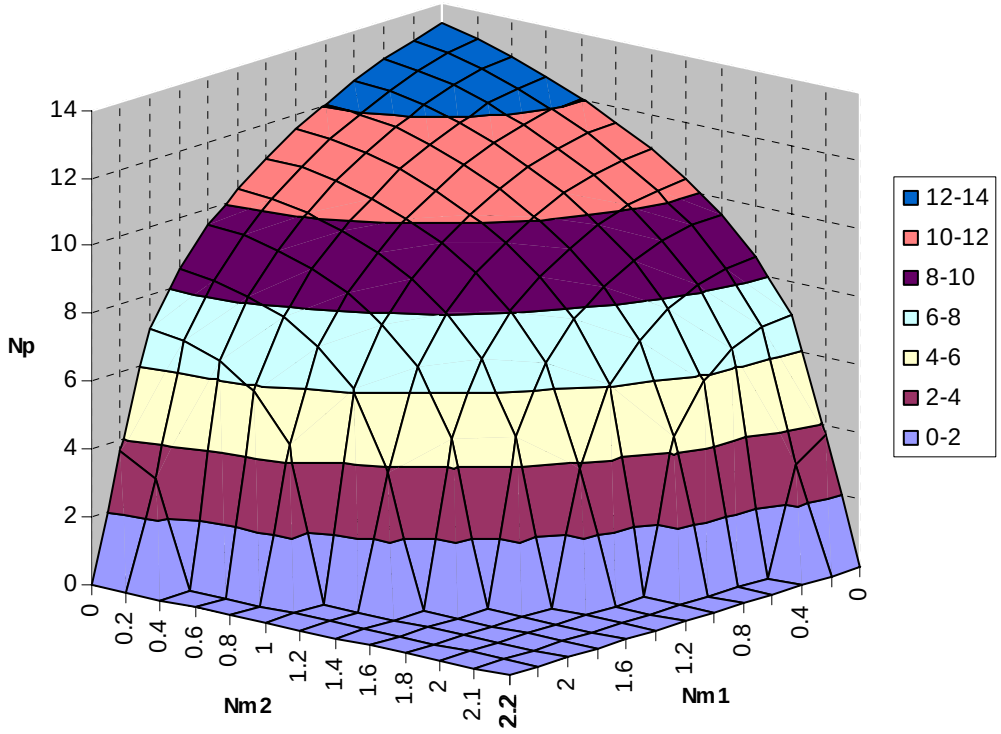

Fig. 3.17 Multi-axial yield surface for the square plate anchor

Given load eccentricities of e_1 and e_2, the capacity of the square plate anchor embedded in a soil with a specified strength profile can be determined by substituting Eqs 3.7 and 3.8 into Eq. 3.5 and solving for F_n. To demonstrate how the capacity of the anchor varies when it is vertically loaded at different locations, it is assumed that the load moves radially outward from the centroid in a specific direction. Fig. 3.18 shows the non-dimensional capacity of the anchor for any eccentricity direction. Clearly the moment can have a major effect in decreasing anchor holding capacity. These curves essentially overlap each other since the exponent m is very close to 2 (where they would exactly overlap). As the load direction changes from the major axis ($\alpha = 0^\circ$) to the diagonal ($\alpha = 45^\circ$), the maximum decrease in capacity for a given eccentricity is less than 1.6%.

This again indicates that the corner effect has little effect on the normal capacity of the square plate anchor.

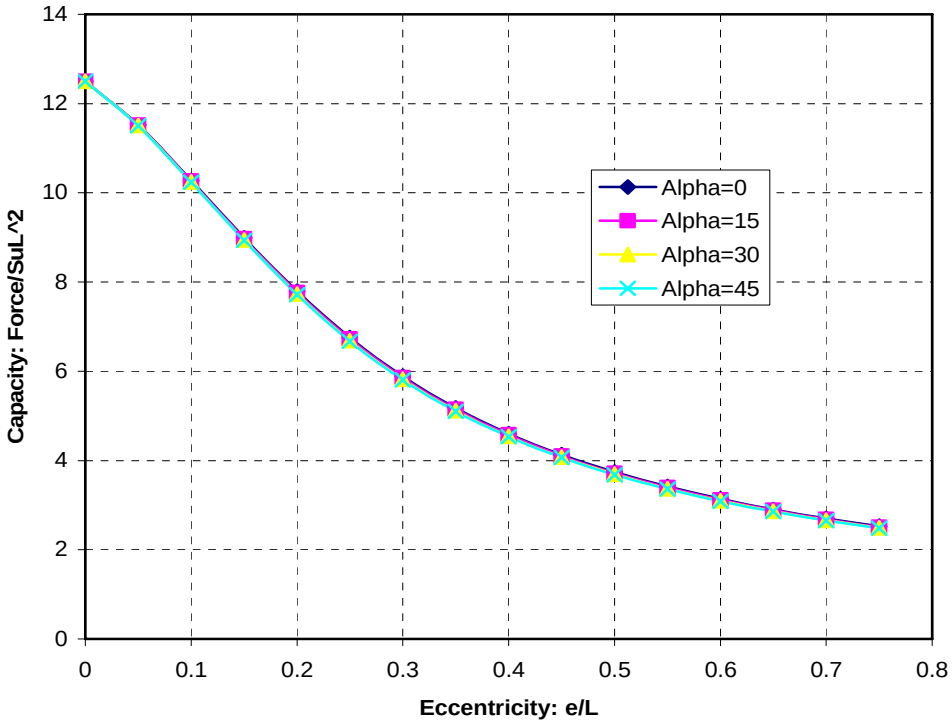

Fig. 3.18 Capacity of the square plate anchor vertically loaded with the eccentricity of *e*/*L*

3.3.3 3-D Finite Element Results for Rectangular Plate Anchor

3.3.3.1 Bearing Capacities of Rectangular Plate Anchor under Pure Loading

The bearing capacities of the rectangular plate anchor in undrained soil can be characterized using the non-dimensional factors as follows,

$$N_p = \frac{F_{n\max}}{LWs_u};\ N_s = \frac{F_{s\max}}{LWs_u};\ N_{m1} = \frac{M_{1\max}}{L^2Ws_u};\ N_{m2} = \frac{M_{2\max}}{LW^2s_u};\ N_t = \frac{T_{\max}}{L^2Ws_u} \qquad (3.9)$$

where L and W are the length and width of the rectangular plate anchor; $F_{n\max}$, $F_{s\max}$, $M_{1\max}$, $M_{2\max}$ and $T_{\max}$ are the ultimate normal and parallel resistances, ultimate moment resistances about the long and short major axes and ultimate torsional resistance of the rectangular plate anchor, respectively.

The aspect ratio of the plate (width to length) accounts for the difference in bearing capacities between the rectangular anchor and the square one. When the ratio is large enough, the end effects can be ignored such that the problem of normal loading or moment loading about the long axis of the plate becomes a plane strain problem. That is, the normal capacity factor of the rectangular plate anchor ranges from the plane strain problem to the square one. The rotational capacity factor for a finite length, rectangular plate about the short (or long) major axis is greater (or less) than the one for the square plate anchor. Unfortunately, there have been few previous studies performed on the behavior of a rectangular plate. Here upper bound solutions are firstly devised for the pure normal loading and moment loading about the long major axis. It is assumed that the "flow around" mechanism, shown in Fig. 2.4, for the plain strain condition applies to the finite length, rectangular plate, allowing for the end effect that is contributed by the energy dissipation along slip surfaces between the plastic flow and the rigid soil on the two ends. The upper bound calculations give solutions for the normal loading of the rectangular, 2:1, plate as follows

$$N_p = (\pi - \alpha)(4 + \frac{1}{4\cos^2\alpha \sin\alpha}) + 2.5\tan\alpha \qquad (3.10)$$

where the minimum value of $N_p = 13.49$ is reached if the parameter α is taken to be

38.62°. The solution for moment loading about the long axis for the rectangular, 2:1, plate is as follows

$$N_{m1} = \frac{7\pi}{12} \approx 1.83 \tag{3.11}$$

Moment loading about the short major axis of the plate is a more complex problem and a simple bound solution has not yet been developed.

To make the FE results comparable, we used the same density mesh that was used for the analyses for the square plate. The finite element predictions for the response of a rectangular plate anchor with a width to length ratio of 2:1 under pure normal or moment loading are presented in Figs 3.19, 3.20 and 3.21. Fig. 3.19 shows that the normal capacity factor N_p approaches a plateau of 13.12, 2.8% lower than the upper

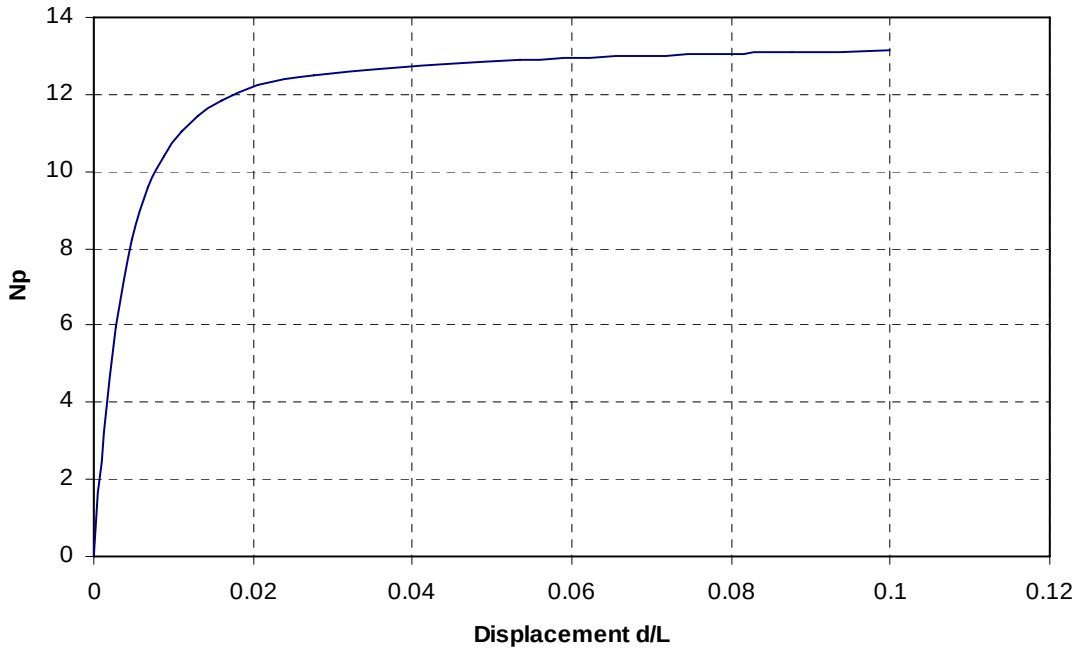

Fig. 3.19 Plate anchor response under pure normal load for a rectangular plate (W/L=2)

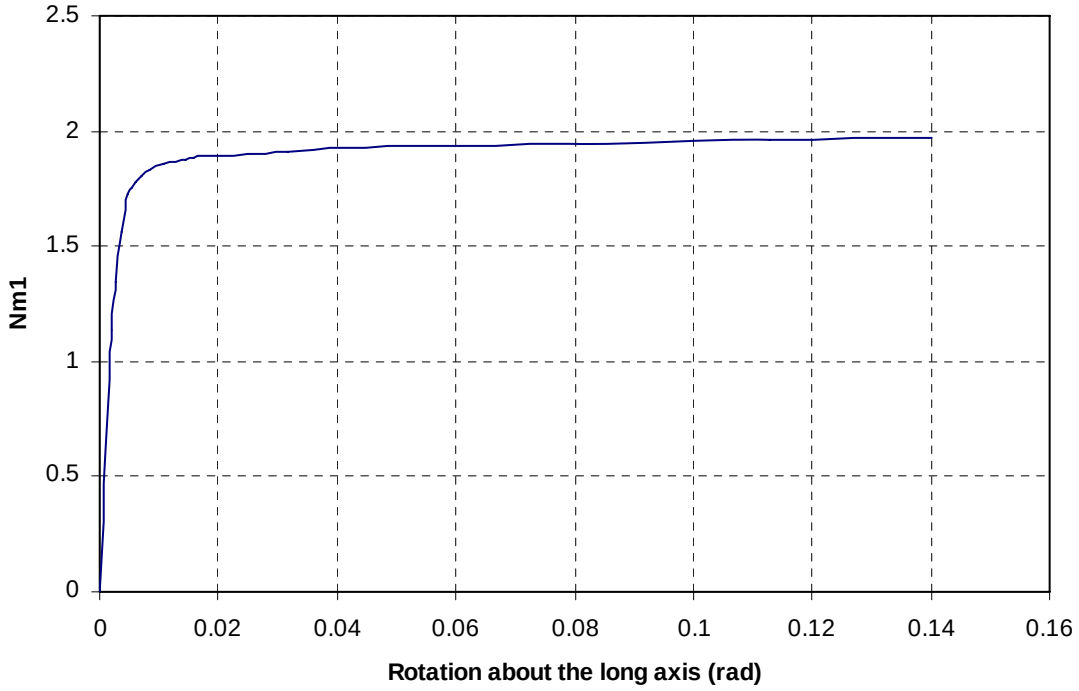

Fig. 3.20 Plate anchor response under pure moment about the long axis for a rectangular plate (W/L = 2)

bound solution of 13.49, before the displacement reaches 10% of the anchor length. The rotational capacity factors N_{m1} and N_{m2} reach their ultimate values of 1.97 and 2.50 at an anchor rotation of about 5° as shown in Figs 3.20 and 3.21. Here $N_{m1} = 1.97$ is 7.7% higher than the upper bound solution of 1.83. These solutions seem to be consistent compared to the finite element analyses for the square plate anchor. Because the density of the finite element mesh used herein is the same as was used in the analyses for the square plate, it is assumed that the finite element results overestimate the real solutions by approximately the same amount, e.g. the normal capacity of $N_p = 13.12$ is assumed

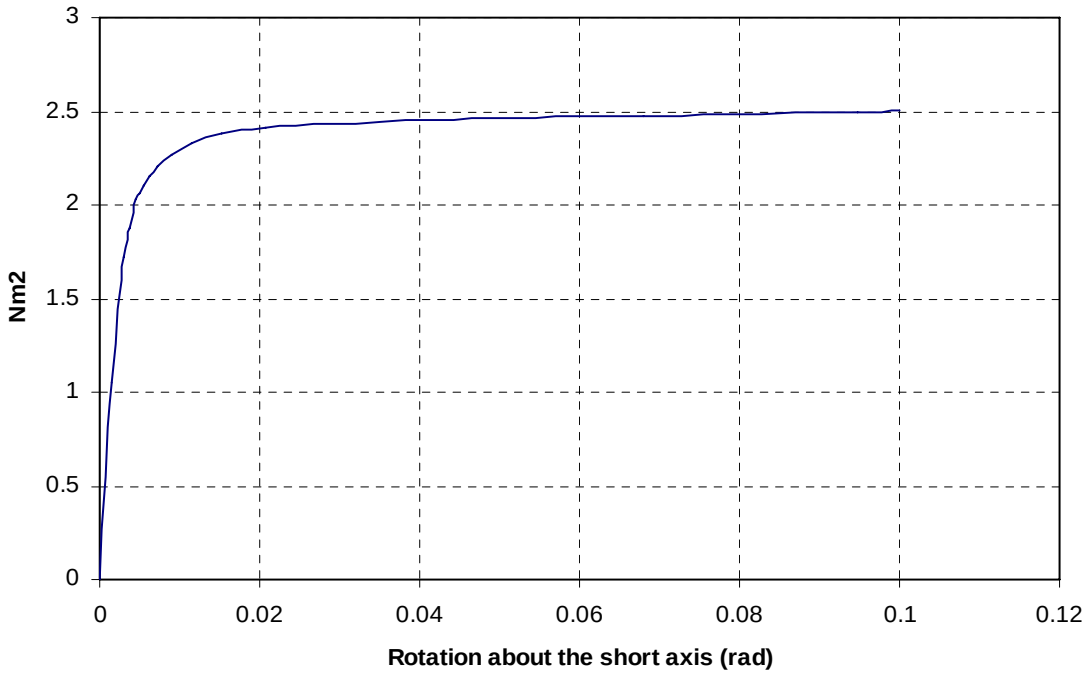

Fig. 3.21 Plate anchor response under pure moment about the short axis for a rectangular plate (W/L = 2)

to be 4%-6% higher, and the rotational capacities of $N_{m1} = 1.97$ and $N_{m2} = 2.50$ are assumed to be 16% higher. Thus we estimate for the rectangular, 2:1, plate that $N_p = 12.35$, $N_{m1} = 1.7$ and $N_{m2} = 2.15$. This results in N_p and N_{m1} being 8.5% and 7% lower than their upper bound solutions. As mentioned previously, the main purpose here is to obtain the overall interaction behavior among the forces acting on the plate and these solutions are considered satisfactory for that purpose.

3.3.3.2 Interaction Curves for Rectangular Plate Anchor

As was previously done for the square plate anchor, the finite element analysis

results were generated by applying the normal load at varying distances from the centroid of the rectangular plate anchor along a specific direction at an angle α from the short major axis. Due to the four fold symmetry of the rectangular plate, the load was applied over only one quarter of the anchor (from $\alpha = 0^{\circ}$ to $\alpha = 90^{\circ}$). The finite element analyses were performed for the following five cases: $\alpha = 0^{\circ}$, $\alpha = 43^{\circ}$, $\alpha = 63^{\circ}$, $\alpha = 76^{\circ}$ and $\alpha = 90^{\circ}$. Fig. 3.22 shows the interaction behavior of the normal load and moment for the cases described above. It can be seen that the five curves almost overlap for N_m less than 0.4, showing that the anchor capacity at a small eccentricity is not very sensitive to the angle α. The aspect ratio of the rectangular plate anchor contributes to the separation of the curves in which the value of N_m increases up to 27% from $\alpha = 0^{\circ}$ to $\alpha = 90^{\circ}$ for

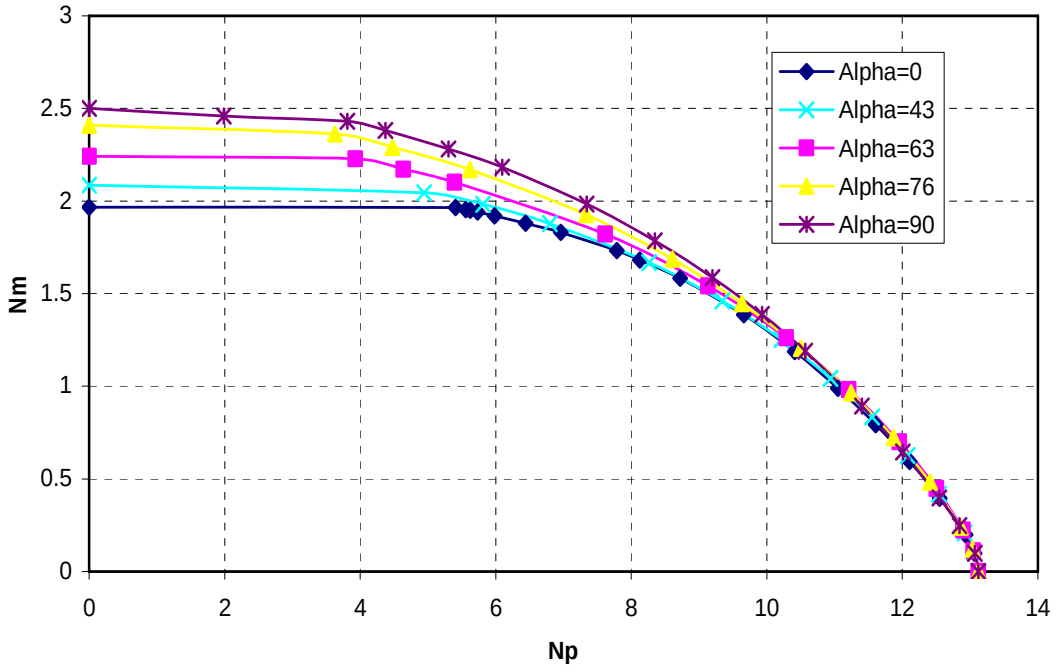

Fig. 3.22 Interaction of normal load and moment for a rectangular plate anchor (W/L = 2)

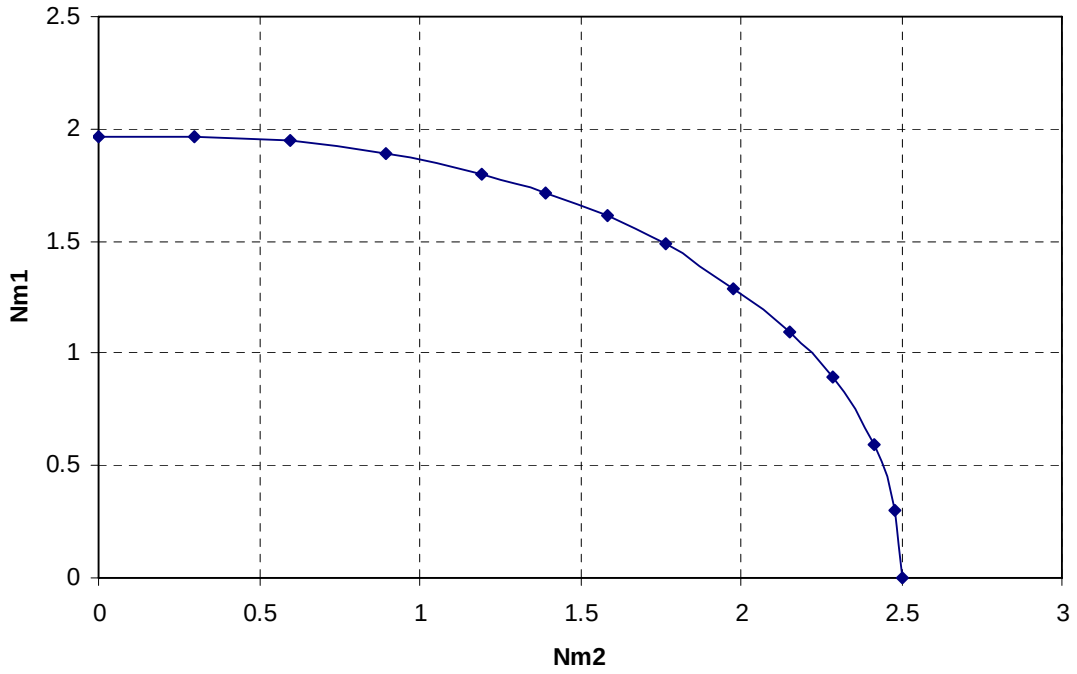

Fig. 3.23 Interaction of two components of the moment for a rectangular plate anchor ($W / L = 2$)

$N_p = 0$. These interaction curves have an approximate plateau for small N_p, i.e. where the moment governs the failure mechanism of the anchor. The plateau becomes shorter as the angle α changes from 0° to 90°. The negative slopes of the curves indicate that the normal capacity of the anchor is sensitive to the eccentricity, and can be reduced significantly by even a small value. Fig. 3.23 shows the interaction between the components of the moment about the short and long axis of the rectangular plate anchor ($N_p = 0$). It is observed that the rotational capacities about two major axes are very sensitive to each other.

3.3.3.3 Interaction Model for Normal Load and Moment on Rectangular Plate Anchor

As was done for the plane strain and the square plate problem, an equation was used to describe the interaction of forces acting on the plate. Not including the parallel and torsional loadings, this empirical equation is written in the following form.

$$f = \left(\frac{F_n}{F_{n\max}}\right)^q + \left[\left(\frac{M_1}{M_{1\max}}\right)^{m1} + \left(\frac{M_2}{M_{2\max}}\right)^{m2}\right]^{\frac{1}{p}} - 1 = 0 \qquad (3.12)$$

where F_n, M_1 and M_2 have the same physical meanings as in Eq. 3.5; $F_{n\max}$, $M_{1\max}$ and $M_{2\max}$ are ultimate pure normal loading and moments that can be calculated from Eq. 3.9 in which $N_p = 12.35$, $N_{m1} = 1.7$ and $N_{m2} = 2.15$. A least squares fit of Eq. 3.12 to the finite element results gives the values of the exponents, *m*1, *m*2, *p* and *q*, which are tabulated in Table 3.4.

As for the square plate anchor, we have

$$M_1 = F_n \cdot e_1 \text{ and } M_2 = F_n \cdot e_2 \qquad (3.13).$$

The normal capacity of the rectangular anchor, F_n, can be obtained by substituting Eq. 3.13 into Eq. 3.12 and then solving Eq. 3.12 for F_n. To demonstrate how the normal capacity is affected by the load eccentricity, it is again assumed that the load is offset from the centroid to the edge along a path at an angle α with the short major axis.

Table 3.4 Exponents in Eq. 3.12

Exponent	m1	m2	p	q
Value	2.47	1.86	1.93	3.20

Fig. 3.24 shows the predicted variation in non-dimensional capacity of the rectangular plate anchor along six different paths, which are $\alpha = 0^{\circ}$, $\alpha = 30^{\circ}$, $\alpha = 45^{\circ}$, $\alpha = 63.4^{\circ}$, $\alpha = 75^{\circ}$ and $\alpha = 90^{\circ}$. In this case e is the resultant eccentricity in that direction such that e/L represents the normalized distance from the centroid. It can be seen that the capacity of the rectangular plate anchor is very sensitive to the direction of load eccentricity. It decreases most slowly along the long major axis ($\alpha = 90^{\circ}$) and most rapidly along the short major axis ($\alpha = 0^{\circ}$). At the same distance from the centroid, the capacity increases more than 100% from $\alpha = 0^{\circ}$ to $\alpha = 90^{\circ}$ after $e/L > 0.5$.

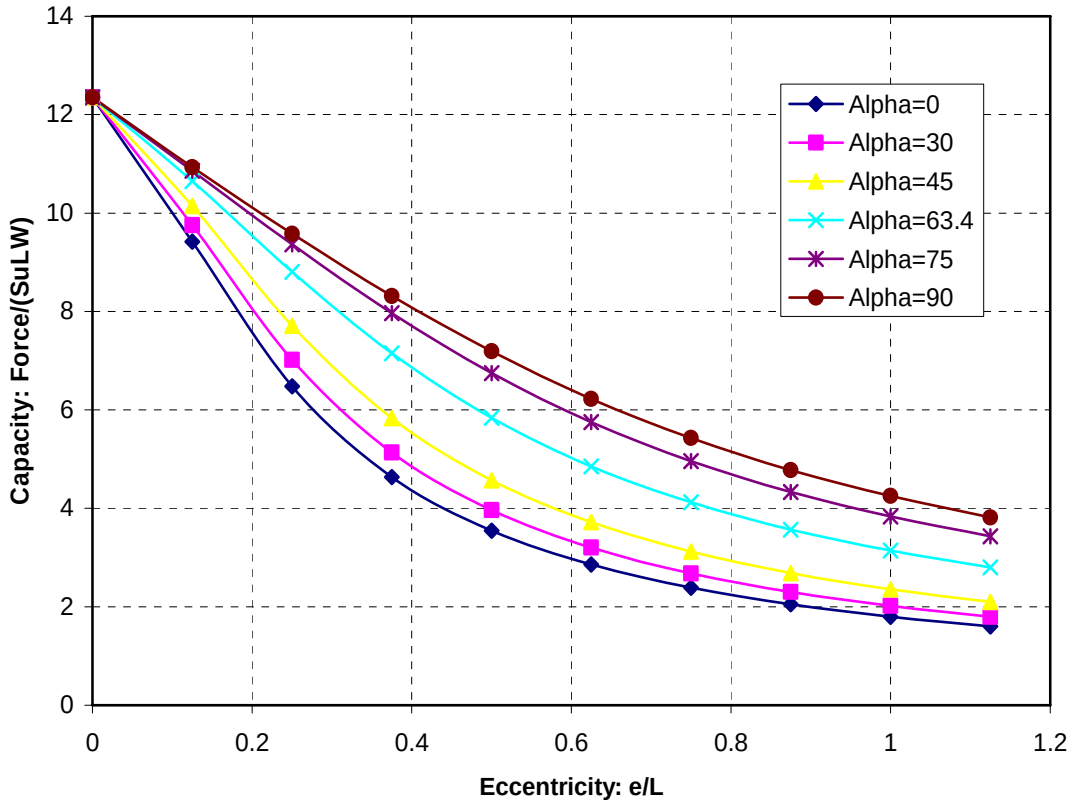

Fig. 3.24 Capacity of the rectangular plate anchor loaded eccentrically in various offset directions

3.3.4 Comparison of Model Predictions with Experiment

To complement the analytical work and provide consistent, repeatable and controlled results, a parallel model-scale laboratory investigation was conducted on the out-of-plane loading of plate anchors by another group at the University of Texas at Austin. The model plate anchors were fabricated from steel plate, and their dimensions were 4 x 4 x 0.25 inches and 4 x 8 x 0.25 inches. Threaded holes were drilled at the desired locations to accommodate the centered or eccentric loading. The plate was then mounted with a 3/16 -inch diameter eye bolt to attach the loading cable. The square and rectangular plates weighed about 1 pound and 2 pounds, respectively. The model plate anchors were embedded in kaolin clay with uniform undrained shear strength that was measured for each loading test using the T-bar method. The eccentricity was taken to be 1/4 or 1/2 the width of the respective plate to account for out-of-plane loading.

The model predictions and experimental results for anchor capacity factors are compared in Table 3.5, which are shown to be in reasonably good agreement with each other. The average capacity factors of the square and rectangular plate under pure normal loading are both $N_p = 12.4$ measured by the experiment whereas $N_p = 12.5$ for the square plate and $N_p = 12.35$ for the rectangular plate are estimated by the analytical model. The comparisons are shown graphically for various out-of-plane loadings in Fig. 3.25. It is found that the measured values for capacity factors are generally within $\pm 10\%$ of the theoretical predictions, which is well within the repeatability of the tests. Therefore, the theoretical interaction model is considered to be reasonable in predicting the capacity of plate anchors subjected to out-of-plane loading.

Table 3.5 Summary of Anchor Capacity Factors by Experiment and Interaction Model

Test No.	Plate Geometry	Eccentricity of Loading Force e/L, α (deg)	Embedment Depth (in)	Pullout Test Results			Theoretical Capacity Factor
				Interpreted Soil Strength (psf)	$F_{max} - W'_{plate}$	Capacity Factor	
1	Square	0, 0	12	10.6	13.1	11.2	12.5
2	Square	0, 0	16	13	19.8	13.8	12.5
3	Square	0, 0	12	14.1	18	11.6	12.5
4	Square	0, 0	12	14.1	17.5	11.3	12.5
5	Square	0, 0	12	14.1	17.9	11.5	12.5
6	Square	0, 0	12	15	21.5	13.0	12.5
7	Square	0, 0	12	16	24.6	14.0	12.5
8	Square	0, 0	12	18	24.8	12.5	12.5
9	Square	0, 0	12	19.5	27.7	12.9	12.5
10	Square	0, 0	12	20	25.6	11.6	12.5
11	Square	0, 0	12	23	31.8	12.6	12.5
12	Rectangular	0, 0	18	19	45.2	10.8	12.35
13	Rectangular	0, 0	12	19.5	60	14.0	12.35
14	Square	0.25, 0	12	10	6.5	5.9	6.8
15	Square	0.25, 0	12	10.3	7.7	6.8	6.8
16	Square	0.25, 0	12	14.1	7.7	5.0	6.8
17	Square	0.25, 0	12	23	17.4	6.9	6.8
18	Square	0.35, 45	12	21	15.3	6.6	5.1
19	Rectangular	0.25, 90	18	17.5	26.9	7.0	6.4
20	Rectangular	0.25, 90	12	18.5	30.2	7.4	6.4
21	Rectangular	0.5, 0	12	24.3	33.2	6.2	7.2
22	Rectangular	0.5, 0	12	25.5	32.1	5.7	7.3

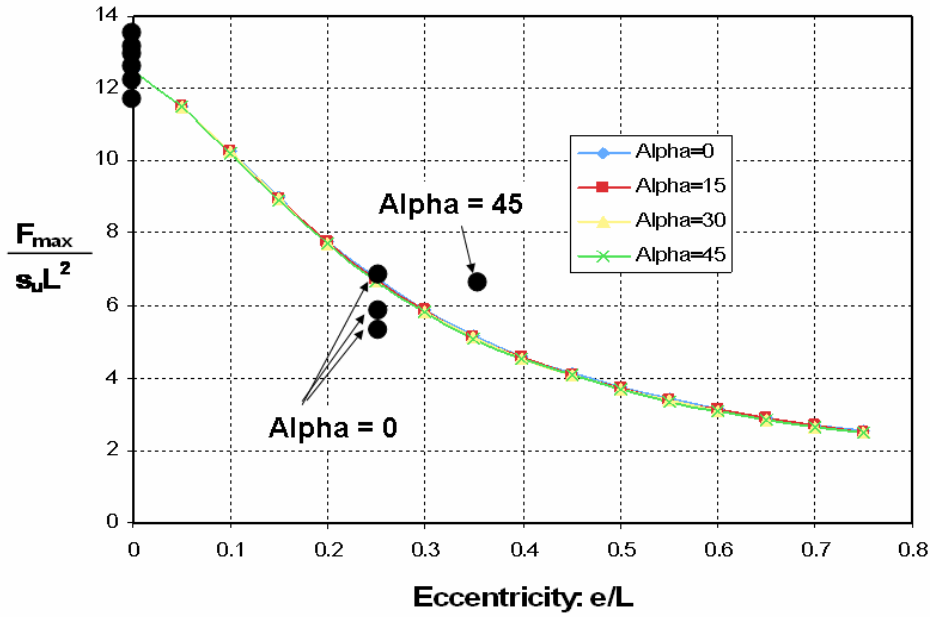

Fig. 3.25-A Comparisons of model predictions and experiment for square plate

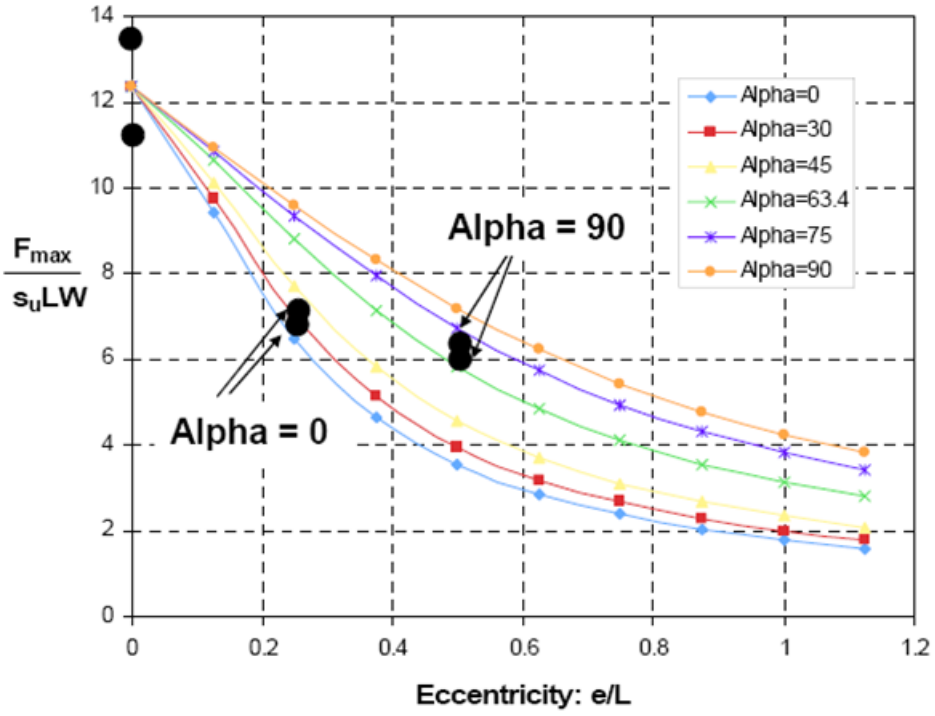

Fig. 3.25-B Comparisons of model predictions and experiment for rectangular plate

3.4 Torsion-Parallel Load Interaction

For a very thin plate, it is inevitable to have some loss of accuracy in finite element solutions since the refinement of the mesh cannot totally overcome the numerical problems caused by the end effects such as stress concentration and mesh locking. This loss does not have a large impact on the solutions for the normal load and rotational moments, as previously discussed, but significantly affects those for the parallel and torsional loads. Fortunately, a rather simple solution using the upper bound method can be utilized to analyze a thin plate subjected to the parallel and torsional loadings and hence the numerical problems are avoided.

3.4.1 Upper Bound Calculations

The rectangular (or square) plate considered herein is the same as the previous

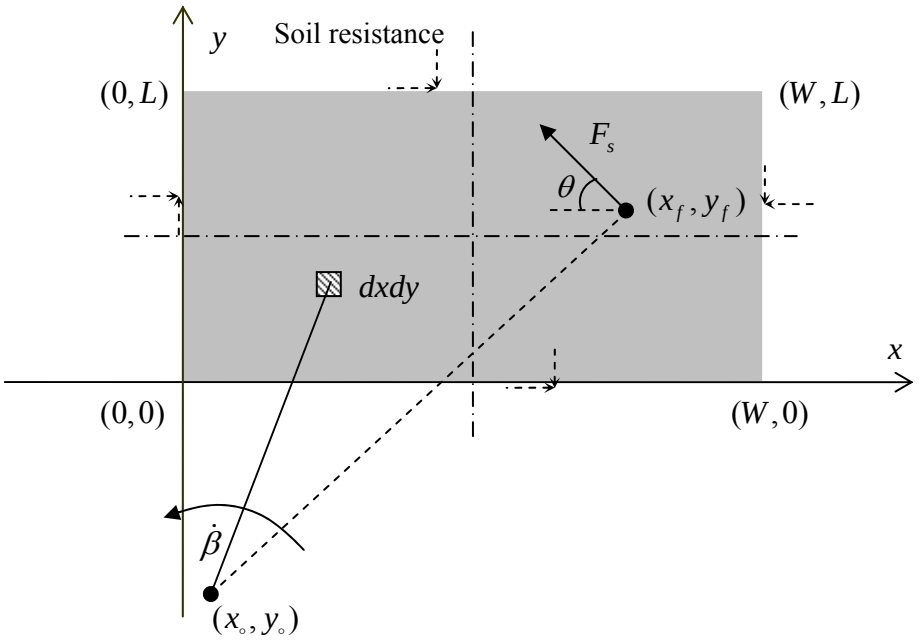

Fig. 3.26 Schematic for upper bound calculations

finite element model, i.e. the rigid plate is fully adhered to the soil around it. Fig. 3.26 shows the schematic of the plate geometry and loading condition. Assuming a virtual angular velocity of $\dot{\beta}$, the failure mechanism is simply a rigid rotation of the plate about a center of rotation with the coordinates of $(x_\circ, y_\circ)$. Therefore, the performance of a thin plate under parallel or torsional loading is actually a two-dimensional problem in the upper bound analyses. The rate at which the unknown external force, F_s, does work is given by

$$\dot{W} = F_s\left[\left(y_f - y_\circ\right)\cos\theta + \left(x_f - x_\circ\right)\sin\theta\right]\dot{\beta} \tag{3.14}$$

where symbols are defined in Fig. 3.26. The rate of internal dissipation of energy involves two parts: the dissipation, $\dot{D}_1$, caused by sliding along the top and bottom plate-soil interfaces, and the dissipation, $\dot{D}_2$, due to soil resistance against the plate ends. Here $\dot{D}_1$ is found by integrating the unit internal dissipation rate over the plate area as follows

$$\dot{D}_1 = 2\int_0^W \int_0^L s_u R(x,y)\dot{\beta}\,dx\,dy \tag{3.15}$$

where $R(x,y) = \sqrt{(x-x_\circ)^2 + (y-y_\circ)^2}$; s_u is the shear strength of soil-plate interface. The value of $\dot{D}_2$ depends on the thickness of the plate so it will vanish if the plate becomes infinitely thin. However, $\dot{D}_2$ will be included in the upper bound calculation to make the case more general. The soil resistance against the plate ends can be resolved into normal and sliding components, as shown in Fig. 3.26, both of which are assumed to be fully mobilized during failure. The unit dissipation rate is simply the virtual velocity times the shear strength for the sliding component but has to be multiplied by a bearing capacity

factor for the normal component. The bearing capacity factor, N_s, is empirically taken to be 7.5 for plane strain condition, and increases to some extent as the plate dimensions vary. $\dot{D}_2$ is given by integrating the unit dissipation rate over the length of the plate ends as follows

$$\dot{D}_2 = \int_0^L s_u \dot{\beta}\left[2N_s\left|y-y_\circ\right|+\left|x_\circ\right|+\left|W-x_\circ\right|\right]R_t L dy + \int_0^W s_u \dot{\beta}\left[2N_s\left(\left|x-x_\circ\right|\right)+\left|y_\circ\right|+\left|L-y_\circ\right|\right]R_t L dx \tag{3.16}$$

where R_t is the ratio of thickness to length of the plate. The upper bound method requires that we equate the rate of external work to the rate of internal dissipation of energy and solve for the unknown force, giving rise to

$$F_s = \frac{2\int_0^W \int_0^L s_u R(x,y)\dot{\beta}dxdy + \dot{D}_2}{\left[\left(y_f - y_\circ\right)\cos\theta + \left(x_f - x_\circ\right)\sin\theta\right]\dot{\beta}} \tag{3.17}$$

where the virtual angular velocity, $\dot{\beta}$, cancels. For a specific plate geometry, the best upper bound solution can be obtained by minimizing the value of F_s with respect to $x_\circ$ and $y_\circ$.

The force, F_s, offset from the plate geometric center is equivalent to the combination of the same force going through the center and a torque that is the force times the offset distance. Pure torsion is produced if the force, F_s, is applied at an infinite distance. Therefore, the overall interaction of the parallel and torsional loadings can be found by calculating the varying F_s as it moves from the plate geometric center to an infinite distance. To be consistent with the previous FE analyses, the thickness of the

plate is still assumed to be zero and hence $\dot{D}_2$ vanishes. Since we are only considering the sliding in the x-y plane now the proposed failure mode includes all possible mechanisms, and hence the optimum upper bound solutions are the exact solutions.

The capacity of an infinitely thin plate subjected to a pure torsional loading is found by the upper bound method in closed form, which gives rise to the non-dimensional factor as follows,

$$N_t = \frac{T_{\max}}{L^2 W s_u} = \frac{W^2}{6L^2}\left\{\frac{\sin\theta}{\cos^2\theta} + \ln\left[\tan\left(\frac{\pi}{4}+\frac{\theta}{2}\right)\right]\right\} + \frac{L}{6W}\left\{\frac{\cos\theta}{\sin^2\theta} - \ln\left[\tan\left(\frac{\theta}{2}\right)\right]\right\} \quad (3.18)$$

where $\theta = \tan^{-1}\left(L/W\right)$. The value of N_t depends only on the plate geometry. However, the parallel capacity factor is independent of the plate geometry, which is $N_s = \frac{F_{s\max}}{LWs_u} = 2$. As in the previous finite element analyses, a square plate and a rectangular one (ratio of width to length of 2:1) are considered here. For the square plate, $\theta = \pi/4$ and hence $N_t = 0.765$. For the rectangular plate with a 2:1 aspect ratio, $\theta = \tan^{-1}\left(0.5\right)$ and hence $N_t = 1.19$. Fig. 3.27 shows the interaction curves of parallel and torsional loads acting on the square plate and the rectangular, 2:1, plate. As expected, the loads significantly interact with each other since they act within the same plane when applied to a thin plate. The parallel capacities are very sensitive to the torsional load and greatly affected by even a small torsion value. For the square plate, the torsional capacity is not reduced significantly until the parallel load exceeds about 15% of its maximum value, whereas for the rectangular, 2:1, plate it is significantly reduced by the parallel load from the very beginning. The curve exhibits less convex shape as the plate geometry becomes more

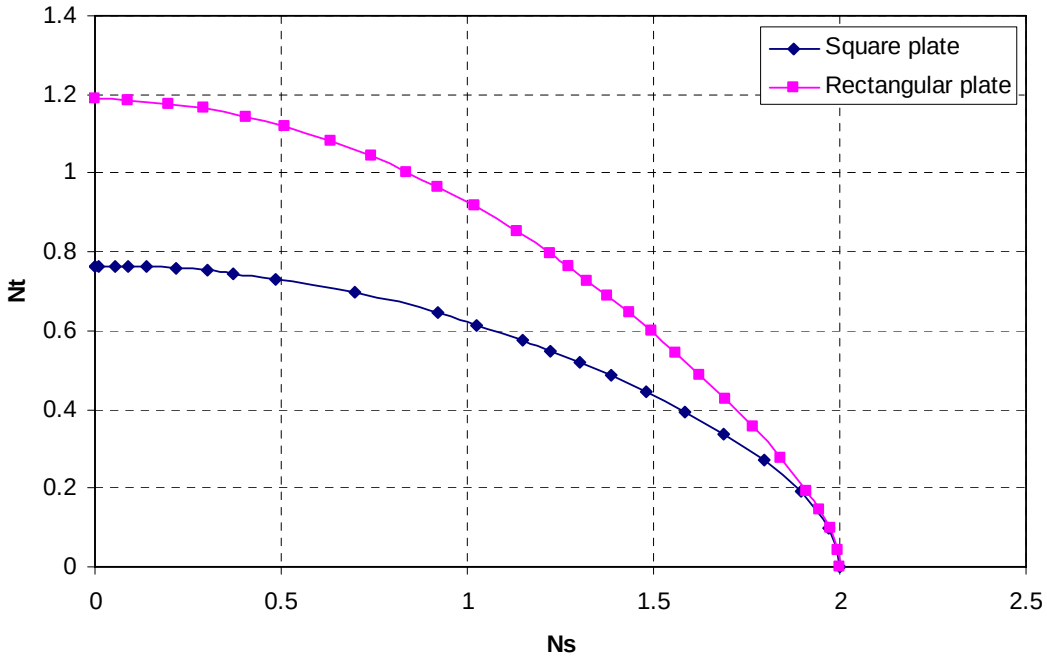

Fig. 3.27 Interaction curves of parallel and torsional loads for infinitely thin plates

rectangular, indicating a stronger interaction between the two loads.

Torsion effect on plate anchors is generally caused by an eccentric parallel load, and it systematically reduces the parallel load that can be sustained by the plate in sliding. For an infinitely thin plate, the anchor capacity under an eccentric parallel load only depends on the offset of the load from the geometric center. If y_f in Fig. 3.26 is taken to be zero the load offset becomes the value of x_f, and θ represents the load angle. Fig. 3.28-A and B show the torsion effects on the parallel resistance of a rectangular, 2:1, plate. For a given load angle, the anchor capacity is approximately linearly reduced with increasing load offset. A load angle of 0 degree is an end on loading and so the full parallel capacity can be mobilized independent of the load offset in the x direction.

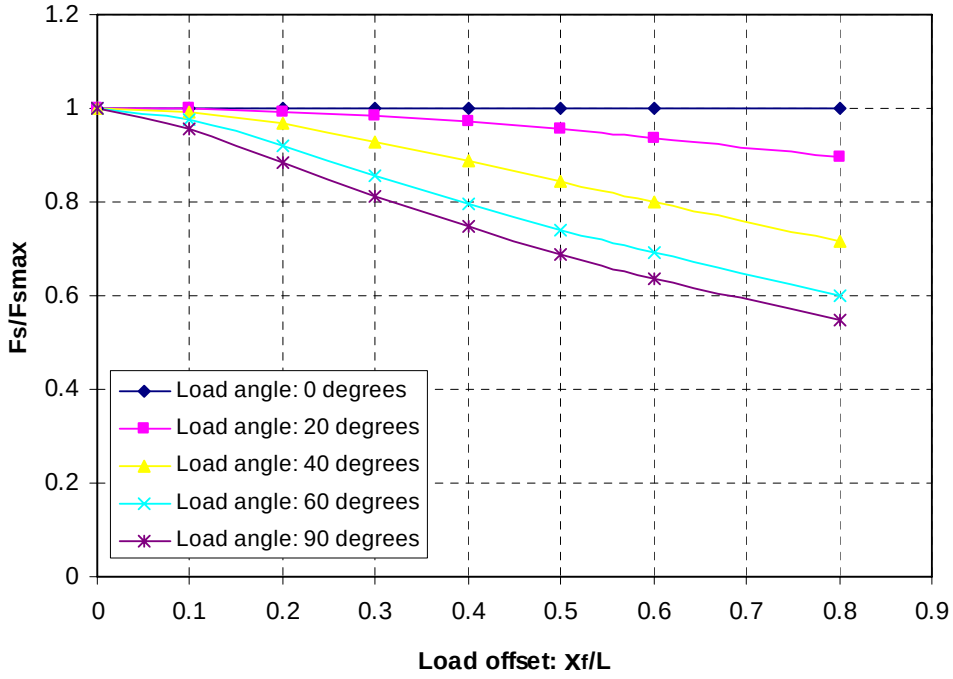

Fig. 3.28-A Parallel resistances of the rectangular plate vs. load offset (L/W=1:2)

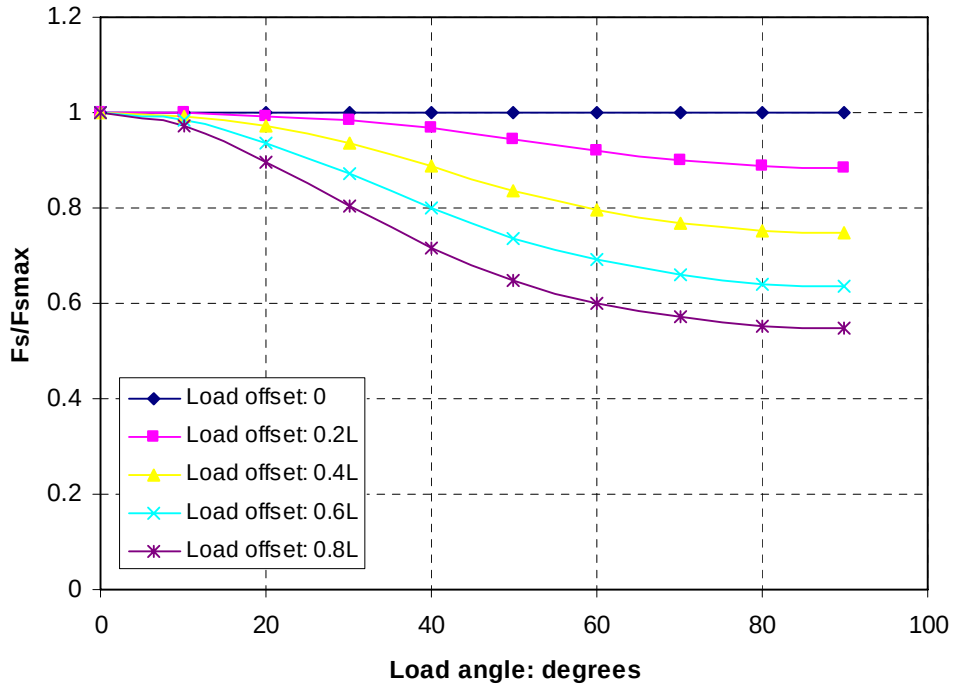

Fig. 3.28-B Parallel resistance of the rectangular plate vs. load angle (L/W=1:2)

3.4.2 Finite Element Verification of Upper Bound Solutions

The loss of accuracy due to end effects cannot be eliminated in finite element solutions simply by refining the mesh for a very (or infinitely) thin plate. For parallel or torsional loading, the finite element method basically overestimates the solutions by over 50%, even using a very dense mesh. To minimize the end effects in the finite element model, a buffer zone is set up around the plate ends in which the strength of soil is reduced, as shown in Fig. 3.29. This buffer zone is distributed symmetrically around the infinitely thin plate, and the cross section of the buffer zone is a square with the length of $L/20$. The other parameters such as plate dimensions, density of mesh, element type and model size etc. are maintained the same as the previous three-dimensional FE model that does not have a buffer zone. The finite element results obtained here are used to verify upper bound solutions for the interaction of parallel and torsional loadings, and the interaction will then be extended to include rotational moment.

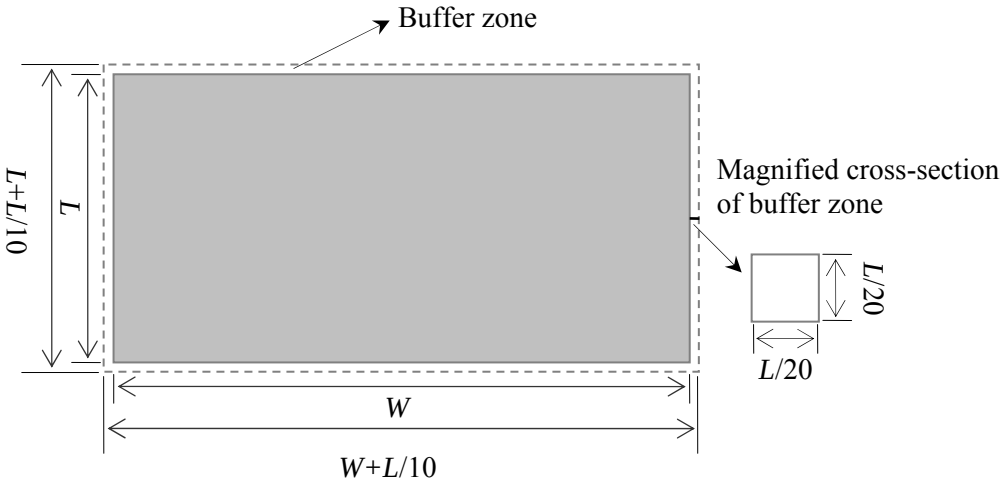

Fig. 3.29 Plate anchor with buffer zone

3.4.2.1 Square Plate Anchor

For the square plate, the strength of soil in the buffer zone was reduced by 50%. The FE results show that the buffer zone can decrease the end effects to some extent, but the anchor capacities are still overestimated. The pure parallel and torsional capacity factors are $N_s = 2.37$ and $N_t = 0.915$, which are 18.5% and 19.6% higher than the rigorous upper bound solutions of 2 and 0.765, respectively. The pure moment capacity factor is $N_m = 1.98$, which is 4.2% higher than the estimated upper bound solution of 1.9 but 10% lower than the FE solution of 2.2 without buffer zone. As discussed earlier, the normal capacity is not significantly affected by the end effects compared to other capacities, indicating that the strength of soil in the buffer zone should not be reduced too much. The pure normal capacity factor obtained here is $N_p = 12.41$, which is 6.6% lower than the FE solution of 13.28 without buffer zone, and only slightly lower than the estimated real solutions of 12.5 ~ 12.8. Therefore, the reduction of 50% in the strength of soil in the buffer zone is considered reasonable for the square plate.

Fig. 3.30 shows the FE results for the interaction of parallel and torsional loads and comparison with the upper bound solutions. By reducing the FE results the overestimated percentages, i.e. 18.5% for parallel load and 19.6% for torsional load, it is found that the interactions from two different methods exhibit excellent agreement although the absolute values are overestimated. Since the main aim of this study is to explore the overall interaction of loads acting on the plate when it fails, the relative values of the loads at failure are more important for our purposes than the absolute values.

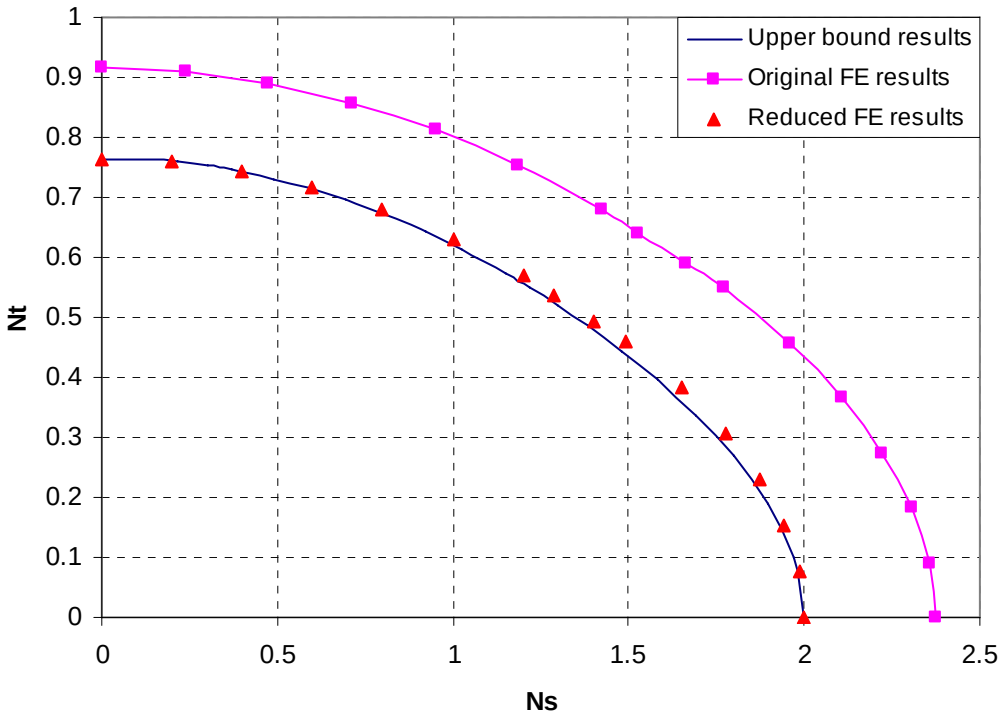

Fig. 3.30 Comparison of interactions of parallel and torsional loads by FE and upper bound method for square plate

Next we carry out finite element analysis to assess the interactions involving the torsion and rotational moments. These results are shown in Fig. 3.31. As indicated these moments do not interact significantly. The torsional capacity decreases only 1.3% and 4.5% when the rotational capacity is mobilized to 30% and 50% of its maximum value. Similarly, the rotational capacity decreases only 1.5% and 4.7% when the torsional capacity reaches 30% and 50% of its maximum value. Fig. 3.32 shows a very weak interaction between normal load and torsion, where the normal capacity and torsional capacity decrease only 3.4% and 3.1%, respectively, when the conjugate capacity

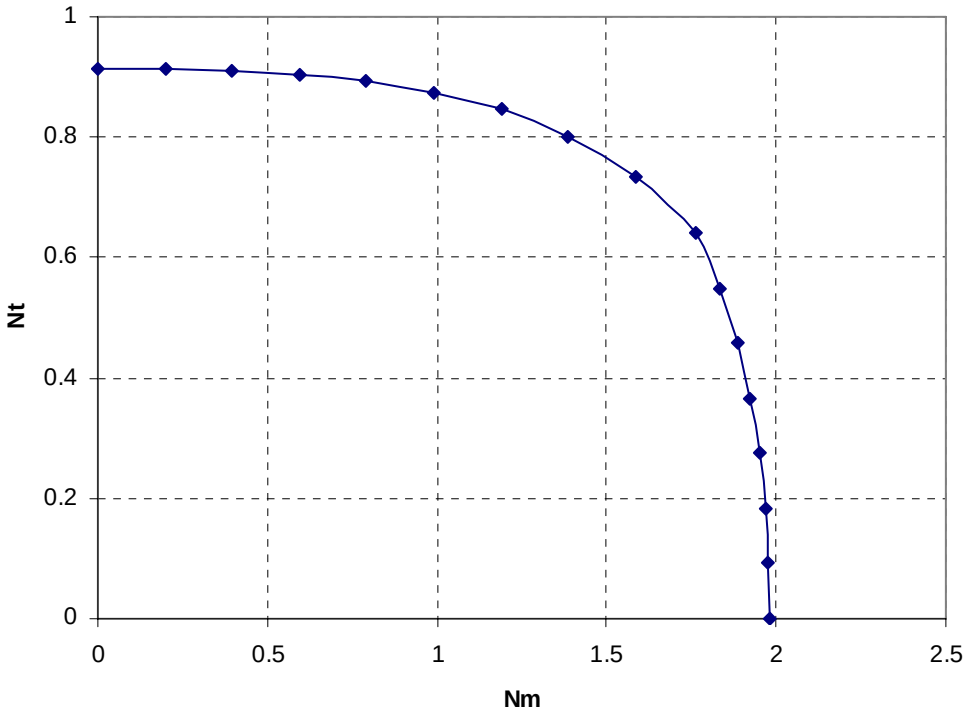

Fig. 3.31 Interaction of rotational moment and torque by FE for square plate

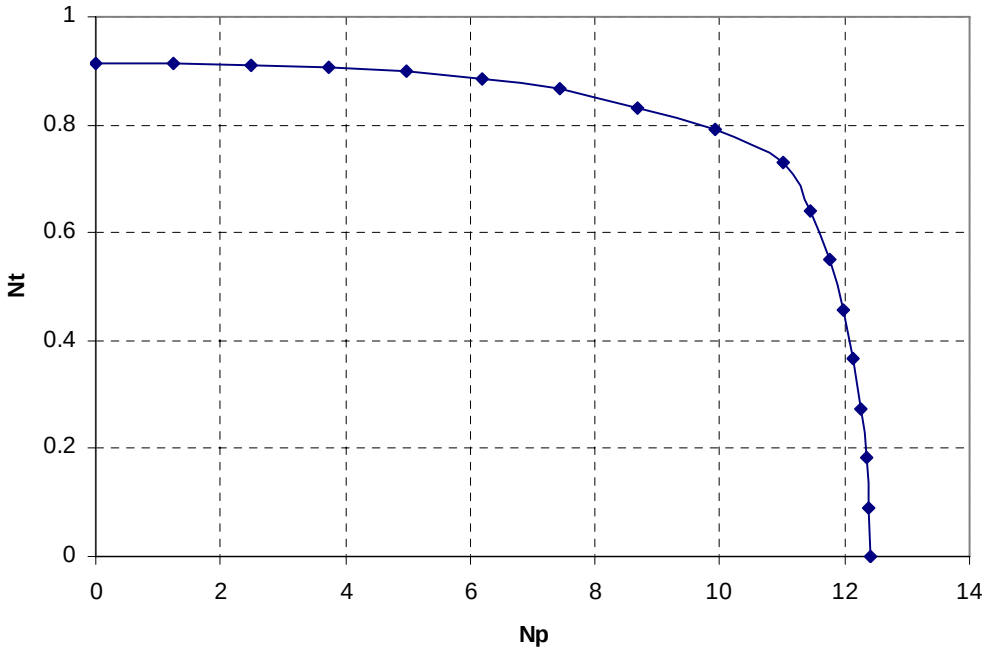

Fig. 3.32 Interaction of normal load and torque by FE for square plate

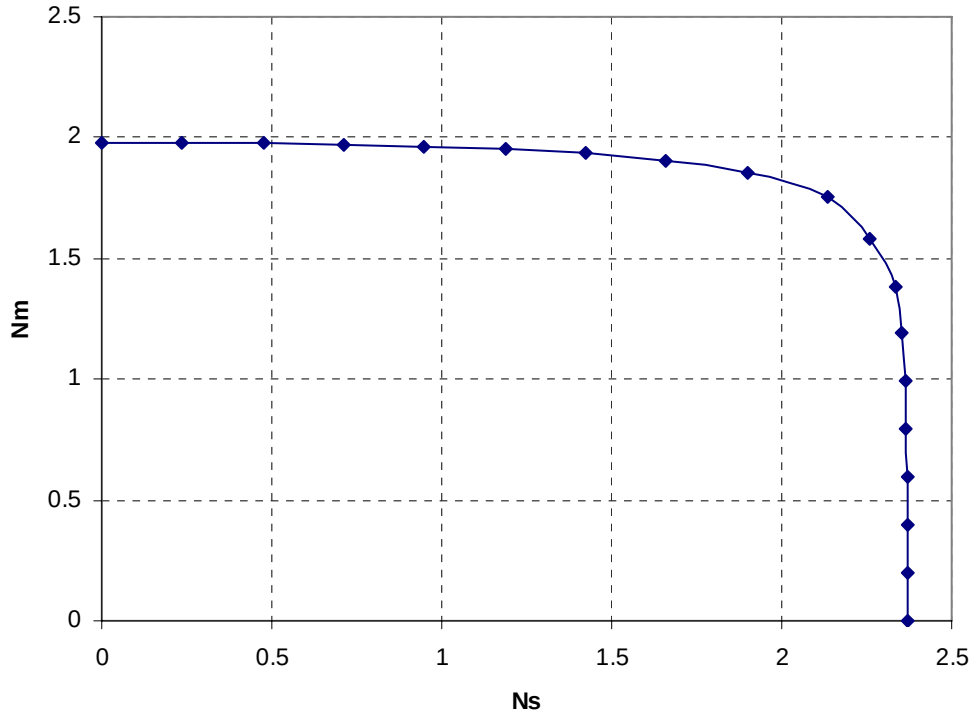

Fig. 3.33 Interaction of parallel load and rotational moment by FE for square plate

reaches 50% of its maximum value. Finally the interaction of parallel load and rotational moment is presented in Fig. 3.33 where the interaction curve approaches a rectangular shape. This indicates that there is little interaction between the parallel load and rotational moment such that it can be ignored.

3.4.2.2 Rectangular Plate Anchor

For the rectangular plate with a width to length ratio of 2:1, the strength of soil in the buffer zone was reduced by 70%. However, the FE results still overestimate the anchor capacities. The pure torsional and parallel capacity factors are $N_s = 2.52$ and $N_t = 1.49$, which are 26% and 25% higher than their rigorous upper bound solutions of 2

and 1.19. The pure normal capacity factor is $N_p = 12.63$, which is 2% higher than the estimated real solution of 12.35 and 3.7% lower than the FE solution of 13.12 without buffer zone. The pure rotational capacity factor about the short major axis is $N_{m1} = 2.3$, which is 7% higher than the estimated real solution of 2.15 but 8% lower than the FE solution of 2.5 without buffer zone. The pure rotational capacity factor about the long axis is $N_{m2} = 1.75$, which is 3% higher than the estimated real solution of 1.7 but 11% lower than the FE solution of 1.97 without buffer zone. Therefore, the reduction of 70% in the strength of soil in the buffer zone is considered reasonable for the rectangular, 2:1, plate.

Fig. 3.34 presents the FE results for the interaction of parallel and torsional loads and comparison with the upper bound solutions. As was done for the square plate, the FE results are reduced by the overestimated percentage, i.e. 26% for the parallel load and 25% for the torsional load, to be comparable with the upper bound solutions. As a result, the interactions indicate that the FE and upper bound methods are in good agreement, again verifying the upper bound mechanism for the parallel and torsional loadings. As found earlier, the rotational moment is caused by the eccentric normal load and does not interact significantly with the parallel load or torque. It is noted that the run-times for the analyses of the rectangular plate, especially for the interaction behavior, are increased greatly compared to the square plate and the previous FE model without the buffer zone for the rectangular plate. Therefore, the analyses are not conducted here for economy sake since it seems apparent what the interactions involving the rotational moments will reveal.

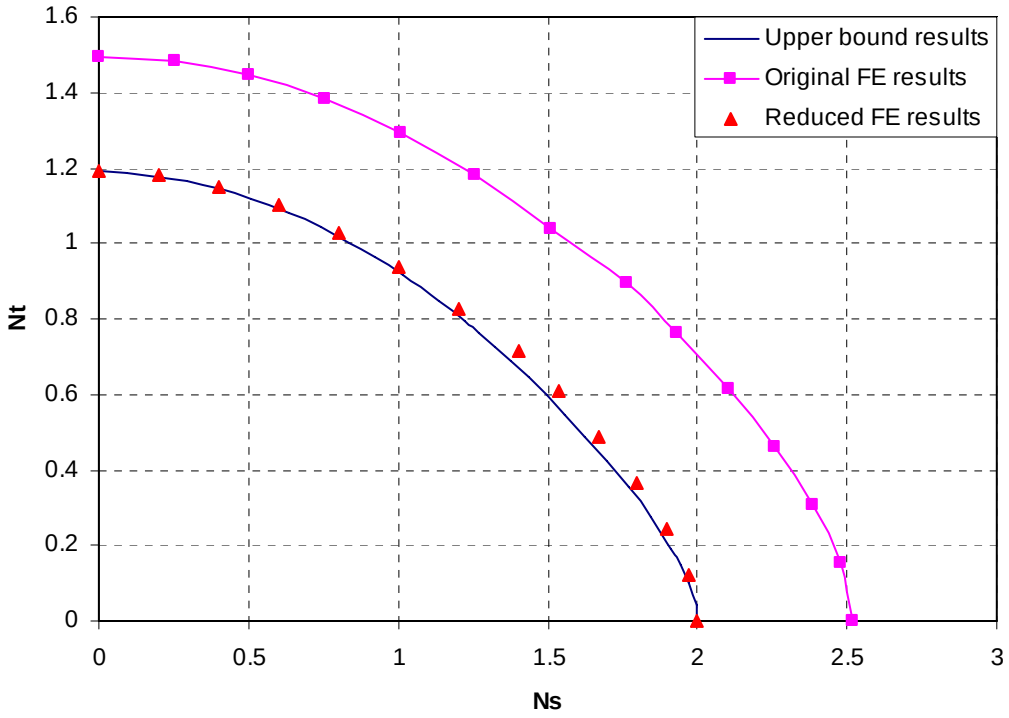

Fig. 3.34 Comparison of interactions of parallel and torsional loads by FE and upper bound method for rectangular, 2:1, plate

3.4.3 Extension of Interaction Model to Include Parallel and Torsional Loadings

The empirical interaction model presented earlier for the eccentric normal loading is now extended to include the parallel and torsional loadings. This model will be a mathematical function in F_n-F_s-M_1-M_2-T space, which fits the interaction curves obtained by both FE and upper bound analyses. For the infinitely thin square or rectangular plate, the following interaction model gives a good fit to the FE and upper bound results,

$$f = \left(\frac{F_n}{F_{n\max}}\right)^q + \left\{\left(\frac{M_1}{M_{1\max}}\right)^{m1} + \left(\frac{M_2}{M_{2\max}}\right)^{m2} + \left[\left(\frac{F_s}{F_{s\max}}\right)^n + \left(\frac{T}{T_{\max}}\right)^k\right]^s\right\}^{\frac{1}{p}} - 1 = 0 \quad (3.19)$$

where F_n, F_s, M_1, M_2 and T are the normal load, parallel load, moment and torque components of a combined loading at failure; $F_{n\max}$, $F_{s\max}$, $M_{1\max}$, $M_{2\max}$ and $T_{\max}$ are the ultimate values for pure normal, parallel, moment and torque loads where $M_{1\max} = M_{2\max}$ for the square plate. These ultimate values are determined by Eq. 3.3 for the square plate where $N_p = 12.5$, $N_s = 2$, $N_m = 1.9$ and $N_t = 0.765$, as well as by Eq. 3.9 for the rectangular, 2:1, plate where $N_p = 12.35$, $N_s = 2$, $N_{m1} = 2.15$, $N_{m1} = 1.7$ and $N_t = 1.19$. It is noted that the ultimate capacity for plate anchors with aspect ratios, width to length, between 1 and 2 can be estimated by a linear interpolation of known capacity. The exponents in Eq. 3.12 were obtained by a least squares fit and are tabulated in Table 3.6.

To check the effectiveness of Eq. 3.19, interactions predicted by Eq. 3.19 are compared with upper bound or FE results in Figs 3.35, 3.36, 3.37 and 3.38 where the FE results have been modified by reducing the overestimated percentages. The two sets of results are shown to be in reasonably good agreement. Therefore, the generalized interaction model described by Eq. 3.19 can be employed to determine the capacity of very thin square or rectangular, 2:1, plate subjected to any out-of-plane loading.

Table 3.6 Summary of Exponents in Various Interaction Models

Plate Types	m1	m2	n	p	q	k	s
Square	2.12	2.12	2.02	2.03	3.64	1.45	4.80
Rectangular	2.47	1.86	1.81	1.93	3.20	1.32	2.84
Plane Strain	1.56	-	4.19	1.57	4.43	-	-

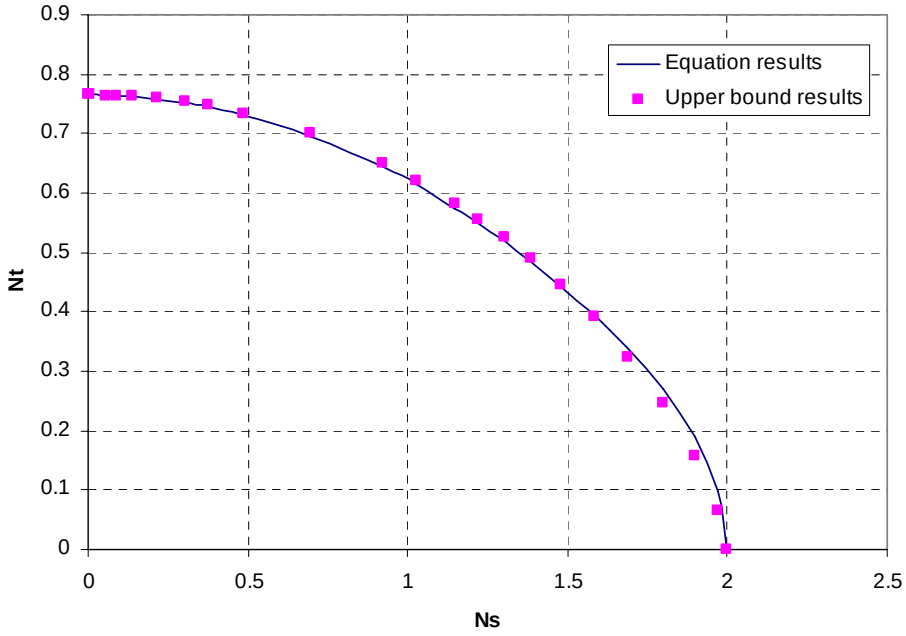

Fig. 3.35 Results comparison of upper bound and Eq. 3.19 for torsion and parallel load for square plate

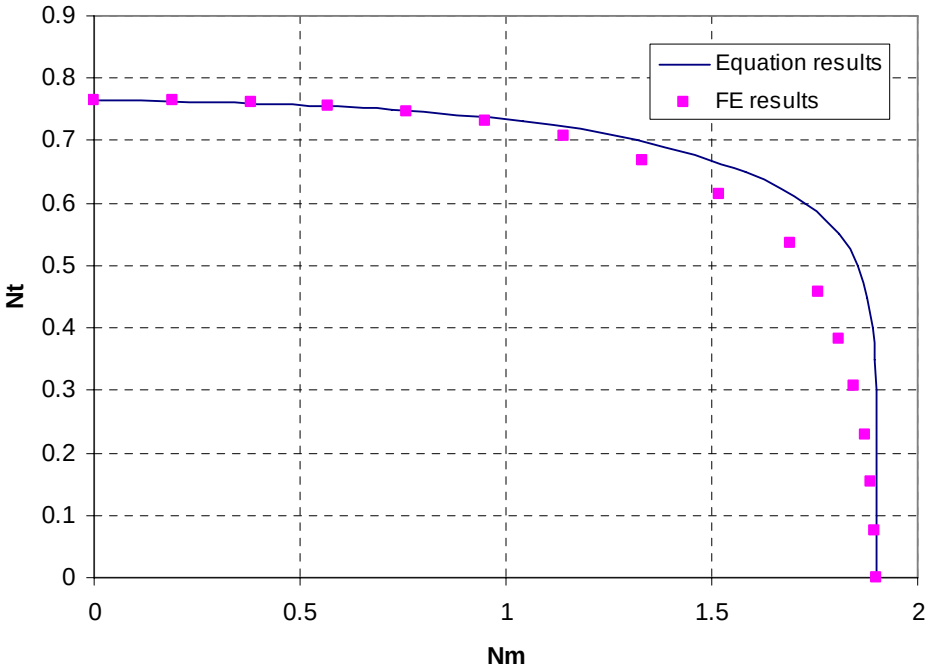

Fig. 3.36 Results comparison of modified FE and Eq. 3.19 for torsion and rotational moment for square plate

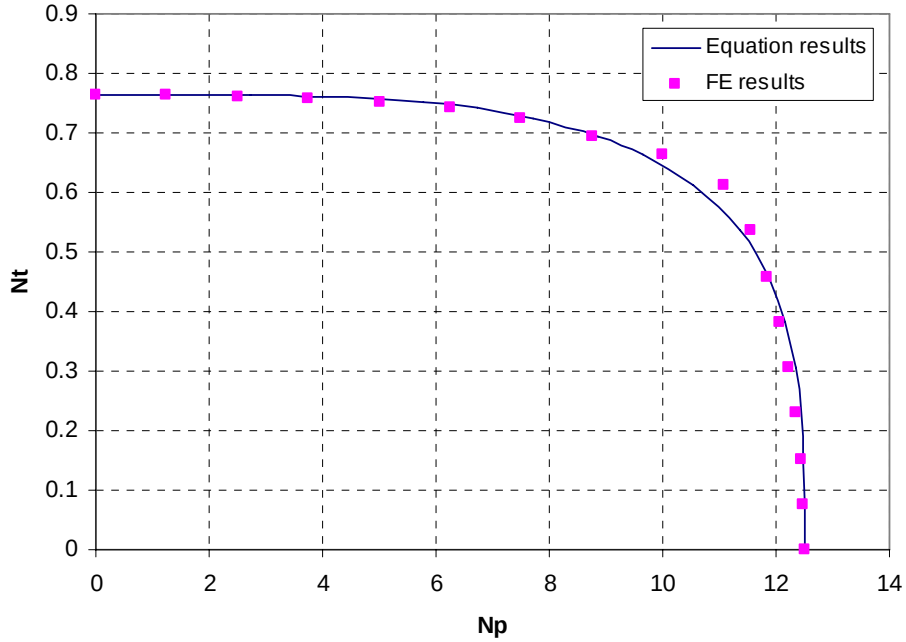

Fig. 3.37 Results comparison of modified FE and Eq. 3.19 for torsion and normal load for square plate

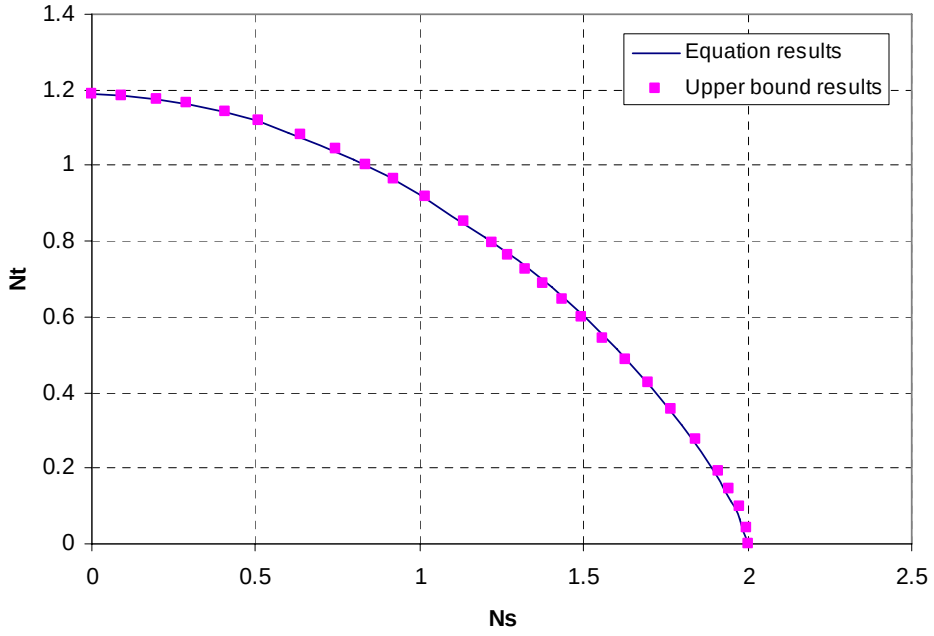

Fig. 3.38 Results comparison of upper bound and Eq. 3.19 for torsion and parallel load for rectangular plate with aspect ration of 2:1

3.5 Trajectory Prediction

3.5.1 Prediction Method

Prager (1959) showed that if a system of forces acts on an assemblage of plastic elements obeying the associated flow rule, causing the system to yield, the forces can be considered generalized stresses. The locus of forces causing yield (the interaction diagram) then constitutes a generalized yield surface. The ensuing plastic displacements can be treated as generalized strains and their directions are governed by the associated flow rule. It is necessary that the particular force and displacement variables selected are work conjugate pairs. For the case of an infinitely thin plate loaded with a general out-of-plane force, the generalized stresses and strains are selected as

Generalized stresses: F_n, F_s, M_1, M_2 and T

Generalized strains: n, s, θ_1, θ_2 and θ_3

where n and s are plastic normal and parallel displacements; θ_1 and θ_2 are the plastic rotations about two major axes; and θ_3 is the plastic torsion. Note that these variables are dimensionally consistent and meet the work conjugate requirement, i.e.

$$W = F_n \cdot n + F_s \cdot s + M_1 \cdot \theta_1 + M_2 \cdot \theta_2 + T \cdot \theta_3$$

where W is the plastic work. Also note that subscript n and s here are the normal and parallel displacements, not to be confused with the exponent n in the yield condition.

A thin square plate anchor was selected to demonstrate the trajectory prediction method and the interaction model expressed by Eq. 3.19 can be written as

$$f = \left(\frac{F_n}{F_{n\max}} \right)^q + \left\{ \frac{M_1^m + M_2^m}{M_{\max}^m} + \left[\left(\frac{F_s}{F_{s\max}} \right)^n + \left(\frac{T}{T_{\max}} \right)^k \right]^s \right\}^{\frac{1}{p}} - 1 = 0 \qquad (3.20)$$

where the loads and moments are defined as shown in Fig. 3.10 as

$$F_n = F\cos(\theta) \qquad (3.21)$$

$$F_s = F\sin(\theta) \qquad (3.22)$$

$$M_1 = e_1 \cdot F\cos(\theta) \qquad (3.23)$$

$$M_2 = e_2 \cdot F\cos(\theta) \qquad (3.24)$$

$$T = F\sin(\theta)\sin(\varphi)\sqrt{e_1^2 + e_2^2} \qquad (3.25)$$

The nonlinear Eq. 3.20 can be solved to determine the value of F for the orientation shown in Fig. 3.10 that will bring the soil-anchor system to yield. Knowing the capacity F, the plastic displacement (or rotation) increments can be calculated using the plastic stress-strain increment equation, which is

$$\dot{\delta}_i = \lambda \frac{\partial f}{\partial F_i} \qquad (3.26)$$

where $\dot{\delta}_i$ is the generalized strain increment; λ is a positive scale factor; F_i is the corresponding work conjugate generalized stress. That is, the direction of the anchor movement is governed by the normal to the plastic yield surface described by Eq. 3.20. Note that λ is not known but is the same for each strain component. This means that we cannot uniquely determine the magnitude of the strains but we can determine the relative values, i.e. the ratios of strains to each other. This can be done as follows

$$\frac{\dot{\delta}_s}{\dot{\delta}_n} = \frac{\partial f / \partial F_s}{\partial f / \partial F_n} \tag{3.27}$$

$$\frac{\dot{\theta}_1}{\dot{\delta}_n} = \frac{\partial f / \partial M_1}{\partial f / \partial F_n} \tag{3.28}$$

$$\frac{\dot{\theta}_2}{\dot{\delta}_n} = \frac{\partial f / \partial M_2}{\partial f / \partial F_n} \tag{3.29}$$

$$\frac{\dot{\theta}_3}{\dot{\delta}_n} = \frac{\partial f / \partial T}{\partial f / \partial F_n} \tag{3.30}$$

We can then assume a small strain increment for one component, say the displacement of the centroid normal to the plate and then calculate the values of all other strain components corresponding to the assumed component. The trajectory of the plate anchor can then be predicted by taking small increments of displacement, updating the loads and moments at failure based on the new anchor orientation, and solving for the next set of strain increments. This can be continued in a step by step fashion.

In fact, the parallel and torsional capacity will depend on the plate thickness but as we have shown, the moment and normal capacity are less sensitive to the parallel load and torsion. Therefore, qualitative predictions for trajectories of plate anchors with thickness should be made by reasonably adjusting the ultimate values of capacity factors, N_s and N_t.

3.5.2 Example Predictions

To illustrate the capacity/trajectory prediction method, a simple example is detailed here. The idealized plate anchor is an infinitely thin square plate, one foot on a side. The soil is normally consolidated clay with a mudline strength of 20 psf and a strength gradient of 8 psf/ft, typical of deepwater sites. The anchor is embedded 10 feet below the mudline and loaded vertically at various eccentricities.

Fig. 3.39 demonstrates the general behavior of the predicted trajectory of the anchor when loaded with a one way eccentricity of 0.25 feet (halfway between the centroid and edge with the offset in one direction only, i.e. $\alpha = 0$ degrees). The solid line is the trajectory of the anchor centroid as it is pulled upward. The thin rectangles represent the anchor plate and show the anchor orientation at various elevations above the initial position. Note that the horizontal scale is exaggerated for the trajectory plot. However, the orientations of the plate are shown at the actual predicted angles. For example, when the anchor centroid has moved upward 2.5 feet (at a depth of 7.5 feet), the anchor has already rotated approximately 45 degrees. At 4.47 feet depth it is predicted that the anchor has rotated 56 degrees.

There are several things to note about the predicted behavior. Initially there is no load parallel to the anchor but as the anchor rotates the vertical load quickly develops a load component parallel to the plate. The parallel resistance is generally weaker than the normal or moment resistance so the anchor tends to move horizontally or “skate”. As the rotation continues the eccentrically loaded anchor tends to align itself parallel to the load. This reduces the horizontal movement and eventually the anchor tends to pull

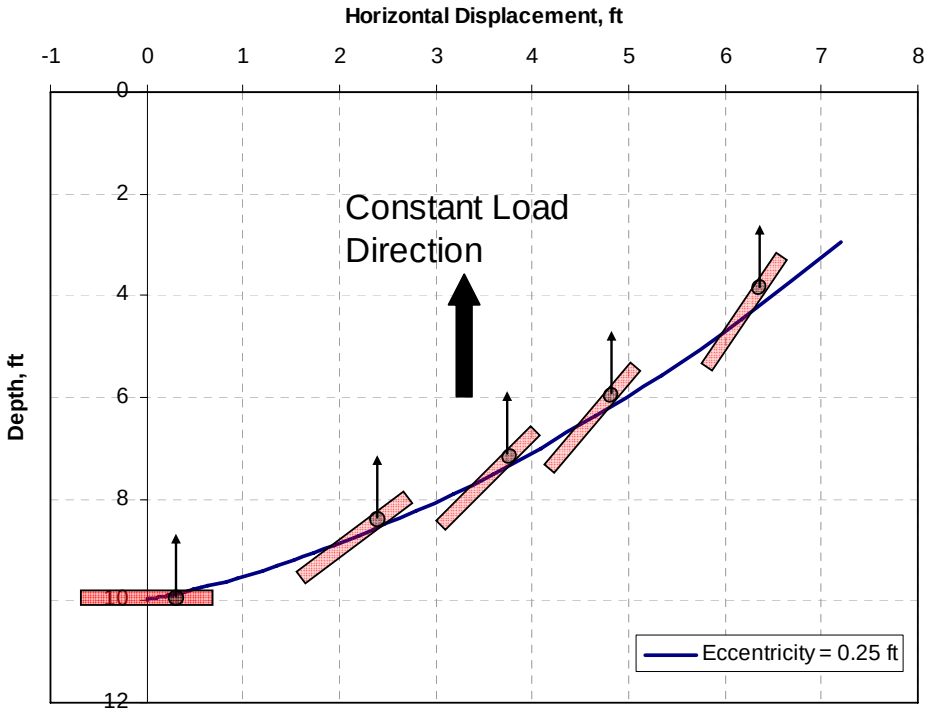

Fig. 3.39 Anchor trajectory and orientation for a square plate loaded at eccentricity of 0.25 ft

out nearly parallel to the plate. This of course is strongly affected by the assumed load direction.

For more pronounced eccentricities the plate is predicted to rotate faster and hence will not skate as far. Conversely for the small eccentricities the plate rotates more slowly and therefore tends to move horizontally to a greater degree. This behavior is shown in Fig. 3.40 which shows the predicted trajectory for square plate anchors with varying eccentricities. Of course for the ideal case of centric loading the anchor will theoretically not rotate and will move directly upward. This suggests that the anchor trajectory may become unstable under centric loading, since the anchor will never be

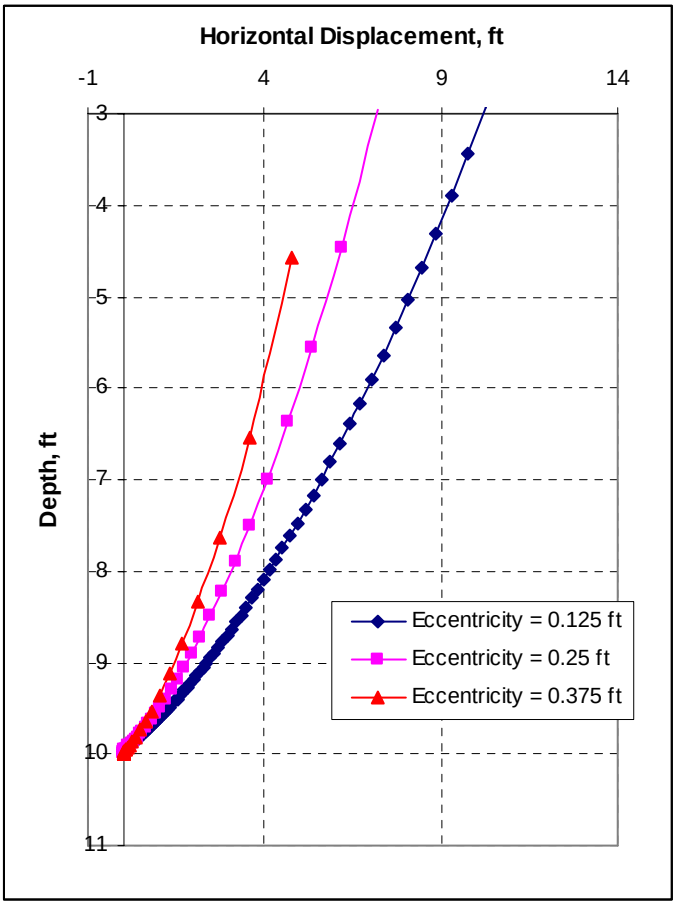

Fig. 3.40 Trajectory predictions for 1.0 ft^2 square plate anchor, embedded 10 feet BML, at varying eccentricities during pull-out

exactly centrically loaded. The sensitivity of this prediction can be strongly influenced by the parallel resistance of the plate and the exponents in the prediction equation. This is an area that needs further investigation, both analytically and experimentally.

Finally it should be emphasized that the foregoing is a preliminary model presented here to demonstrate the potential of the method. Considerable work needs to be carried out on various aspects of the prediction including anchor line behavior and

refinement of the anchor model to include all six rigid body degrees of freedom (three rotations and three translations).

Fig. 3.41 shows the resistance to anchor pull-out for the cases shown in Fig. 3.40 with the addition of the centrically loaded plate. For the centrically loaded plate the reduced resistance is due strictly to the decreasing soil strength as the anchor is pulled upward. For the eccentrically loaded anchors the reduced resistance is due to the reduced soil strength and the eccentric load effect as illustrated in Fig. 3.18. Note that the prediction of anchor skating does not reduce the anchor resistance. It is also important to emphasize that in the cases shown in Figs 3.40 and 3.41 the load was assumed to be maintained vertically upward. In the real case the pulling angle will probably change as the anchor moves laterally and rotates and the anchor line cuts through the soil. This suggests a further study to develop the ability to predict the 3D anchor line behavior and to couple it with the anchor response as the anchor line cuts through the soil at varying pull orientations during vessel drift. The performance of the anchor line will be studied in the following chapter.

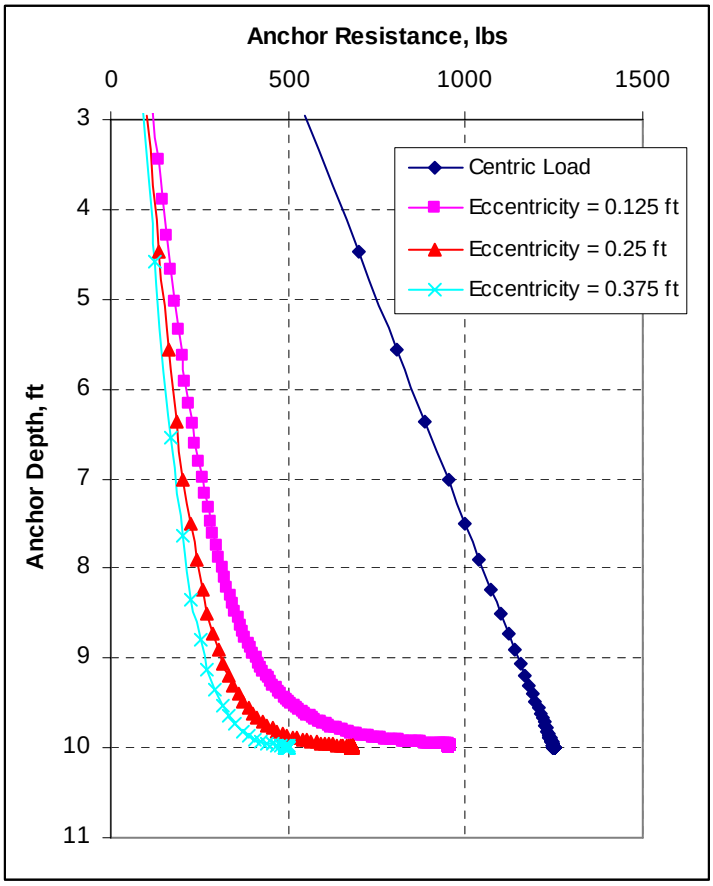

Fig. 3.41 Resistance predictions for 1.0 ft^2 square plate anchor, embedded 10 feet BML, at varying eccentricities during pull-out

CHAPTER IV

PERFORMANCE OF SUCTION EMBEDDED PLATE ANCHORS

4.1 Theoretical Model for Suction Embedded Plate Anchors (SEPLAs)

As previously described, the SEPLAs are easier to be penetrated to the target depth at a specific location compared to other types of plate anchors (DEAs and VLAs). Meanwhile, the "keying" process gives rise to the loss of embedment depth of the SEPLAs to some extent, as shown in Fig. 4.1, and hence the anchor capacity is reduced in normal offshore soil that has increasing strength with depth. The proposed model

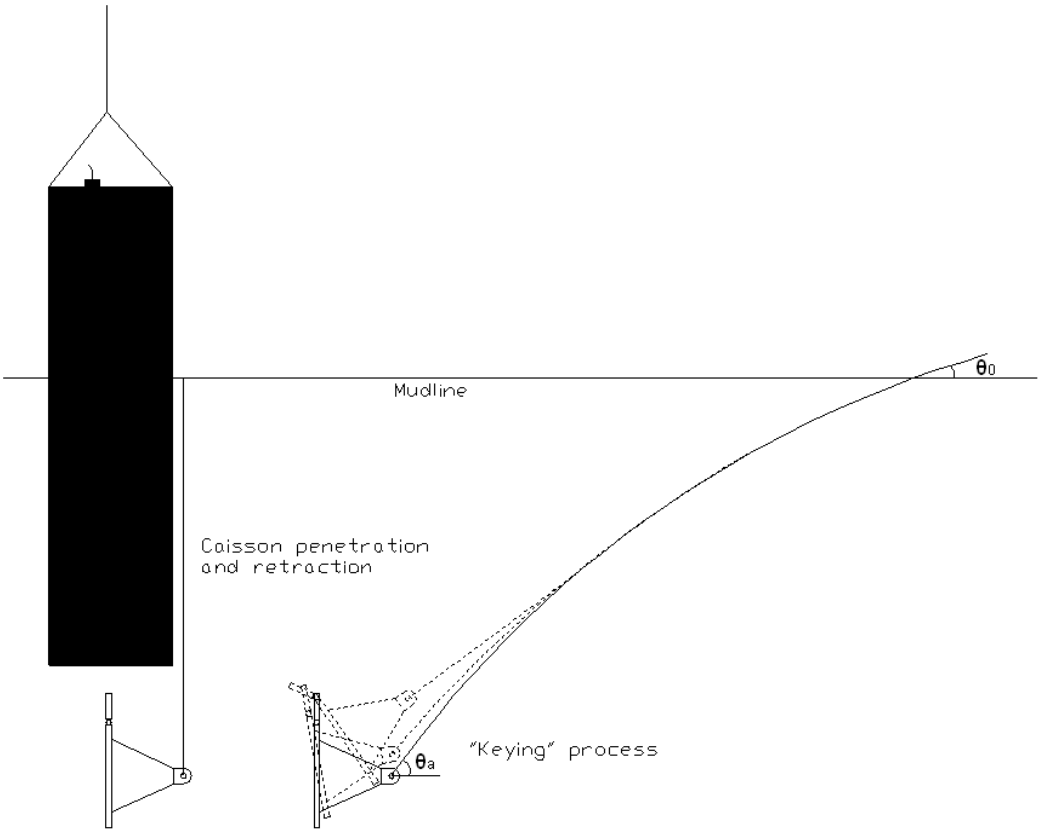

Fig 4.1 Schematic of SEPLA installation

aims at predicting the trajectory of the SEPLAs during the “keying” process and the ultimate anchor capacity after the “keying” is complete.

4.1.1 Plate Anchor Capacity

As was given in Chapter III, the normalized ultimate capacities of a wide, thin plate anchor under in-plane pure loadings can be characterized by the following relationships proposed by O’Neill et al. (2003).

$$N_p = \frac{F_{n\max}}{Ls_u} = 3\pi + 2 + 2\frac{t}{L}\left(\alpha + \frac{1+\alpha}{\sqrt{2}}\right) \tag{4.1}$$

$$N_s = \frac{F_{s\max}}{Ls_u} = 2\left[\alpha + N_{tip}\frac{t}{L}\right] \approx 2\alpha + 15\frac{t}{L} \tag{4.2}$$

$$N_m = \frac{M_{\max}}{L^2 s_u} = \frac{\pi}{2}\left[1 + \left(\frac{t}{L}\right)^2\right] \tag{4.3}$$

where L and t are the length and thickness of the plate anchor (in the intended plane of loading), respectively; $F_{n\max}$, $F_{s\max}$ and $M_{\max}$ are the normal , parallel and rotational capacities per unit width (normal to the intended plane of loading), respectively; and α is the coefficient of anchor surface roughness. This solution is strictly valid for plane strain condition, and gives a rough estimate for a finite width plate by simply multiplying the unit width capacity by its actual width.

An offset form of the Murff (1994) equation was developed by O’Neill et al. (2003) for describing the yield behavior of the plate anchor under a combined loading.

$$f = \left(\frac{F_n}{F_{n\max}}\right)^q + \left[\left(\frac{M}{M_{\max}}\right)^m + \left(\frac{F_s}{F_{s\max}}\right)^n\right]^{\frac{1}{p}} - 1 = 0 \tag{4.4}$$

where F_n, F_s, and M are normal load, parallel load and moment components of a combined loading at failure, which will be detailed for SEPLA anchors in a subsequent section; and $F_{n\max}, F_{s\max}$, and $M_{\max}$ are the maximum values for pure normal load, shear load and moment (i.e. without interaction) determined using Eqs 4.1, 4.2 and 4.3. The values of exponents m, n, p and q are obtained by a least squares fit of finite element solutions to the equation for multi-axial loading. The values tabulated in Table 4.1 is for the case where the soil is fully attached, i.e. $\alpha = 1$, to the plate surface (Anderson et al., 2003).

Table 4.1 Values of Exponents in Eq. 4.4

Exponent	m	n	p	q
Values	1.37	3.74	1.22	3.68

4.1.2 Anchor Chain Interaction

The uplift load imposed by the offshore floating structure acts at the padeye of the plate anchor through the anchor chain. The profile of anchor chain is a standard catenary above the seabed and then transformed into a reverse catenary-like shape within the soil as shown schematically in Fig.4.1. The portion of the anchor chain embedded in soil is considered in this study. The behavior of the embedded anchor chain is very important for the entire anchor-chain system. One feather of the system is the frictional resistance of the anchor chain, which can be a significant contributor to the overall anchor capacity (Degenkamp and Dutta, 1989). The other feature is the chain inclination, represented as an angle from the horizontal, at the padeye of the anchor. This angle

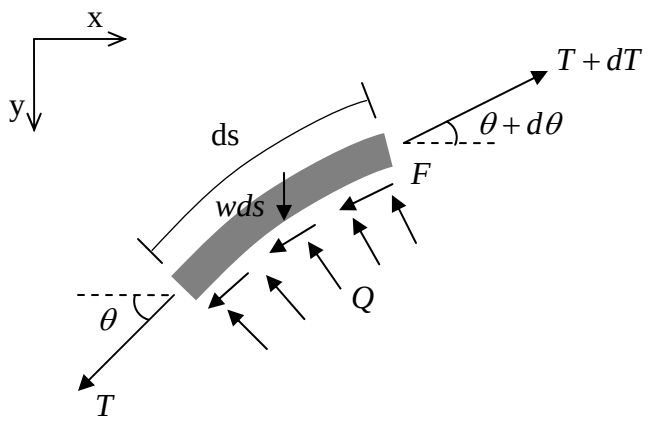

Fig. 4.2 Schematic of anchor chain force

determines the relative magnitudes of normal load, parallel load and moment components of a loading applied at the anchor, which in turn determines the failure mode of the anchor. The force equilibrium of the embedded chain element is schematically shown in Fig. 4.2. Vivatrat et al. (1982) presented two ordinary, coupled differential equations for describing the interaction of chain and soil, allowing for the chain-soil frictional resistance and the chain weight, which are

$$\frac{dT}{ds} = F + w\sin\theta \tag{4.5}$$

$$T\frac{d\theta}{ds} = -Q + w\cos\theta \tag{4.6}$$

where T is the chain tension; F is the chain friction per unit length; w is the chain weight per unit length; θ is the chain angle from the horizontal; and Q is the normal soil resistance per unit length. F and Q are related by a "quasi" frictional coefficient μ between the chain and the soil as following

$$F = \mu Q \tag{4.7}$$

Eqs 4.5 and 4.6 can be numerically solved with an iterative scheme as proposed by Vivatrat et al. (1982).

Neubecker and Randolph (1995) linearized Eqs 4.5 and 4.6 and derived an approximate closed-form expression that relates the tension and inclination of the chain at a given padeye depth to the tension and inclination at the mudline. This solution is summarized as

$$T_o = T_a e^{\mu(\theta_a - \theta_o)} \tag{4.8}$$

where T_o is the chain tension at the mudline; T_a is the chain tension at the padeye; θ_a is the chain angle at the padeye; and θ_o is the chain angle at the mudline.

By including the profile of soil strength between the mudline and the padeye, Eq. 4.8 can also be written in the form (Neubecker and Randolph, 1995):

$$\frac{T_a}{1+\mu^2}\left[e^{\mu(\theta_a-\theta_o)}\left(\cos\theta_o + \mu\sin\theta_o\right) - \cos\theta_a - \mu\sin\theta_a\right] = E_n d N_c \int_0^D s_u(z)dz \tag{4.9}$$

where E_n is the multiplier giving the effective chain width in the normal direction; *d* is the nominal chain stock diameter; N_c is the normal bearing capacity factor for the chain; $s_u(z)$ is the soil strength at the depth *z*; and *D* is the depth of the padeye.

The recommended value of E_n is 2.5 for the chain with a link length of 5 or 6 times the stock diameter (Degenkamp and Dutta, 1989). The value of N_c is taken to be 7.5 compared to the end of a strip plate anchor. The chain weight is ignored in Eqs 4.8 and 4.9, but can be accounted for by reducing the profile of normal resistance per unit

length by an amount equal to the chain weight per unit length. Actually, the effect of chain weight on the profile and tension distribution of the chain is essentially negligible except at shallow depths in very soft soil where the chain itself can cut into soft soil to some extent under its self-weight alone (Neubecker and Randolph, 1995).

4.1.3 Generalized Plastic Limit Analysis

The concept of the generalized plastic limit analysis presented by Prager (1959) was summarized in Chapter III. For a strip plate anchor subjected to an inclined load offset from the plate geometric centroid, the generalized stresses are selected as the load components F_n, F_s and M; and the generalized strains are selected as *n*, *s* and θ, where *n*, *s* are plastic normal and parallel displacements and θ is the plastic rotation about the plate centroid. Note that these variables are dimensionally consistent and meet the work conjugate requirement, i.e.

$$W = F_n \cdot n + F_s \cdot s + M \cdot \theta \tag{4.10}$$

where *W* is the plastic work. Also note that the subscript *n* here is the normal displacement, not to be confused with the exponent *n* in the yield condition.

As previously described, the nonlinear Eq. 4.4 is employed as the yield function for the plate anchor. Taking the derivatives of Eq. 4.4 with respect to load components gives the plastic stress-strain increment equations to calculate the plastic displacement (or rotation) increments, as described by the associated flow rule, which is

$$\dot{\delta}_i = \lambda \frac{\partial f}{\partial F_i} \tag{4.11}$$

where $\dot{\delta}_i$ is the generalized strain increment (displacement or rotation increment); λ is a

positive scale factor; F_i is the corresponding work conjugate generalized stress (load component). That is, the direction of the anchor movement is governed by the normal to the plastic yield surface described by Eq. 4.4. Substituting Eq. 4.4 into Eq. 4.11 gives the strain (displacement or rotation) increments in the detailed forms

$$dn = \lambda \frac{\partial f}{\partial F_n} = \lambda\, q \left(\frac{F_n}{F_{n\max}} \right)^{q-1} \left(\frac{1}{F_{n\max}} \right) \tag{4.12}$$

$$d\theta = \lambda \frac{\partial f}{\partial M} = \frac{\lambda}{p} \left(\left(\frac{M}{M_{\max}} \right)^{m} + \left(\frac{F_s}{F_{s\max}} \right)^{n} \right)^{(\frac{1}{p}-1)} \left(m \left(\frac{M}{M_{\max}} \right)^{m-1} \left(\frac{1}{M_{\max}} \right) \right) \tag{4.13}$$

$$ds = \lambda \frac{\partial f}{\partial F_s} = \frac{\lambda}{p} \left(\left(\frac{M}{M_{\max}} \right)^{m} + \left(\frac{F_s}{F_{s\max}} \right)^{n} \right)^{(\frac{1}{p}-1)} \left(n \left(\frac{F_s}{F_{s\max}} \right)^{n-1} \left(\frac{1}{F_{s\max}} \right) \right) \tag{4.14}$$

Note that λ is not known but is the same for each strain component. This means that we cannot uniquely determine the magnitude of the strains but we can determine the relative values, i.e. the ratios of strains to each other, which are written as follows

$$\frac{ds}{dn} = \frac{\partial f / \partial F_s}{\partial f / \partial F_n} \tag{4.15}$$

$$\frac{d\theta}{dn} = \frac{\partial f / \partial M}{\partial f / \partial F_n} \tag{4.16}$$

As was done in Chapter III, given a specific yield load calculated using Eq. 4.4, a small strain increment is assumed for one component, say the displacement of the centroid normal to the plate and then calculate the values of all other strain components corresponding to the assumed component. The trajectory of the plate anchor can then be predicted by taking small increments of displacement, updating the load components at

failure based on the new anchor and anchor line orientations, and solving for the next set of strain increments. This can be continued in a step by step fashion.

4.1.4 Suction Embedded Plate Anchor (SEPLA)

As was previously done for a regular plate, the SEPLA is modeled subjected to a combined load with normal load, parallel load and moment components referenced to the centroid of the fluke. Fig. 4.3 shows that the SEPLA anchor consists of a fluke, a shank attached to the fluke and a hinged "keying" flap. The shank offsets the padeye in front of the fluke such that the anchor rotates or "key" under the parallel component of the load acting at the padeye by the anchor line. The normal component goes through the centroid of the fluke and hence makes no rotation. To offset the normal component, however, a flap is added to the top of the fluke such that the center of rotation is varied. In the configuration of the SEPLA, the flap is free to rotate back and forth within a backward "stop" angle, generally about 30^o, from the fluke but strictly restricted from rotating forward from the fluke as shown in Fig. 4.3.

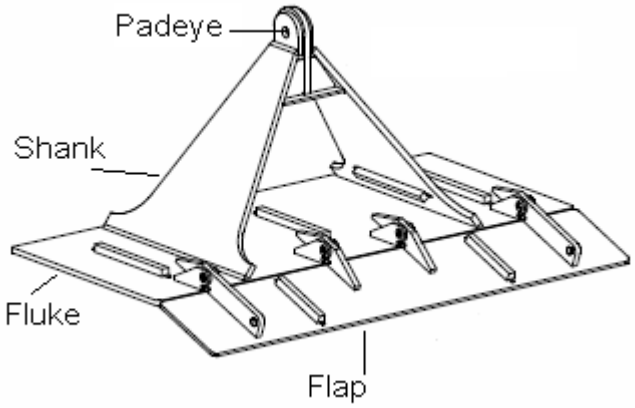

Fig. 4.3 Configuration of SEPLA

The fluke and flap are both maintained in a vertical orientation at the beginning of the "keying" process, as shown in Fig. 4.1. Once the SEPLA starts to "key", the top side of the fluke first moves backward and in turn makes the flap rotate together with the fluke as a rigid extension. Apparently, the SEPLA at this point can be approximated as a single, extended regular plate anchor with the length of the extended fluke equal to the length of the original fluke, L_1, plus the length of the flap, L_2. This means that the SEPLA rotates about the centroid of the extended fluke instead of the original one. That is to say, the center of rotation of the SEPLA is moved up by the rigid flap and hence the normal component of the load becomes eccentric. The flap was assumed to help the "keying" of the anchor in the conventional SEPLA design. However, the flap, unlike the shank, also develops a significant soil resistance in the opposite direction which tends to delay the "keying" of the SEPLA in the mean time. Therefore, it is too early to draw a conclusion regarding the net effect of the flap during various stages of the "keying" process of the SEPLA without any theoretical or experimental verification. The function of the flap will be tested by the proposed theoretical model in this study.

Fig. 4.4 shows that the top of the fluke begins to move forward as the SEPLA rotates to such an extent that the anchor line is approximately perpendicular to the fluke. However, the flap does not rotate backward from the fluke until the following condition is satisfied

$$\frac{dn'}{dn} > \frac{L_2}{L_2 + L_1/2} \tag{4.17}$$

where dn' is the normal displacement for the top of the fluke; and dn is the normal

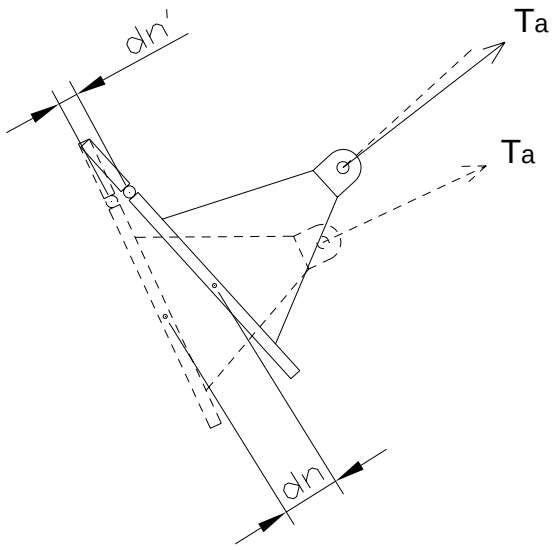

Fig. 4.4 Critical condition for the flap rotating backward relative to the fluke

displacement for the centroid of the fluke. Note that dn' and dn are approximately equal to the total displacements of the top and the centroid of the fluke as the rotation of the SEPLA is very small. Once Eq. 4.17 is satisfied the extended fluke becomes “broken” at the hinge, i.e. the flap rotates backward from the fluke. The flap acts pinned to the fluke when it is free to rotate within the “stop” angle, and thus it behaves as an independent plate subjected to an inclined load applied at the bottom edge by the fluke. Consequently, the fluke and flap can both be modeled as individual plate anchors, to which Eq. 4.4 can be applied, with the same displacement at the hinge.

Fig. 4.5 shows the force equilibrium of the SEPLA where the flap is free to rotate. The fluke is not only subjected to an active load, T_a, at the padeye from the anchor line but also a reacting load, T_f, at the top edge from the flap as well as some additional resistance, T_s, from the shank. These loads can be resolved into the normal,

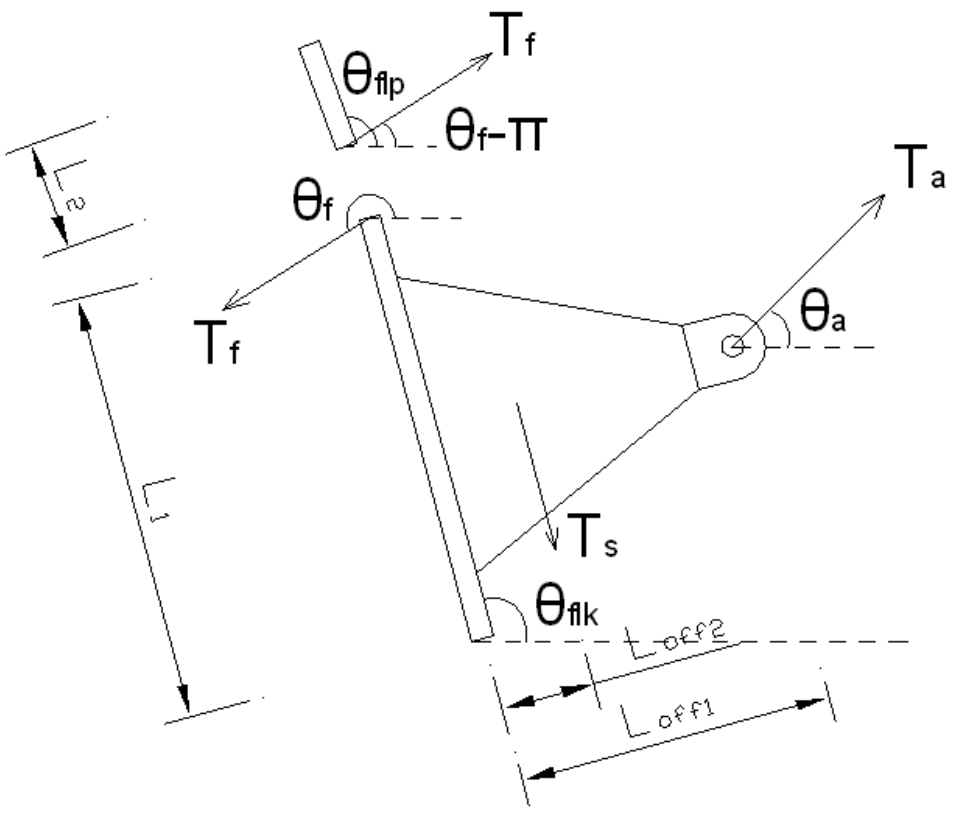

Fig. 4.5 Schematic of force equilibrium of the SEPLA

parallel and moment components referenced to the fluke centroid. For the load acting at the fluke imposed by the anchor chain, the components are expressed as follows

$$F_{na} = T_a \sin(\theta_{flk} - \theta_a) \tag{4.18}$$

$$F_{sa} = T_a \cos(\theta_{flk} - \theta_a) \tag{4.19}$$

$$M_a = F_{sa} L_{off\,1} \tag{4.20}$$

For the load acting at the fluke imposed by the flap, the components are given as follows

$$F_{nf} = T_f \sin(\theta_{flk} - \theta_f) \tag{4.21}$$

$$F_{sf} = T_f \cos(\theta_{flk} - \theta_f) \tag{4.22}$$

$$M_f = -F_{nf} L_1/2 \tag{4.23}$$

The resistance caused by the shank includes two parts: side friction and end bearing. It is assumed that the shank resistance is fully mobilized. Two parts can be combined to a resultant load, T_s, acting at the fluke with an offset, $L_{off\,2}$, as follows

$$T_s = \pm(4A_s + 2A_e N_c)s_u \tag{4.24}$$

$$M_s = T_s L_{off\,2} \tag{4.25}$$

$$L_{off\,2} = \frac{4A_s x_1 + 2A_e N_c x_2}{4A_s + 2A_e N_c} \tag{4.26}$$

where "+" ("-") denotes the upward (downward) direction; A_s is the area of shank side; A_e is the area of shank end; N_c is the bearing factor of shank end, taken as 7.5; s_u is the shear strength of soil; x_1 is the offset of the center of gravity of shank side area from the fluke; and x_2 is the offset of the center of gravity of the shank end area from the fluke. When the parallel component of the active load, T_a, is less than the resistance from the shank and flap, i.e. $F_{sa} + F_{sf} + T_s < 0$, T_s is not fully mobilized and becomes

$$T_s = -F_{sa} - F_{sf} \tag{4.27}$$

Therefore, the components of the resultant load acting at the fluke can be expressed as follows

$$F_{n1} = F_{na} + F_{nf} = T_a \sin(\theta_{flk} - \theta_a) + T_f \sin(\theta_{flk} - \theta_f) \tag{4.28}$$

$$F_{s1} = F_{sa} + F_{sf} + T_s = T_a \cos(\theta_{flk} - \theta_a) + T_f \cos(\theta_{flk} - \theta_f) + T_s \tag{4.29}$$

$$M_1 = M_a + M_f + M_s = T_a \cos(\theta_{flk} - \theta_a) L_{off\,1}$$

$$-T_f \sin(\theta_{flk} - \theta_f)\, L_1/2 + T_s L_{off\,2} \qquad (4.30)$$

The components of the load reacting at the flap can be expressed as follows

$$F_{n2} = T_f \sin(\theta_{flp} - \theta_f + \pi) \qquad (4.31)$$

$$F_{s2} = T_f \cos(\theta_{flp} - \theta_f + \pi) \qquad (4.32)$$

$$M_2 = F_{n2}\, L_2/2 \qquad (4.33)$$

Once the flap reaches the “stop” angle, it immediately stops rotating relative to the fluke and again rotates with the fluke as a rigid extension. To simplify, the flap at the “stop” angle is projected parallel to the fluke and acts as an extended part of the fluke again. Thus, the SEPLA keeps rotating with the length of the extended fluke equal to the projected length of the flap plus the original length of the fluke. Although this simplification does not give a rigorous solution but can make a rough estimate for the performance of the SEPLA at this stage. As previously described, the main aim of the “keying” process is to make the anchor line normal to the fluke as quickly as possible such that the ultimate capacity of the anchor will be mobilized. However, the anchor chain-fluke angle has already been beyond normal when the flap reaches the “stop” angle. Therefore, the model behavior of the SEPLA after that can be ignored unless there is a special need to assess post-peak behavior.

A method is presented here to estimate the behavior of the SEPLA as the flap is free to rotate back and forth. The boundary conditions for the fluke and flap at the hinge are expressed as

$$dx_1 = dx_2 \text{ and } dy_1 = dy_2 \tag{4.34}$$

where dx_1 and dy_1 are the horizontal and vertical components of the displacement for the top of the fluke; dx_2 and dy_2 are the horizontal and vertical components of the displacement for the bottom of the flap. Given a specific orientation and location of the SEPLA anchor, i.e. the fluke inclination, θ_{flk}, the flap inclination, θ_{flp}, from the horizontal and the embedment depth of the fluke centroid are known, as shown in Fig. 4.5, the displacements dx_1, dy_1, dx_2 and dy_2 can be calculated as

$$dx_1 = dn_1 \cos\left(\theta_{flk} - \frac{\pi}{2}\right) - ds_1 \sin\left(\theta_{flk} - \frac{\pi}{2}\right) - d\theta_1 \frac{L_1}{2} \sin\theta_{flk} \tag{4.35}$$

$$dy_1 = dn_1 \sin\left(\theta_{flk} - \frac{\pi}{2}\right) + ds_1 \cos\left(\theta_{flk} - \frac{\pi}{2}\right) + d\theta_1 \frac{L_1}{2} \cos\theta_{flk} \tag{4.36}$$

$$dx_2 = dn_2 \cos\left(\theta_{flp} - \frac{\pi}{2}\right) - ds_2 \sin\left(\theta_{flp} - \frac{\pi}{2}\right) + d\theta_2 \frac{L_2}{2} \sin\theta_{flp} \tag{4.37}$$

$$dy_2 = dn_2 \sin\left(\theta_{flp} - \frac{\pi}{2}\right) + ds_2 \cos\left(\theta_{flp} - \frac{\pi}{2}\right) - d\theta_2 \frac{L_2}{2} \cos\theta_{flp} \tag{4.38}$$

where dn_1 and ds_1 are the normal, parallel displacement increments and $d\theta_1$ is the rotation increment for the fluke; dn_2 and ds_2 are the normal, parallel displacement increments and $d\theta_2$ is the rotation increment for the flap. Substituting Eqs 4.28 ~ 4.33 into Eqs 4.12, 4.13 and 4.14 and then substituting Eqs 4.12, 4.13 and 4.14 into Eqs 4.35 ~ 4.38 gives the displacements with respect to T_a, θ_a, T_f and θ_f, which are expressed in the functional forms as

$$dx_1 = \lambda_1 \cdot f_1(T_a, \theta_a, T_f, \theta_f) \tag{4.39}$$

$$dy_1 = \lambda_1 \cdot f_2(T_a, \theta_a, T_f, \theta_f) \tag{4.40}$$

$$dx_2 = \lambda_2 \cdot g_1(T_f, \theta_f) \tag{4.41}$$

$$dy_2 = \lambda_2 \cdot g_2(T_f, \theta_f) \tag{4.42}$$

where λ_1 and λ_2 are positive scale factors for the fluke and flap. By substituting Eqs 4.39 ~ 4.42 into Eq. 4.34 and canceling λ_1 and λ_2, an equation can be obtained for describing the displacement boundary condition at the hinge of the SEPLA anchor as follows

$$\frac{f_1(T_a, \theta_a, T_f, \theta_f)}{f_2(T_a, \theta_a, T_f, \theta_f)} = \frac{g_1(T_f, \theta_f)}{g_2(T_f, \theta_f)} \tag{4.43}$$

Now a system of equations consists of four equations: the yield equation for the fluke that is obtained by substituting Eq. 4.28 ~ 4.30 into Eq. 4.4, the yield equation for the flap that is obtained by substituting Eq. 4.31 ~ 4.33 into Eq. 4.4, the anchor chain interaction Eq. 4.9 and the boundary condition Eq. 4.43. This system can be solved iteratively for the unknowns: T_a, θ_a, T_f and θ_f. By updating these parameters at failure step by step, the trajectory and corresponding capacities of the SEPLA can be predicted according to the preceding description.

When the flap rotates as a rigid extension of the fluke, the calculation becomes comparatively simpler. The length of the fluke is replaced by the extended length and hence the center of rotation moves up to the centroid of the extended fluke. The capacities and trajectory of the SEPLA during this stage can be obtained by iteratively solving Eqs 4.4 and 4.9. Consequently, the performance of the SEPLA during the entire “keying” process will be a combination of different stages mentioned above.

4.2 Results of Prediction

The function of the flap was assumed to facilitate the "keying" of the SEPLA and reduce the loss of embedment. To our knowledge, there has so far been little theoretical or experimental work that was conducted to verify the details of the "keying" process. To better understand the effects of the flap on the behavior of the SEPLA during the "keying" process, two different types of SEPLA anchors will be studied herein. They are the SEPLA without a flap and the SEPLA with a flap limited by "stop" angle (conventional SEPLA). The trajectory and corresponding capacities of the SEPLAs will be predicted.

4.2.1 SEPLA without Flap

The configuration of the SEPLA in this type follows the conventional SEPLA but without the "keying" flap. The fluke dimensions used herein are 10 ft (3m) x 24 ft (7.3 m) x 0.5 ft (0.15 m). The padeye is located in front of the fluke with a normal offset of 7 ft (2.1 m). Song et al. (2005) pointed out that the anchor capacity is not affected by its orientation for anchor embedment ratios (ratio of embedment depth of fluke centroid to anchor length) greater than 3. Here the SEPLA is assumed to be embedded in uniform soil with an embedment ratio of 5. To explore the influence of the anchor chain on the SEPLA, the behavior of the SEPLA is simulated for two different pullout directions, i.e. pullout under a constant angle of θ_a from the horizontal at the anchor padeye (not including anchor-chain interaction) and pullout under a constant angle of θ_o from the horizontal at the mudline (including anchor-chain interaction).

Plotted in Figs 4.6-A, 4.6-B, 4.7-A and 4.7-B are the normalized trajectories

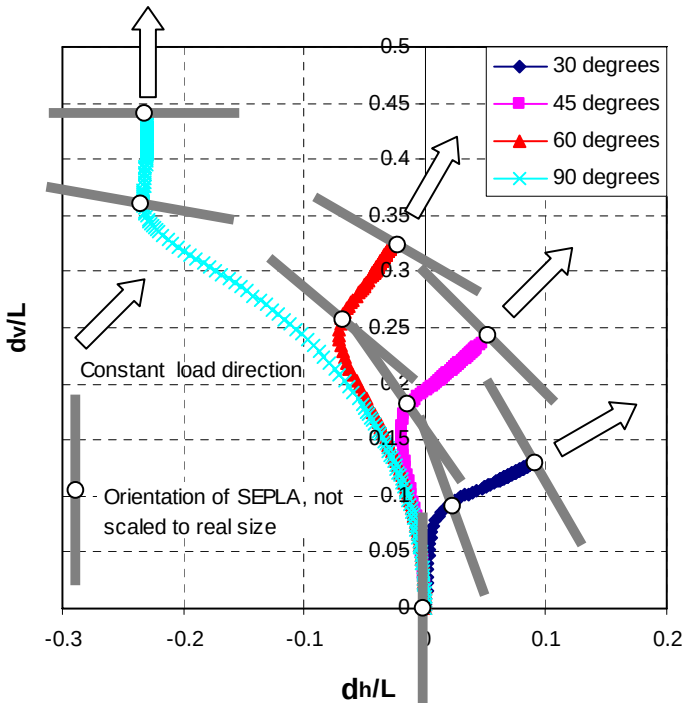

Fig. 4.6-A Trajectories of SEPLA without flap, not including anchor chain interaction

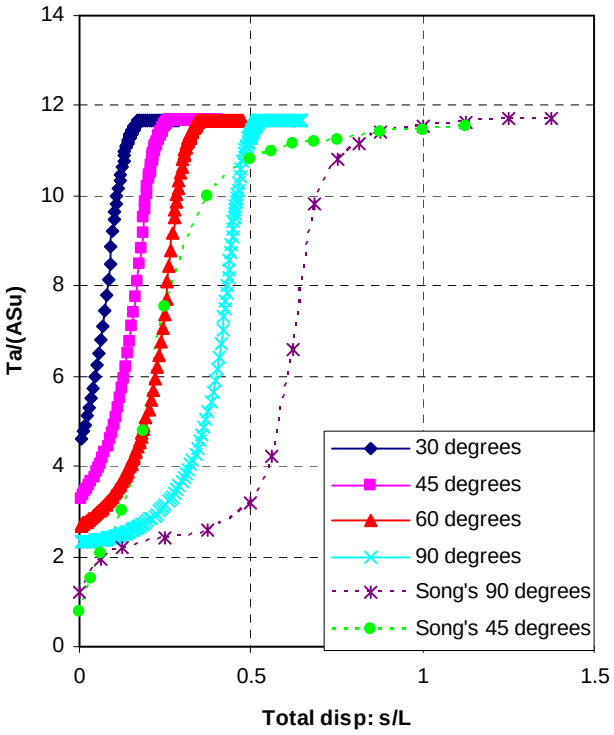

Fig. 4.6-B Capacities of SEPLA without flap, not including anchor chain interaction

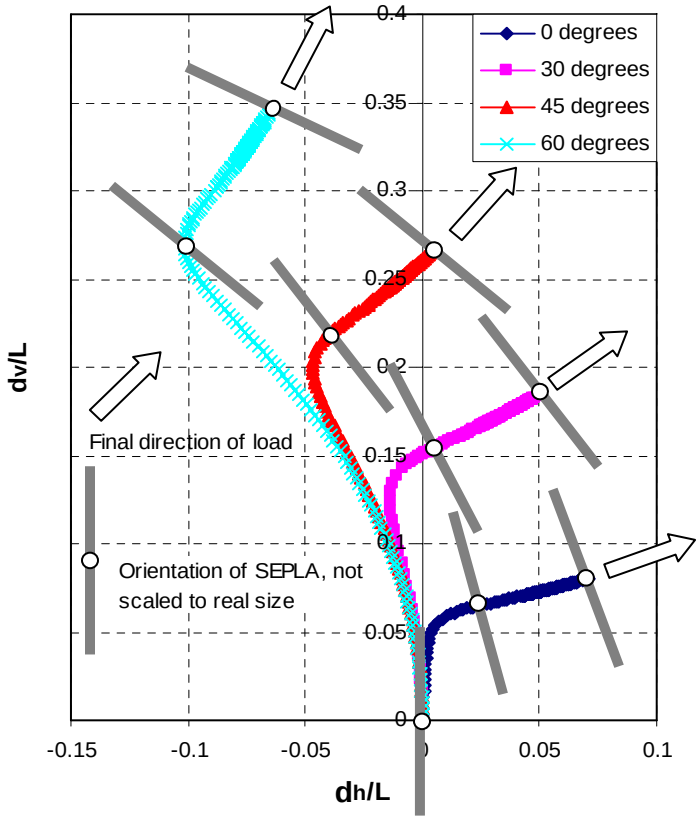

Fig. 4.7-A Trajectories of SEPLA without flap, including anchor chain interaction

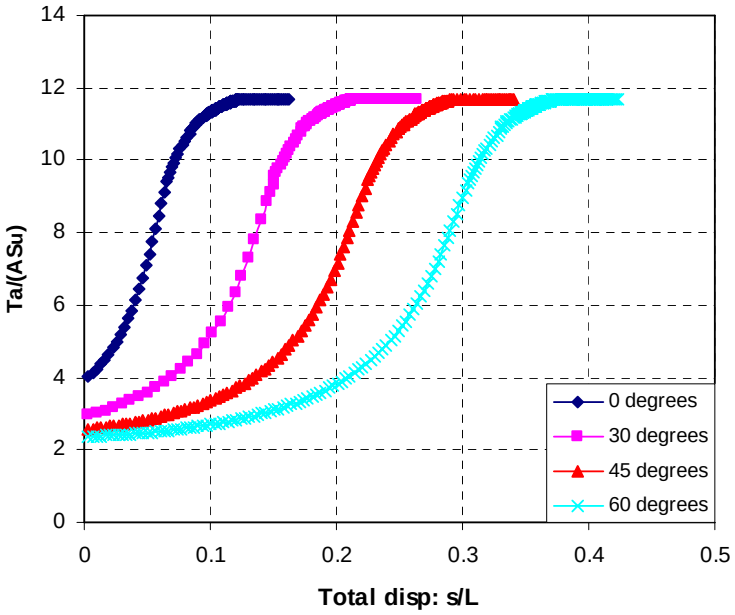

Fig. 4.7-B Capacities of SEPLA without flap, including anchor chain interaction

and corresponding capacities of the SEPLA under various pullout angles. It is noted that all trajectories through this study are referred to as those of the centroid of the fluke. The displacement of the SEPLA with a varying orientation can be resolved into two components: sliding parallel to the fluke and translation normal to the fluke. As a result, the SEPLA is likely to have an initial negative horizontal displacement while it rotates. Figs 4.6-A and 4.7-A show that most trajectories follow the same trend in which the SEPLA initially moves backward and then forward while it goes up. The backward movement mainly depends on the pullout angle and vanishes when the pullout angle is small, e.g. 30^o in Fig. 4.6-A and 0^o in Fig. 4.7-A. Song et al. (2005) carried out a finite element analysis to simulate the continuous rotation of a strip SEPLA with the length of 4m and the padeye eccentricity of 2.5 m. They assumed that the SEPLA was embedded in uniform soil with an embedment ratio of 5. The anchor-chain interaction was not included, and the anchor rotation was simulated for 45^o and 90^o pullout at the padeye. The results show that the SEPLA initially moves backward as predicted by the current model, and the embedment losses are $0.25L$ and $0.6L$, respectively. The embedment losses are in reasonable agreement with Fig. 4.6-A where they are $0.24L$ for 45^o pullout and $0.44L$ for 90^o pullout. Gaudin et al. (2006) performed centrifuge tests for a SEPLA that has a square fluke and no flap where the prototype strength of soil increases linearly with a gradient of 1.1 kPa/m from 0 at the surface. The SEPLA was embedded with an embedment ratio of 4. The chain formed a 45^o inclination at the mudline and hence the anchor chain interaction was involved. The test results show that the embedment losses were in a range of $0.9 \sim 1.3L$. They are significant greater than $0.27L$ by the current

model, shown in Fig. 4.7-A, as well as Song et al. (2005) solutions for the strip fluke. This discrepancy indicates that the aspect ration of plate and the strength profile of soil might have a significant effect on the embedment loss. The anchor orientations, not scaled to the real anchor size, in Figs 4.6-A and 4.7-A show that the SEPLA gradually keys itself to translate along the direction of pullout where the load becomes perpendicular to the fluke, which indicates that the ultimate capacity has been mobilized. However, the SEPLA might not translate ideally this way in the real world because the anchor will not be loaded by an exact centric load. The previous study on the out-of-plane loading of plate anchors suggests that the plate anchor has a trend toward sliding along the plate under even a slightly eccentric load.

Figs 4.6-B and 4.7-B show how the anchor capacity is mobilized against the total anchor displacement that is referred to as the cumulative displacement from the starting location along the trajectory. Song et al. (2005) solutions for 45^o and 90^o pullout are also plotted in Fig. 4.6-B to be compared with. The curves predicted by the current model follow almost the same trend as those by Song et al. (2005). They finally reach a plateau at the ultimate value of $N_p = 11.67$, which is in excellent agreement with the solution of 11.5-11.7 reported by Song et al. (2005). The only discrepancy is the total displacements by Song et al. (2005) are greater than the corresponding ones by the current model. This is likely due to different offset of the padeye and the shank-soil resistance that is not considered in Song et al. (2005) analysis.

The anchor chain makes the chain angle, θ_a, at the padeye greater than the pullout angle, θ_o, at the mudline due to its reverse catenary profile within the soil,

although there is a trend toward decreasing θ_a to θ_o during the pullout. For the pullout angles of 0^o, 30^o, 45^o and 60^o at the mudline in Fig. 4.7, the results show that the corresponding chain angles at the padeye decrease to about 20^o, 36^o, 49^o and 63^o, respectively, when the anchor chain becomes perpendicular to the fluke. Of course, the chain angle at the padeye mainly depends on the depth of embedment, soil strength and chain properties etc. The greater the pullout angle is, the more the loss of anchor embedment would be. Thus, the anchor chain somewhat contributes to the loss of anchor embedment, although its frictional capacity significantly increases the overall anchor capacity.

4.2.2 SEPLA with Flap

As described previously, the conventional SEPLA is designed to have a "keying" flap that can rotate backward within a "stop" angle from the fluke but is strictly restricted from rotating forward. The dimensions of the fluke and shank here are chosen to be consistent with the SEPLA without flap that was analyzed above. The length of the flap is set to be 3 ft (0.91 m). The SEPLA is also assumed to be embedded in uniform soil with an embedment ratio of 5. The effect of the anchor chain on the SEPLA has been studied in preceding section so it will not be included here.

Figs 4.8-A and B show the trajectories and corresponding capacities of the SEPLA with a flap under various pullout angles at the padeye. The typical variations in orientation of the SEPLA are plotted on the trajectories, showing the rotation of the flap relative to the fluke during the "keying" process. The results show that the entire "keying" process is divided into three stages of the mechanism of rotation. In the first

stage, the SEPLA rotates about the centroid of the extended fluke starting from the initial orientation as previously discussed. As the "keying" progresses the parallel component of the load gradually decreases and becomes less than the soil resistance in the parallel direction when the anchor line has an angle of 4^o from normal to the fluke. This indicates that sliding parallel to the fluke stops. It is found that the SEPLA still continues

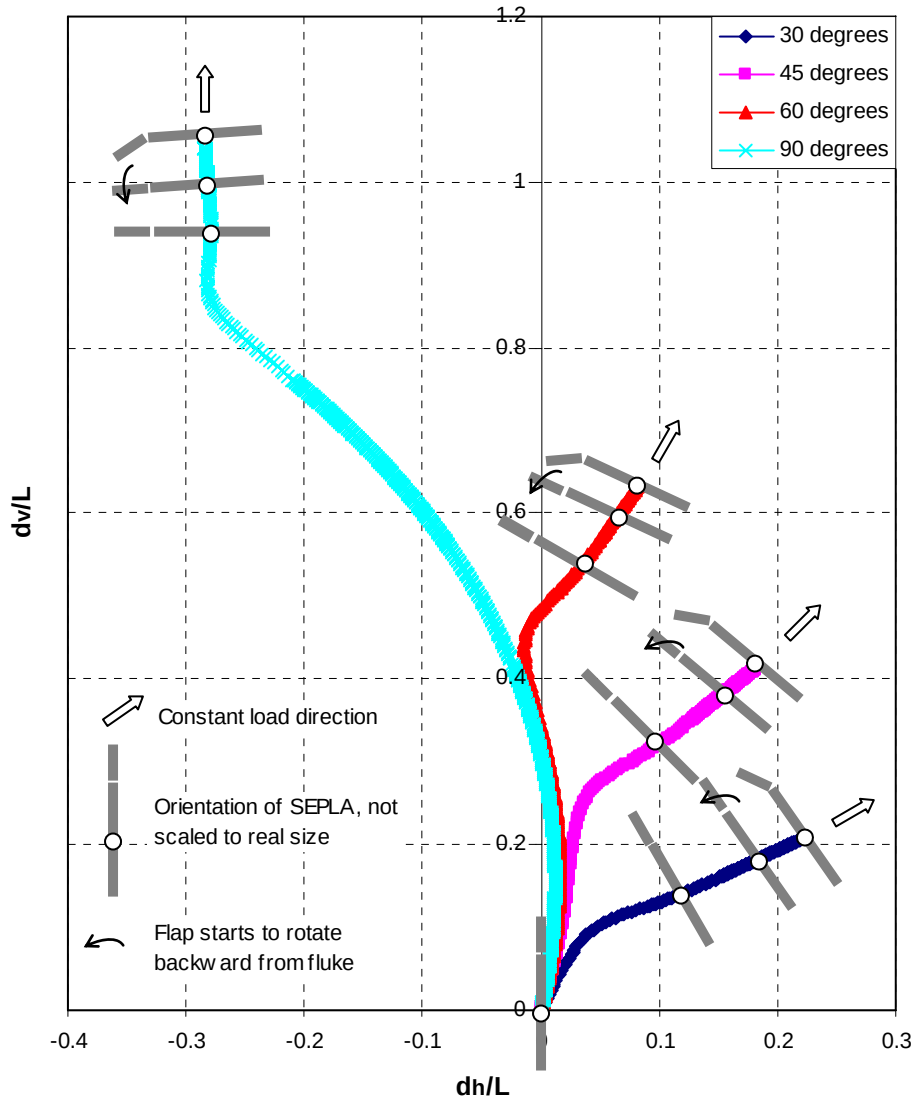

Fig. 4.8-A Trajectories of SEPLA with flap, not including anchor chain interaction

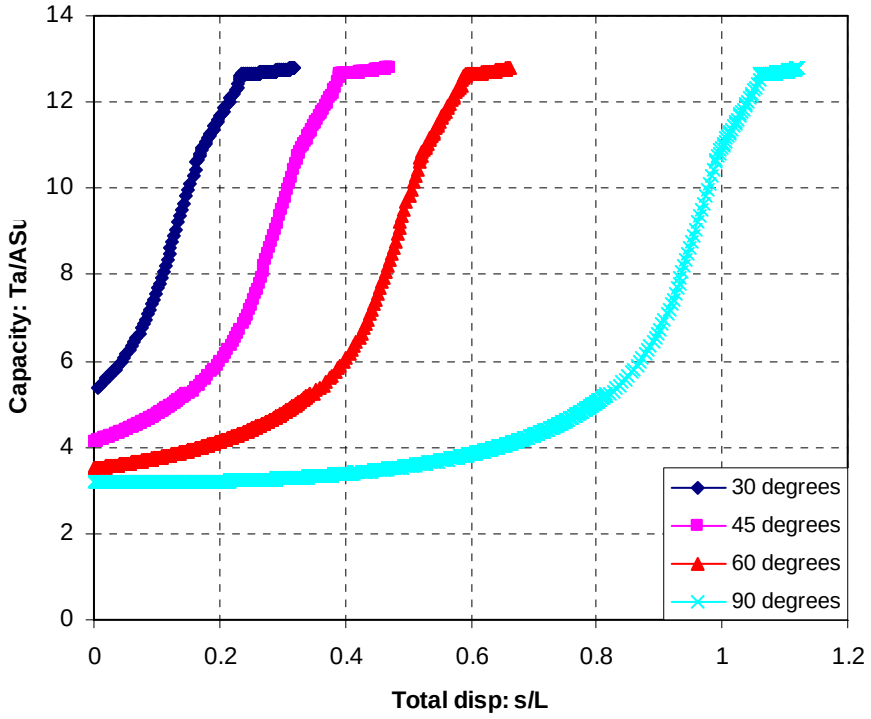

Fig. 4.8-B Capacities of SEPLA with flap, not including anchor chain interaction

to rotate as it reaches the target orientation, i.e. the anchor line is normal to the fluke. In addition, the flap does not begin to rotate backward relative to the fluke until a further rotation of about 4^o after the target orientation is achieved, as shown previously in Fig. 4.4. As the SEPLA rotates beyond normal to the direction of pullout, the parallel component of the load becomes negative and hence it has a tendency of sliding down the SEPLA parallel to the fluke and counter-rotating the SEPLA. The second stage comes once the flap starts to rotate backward from the fluke, indicating that the SEPLA rotates about the centroid of the original fluke. As a result, the offset of the normal load component vanishes and the moment component of the load sharply drops down to negative, which is in magnitude slightly less than the positive moment imposed by the

flap. Therefore, the resultant moment becomes very small such that the SEPLA only has a slight rotation, about 0.3°, as the flap rotates toward its "stop" angle. During this stage, the normal component of the load governs the movement of SEPLA and the SEPLA translates with a negligible rotation in the direction normal to the fluke. The third stage is where the flap has already reached the "stop" angle and rotates as a rigid extension of the fluke. During this stage, the flap makes the normal component of the load eccentric again and hence the SEPLA continues to rotate as it moves forward. Meanwhile, the negative parallel component of the load overcomes the soil resistance in the parallel direction, causing a displacement component of sliding down parallel to the fluke. The SEPLA does not stop rotating until the load goes through the center of rotation which is the centroid of the extended fluke. In principle, the SEPLA will finally translate in a direction which has a clockwise angle from the load direction, as shown in Fig. 4.9. If the pullout angle is small, the translation will probably be in a horizontal or slightly

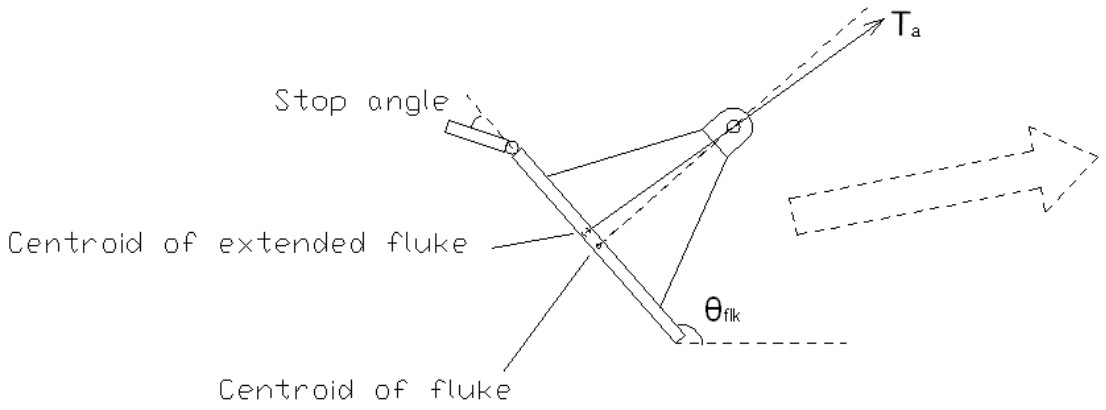

Fig. 4.9 Final orientation of SEPLA

downward direction. Because the predicted model path is already well beyond where the anchor chain becomes normal to the fluke, the third stage simulation was truncated. Therefore, the embedment loss and capacity of the SEPLA at the end of the second stage are taken to be the final solution in our model. The ultimate capacity of the SEPLA in uniform soil is determined by the SEPLA dimension so the curves in Fig. 4.8-B reach the same capacity that is $N_p = 12.79$.

4.2.3 Comparisons of SEPLA without Flap and with Flap

It was shown that the predicted solutions for the SEPLA without a flap agree reasonably well with the relevant known results. To see how the flap affects the behavior of SEPLA, comparisons are made between the results for the SEPLA with a flap and without a flap, not including the anchor chain interaction. The SEPLA with a flap does not stop rotating until it rotates past the target orientation that is perpendicular to the direction of load, but the embedment loss at the target orientation is important to compare with the SEPLA without a flap. Tabulated in Table 4.2 is a summary of the predicted results for both types of SEPLAs. It can be seen that no matter how much the

Table 4.2 Summary of Results Predicted by Model

SEPLA type	Embedment loss: dv/L								Capacity factor	Over rotation
	10^o	15^o	20^o	30^o	45^o	60^o	75^o	90^o		
Flap	0.01*	0.02*	0.05*	0.14*	0.32*	0.54*	0.75*	0.95*	12.79	4.7^o
	0.04	0.06	0.1	0.21	0.41	0.63	0.85	1.04		
No flap	0.01	0.03	0.06	0.13	0.23	0.32	0.39	0.43	11.67	0^o

*: Embedment loss at the target orientation

pullout angle is, the SEPLA without a flap exactly keys up to be normal to the direction of load whereas the one with a flap continues rotating to 4.7^o past normal. The predicted final embedment losses for the SEPLA with a flap are greater than the corresponding ones for the SEPLA without a flap, generally in a range of 1.6 ~ 2.4 times. Of course, the embedment losses may be compensated somewhat because the SEPLA with flap is likely to slightly dive down after the flap reaches the "stop" angle if the pullout angle is small. If comparing them at the target orientation where they have the same level of rotation, the embedment losses for the SEPLA with flap are still greater than the one without flap when the pullout angle is more than 30^o, but a little less when the pullout angle is smaller than 30^o. To show the impact of the flap during the entire "keying" process, Fig. 4.10-A shows the trajectories for both types of SEPLAs when they are pulled out by a load oriented at the padeye with angles of 30^o, 45^o and 60^o from the horizontal. The notches on the curves for the SEPLA with flap denote where the anchor becomes normal to the direction of load. The comparisons of related curves in Fig. 4.10-A show that the flap not only increases the embedment losses but also lengthens the trajectories. The fact that the flap makes the SEPLA traverse a longer distance to achieve the same level of rotation suggests that the flap may slightly hinder the "keying" of the SEPLA. Fig. 4.10-A also shows that all trajectories for the SEPLA without a flap are located behind the corresponding ones for the SEPLA with a flap and the SEPLA with a flap does not have initial backward movement, indicating that the flap makes it harder for the SEPLA to rotate.

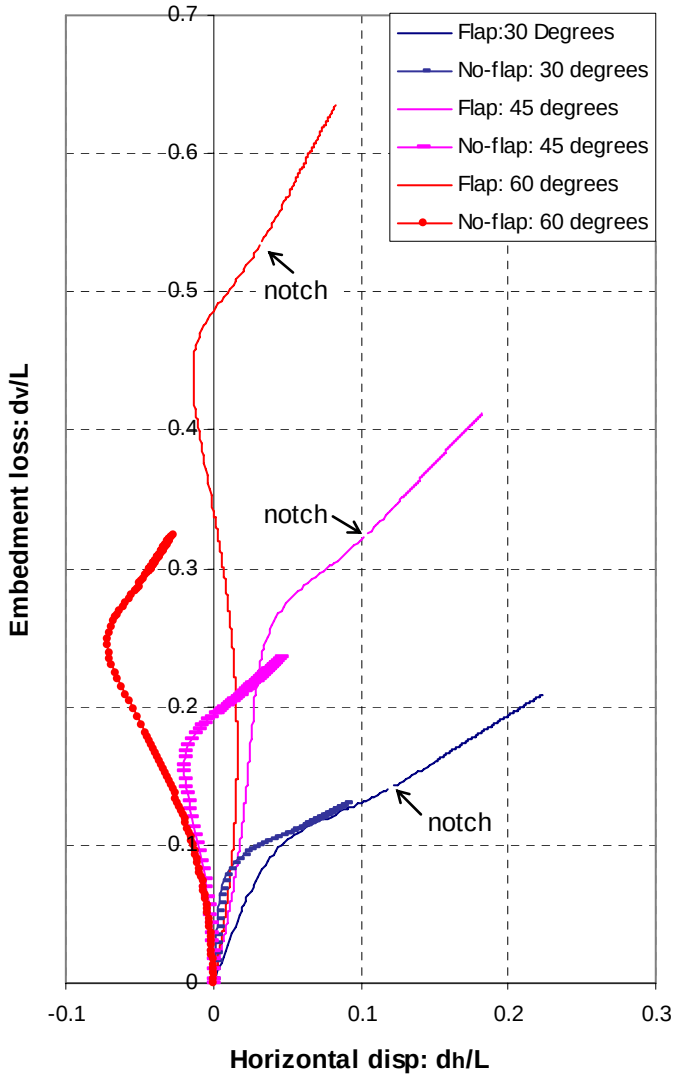

Fig. 4.10-A Comparisons of trajectories of SEPLA with flap and without flap under different angles of pullout

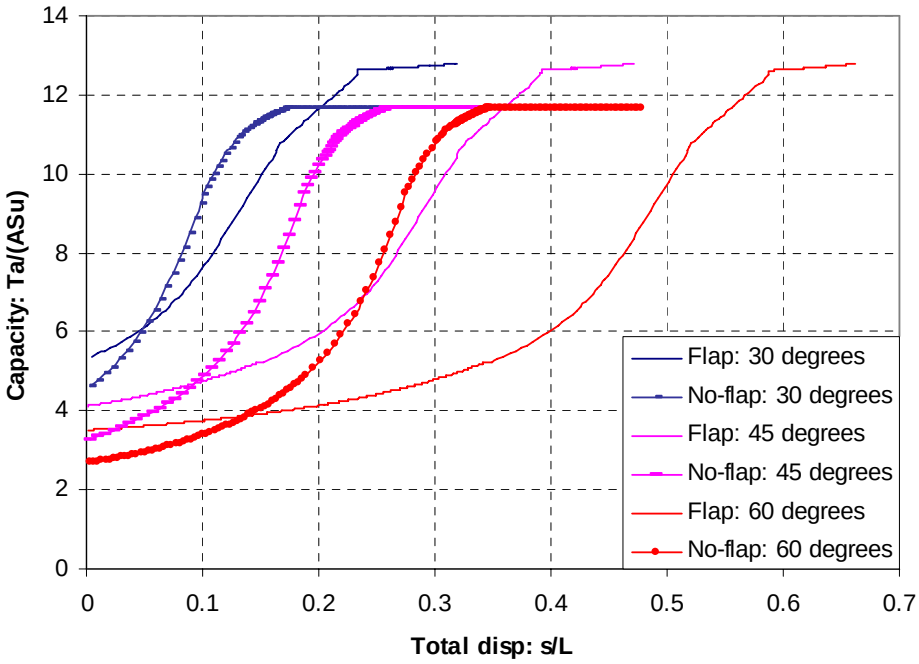

Fig. 4.10-B Comparisons of capacities of SEPLA with flap and without flap under different angles of pullout

Fig. 4.10-B presents the variation in capacities of both types of SEPLAs as they move along the trajectories in Fig. 4.10-A. It can be see that the capacity curves of the SEPLA without a flap have a steeper slope than those of the SEPLA with a flap. This indicates that the flap may actually slow down the mobilization of anchor capacity. The capacities of the SEPLA with a flap gradually increase up to the ultimate value of 12.79, which is about 10% higher than 11.67, the ultimate capacity of the SEPLA without a flap. This higher value is mainly contributed by the flap because it actually increases the bearing area of the SEPLA. However, the fluke is not perpendicular to the direction of load at final orientation due to the flap. This suggests that simply increasing the length of the fluke with a centric shank may be more efficient than adding the flap.

4.3 Conclusions

The behavior of the SEPLA under various conditions during the “keying” process has been analyzed using the proposed theoretical model. Consideration has been given to the effects of the anchor chain and soil resistance against the shank. The predicted results have been shown to be in reasonably good agreement with the related known solutions. The effect of flap has been examined theoretically by comparing the solutions for the SEPLA with and without flap. The results presented in this study lead to the following conclusions:

- The proposed model can predict the trajectory and corresponding capacities of the SEPLA during the “keying” process.
- The anchor chain makes the chain inclination at the padeye greater than the pullout angle at the mudline due to its reverse catenary shape within soil and hence increases the loss of embedment depth although the chain friction improves the overall anchor capacity.
- A SEPLA without the flap rotates to the final target orientation which is perpendicular to the direction of loading, but the SEPLA with the flap keeps rotating after reaching the target orientation since the normal component of the load becomes offset again.
- The flap gives rise to more loss of embedment depth and causes the SEPLA to travel a longer distance to achieve the same level of rotation. As a result, more soil in the vicinity of the SEPLA is disturbed. This suggests that the flap may hinder the “keying” of the SEPLA.

- The ultimate capacity achieved by the SEPLA with the flap is higher than that by the SEPLA without the flap because the flap increases the bearing area of the SEPLA.

CHAPTER V

CONCLUSIONS AND RECOMMENDATIONS

5.1 Conclusions

Investigations have been conducted on the undrained behavior of plate anchors, including out-of-plane loading of simple plates and performance of suction embedded plate anchors (SEPLA) during the “keying” process. For out-of-plane loading of plate anchors, finite element analyses were initially conducted to replicate two dimensional results previously obtained to verify/calibrate the modeling approach used in this study. Subsequently, three dimensional FE models were used to analyze the behavior of square and rectangular plates. These models were used to investigate plate anchor behavior under normal loads with eccentricity in any direction. A simple model was then fit to the FEM results to determine required fitting parameters for both square and rectangular plates. These simple models are analytical expressions of multi-axial failure interaction surfaces which include load normal to the plate and moments about two major axes of the plate. They fit the FEM results well and are also consistent with experimental results obtained in a companion experimental program conducted at the University of Texas at Austin. In addition, upper bound analyses were performed for parallel loading and torsion loading. These solutions were verified by FE models modified with a weak buffer zone around the plate. The previous simple models were then extended to include the parallel load and torque. These models can, in turn, be used both to predict anchor holding capacity and as yield surfaces. These surfaces can be used for capacity

assessment and conducting plastic limit analysis, a method conducting plastic limit analyses, a tool capable of predicting post yield anchor trajectory. The studies carried out herein show conclusively that out-of-plane loading, which will subject an anchor to eccentric loading, can cause a profound reduction in anchor capacity. The reduction is due to two effects: (1) the load eccentricity which causes the anchor to lose capacity due to interactions between different load components and (2) the reduced soil strength as the anchor is displaced upward in a normally consolidated soil profile. If the anchor is loaded in a fixed direction it is possible (although by no means certain) that the anchor could stabilize after its initial failure. Stabilization would seem to be more likely for a VLA if the shank or bridle remains in tact. However a MODU adrift is likely to load the anchor in changing directions. This in turn could cause a series of successive failures in which the anchor gradually works its way upward into weaker soil. Thus even if the anchor tended to stabilize momentarily, it seems likely that varying loading directions could eventually lead to pulling out of the anchor.

For SEPLA, the theoretical model based on the associated flow rule of plasticity was applied to predict the trajectory and varying capacity during the “keying” process. It was found that the reverse catenary shape of the anchor chain increases the loss of embedment depth of the SEPLA. Comparisons were made between the SEPLA with and without the “keying” flap, showing that the flap may actually hinder the “keying” of the SEPLA. The flap gives rise to more loss of embedment depth and causes the SEPLA to travel a longer distance to achieve the same level of rotation. As a result, more soil in the vicinity of the SEPLA is disturbed. The SEPLA without the flap stabilizes at the final

target orientation which is perpendicular to the direction of anchor line loading, but the SEPLA with the flap can keep rotating to some extent after reaching the target orientation.

5.2 Recommendations

The study carried out here is considered to be an initial investigation of the effects of out-of-plane loading on plate anchors. As such it was focused on what we believe are some of the more important issues. From these results it is clear that out-of-plane loading is an important issue in the analysis of plate anchor behavior where the moored vessel is adrift. This study considered infinitely thin plates, which can be used in an approximate manner to estimate for the plates with different thicknesses. However, since the thickness has a significant effect on the parallel and torsion loading behavior, a more detailed study of the problem is needed to explore these effects in order to understand the likely consequences better.

The flap is likely to hinder the “keying” of the SEPLA, but it can provide resistance against the upward sliding of the SEPLA after the installation is complete. An experimental program aimed at testing this conclusion is recommended.

REFERENCES

Andersen, K. H., Murff, J. D., and Randolph, M. R. (2003). “Deepwater anchor design practice-vertically loaded drag anchors”. *Phase II Report* to *API/Deepstar*, Norwegian Geotechnical Institute, Norway, Offshore Technology Research Center, USA and Centre for Offshore Foundation Systems, Australia.

Aubeny, C. P., Murff, J. D., and Roesset, J. M. (2001). “Geotechnical issues in deep and ultra-deep waters.” *Int. J. Geomech*., 1(2), 225-247.

Bransby, M. F., and O’Neill, M. P. (1999). “Drag anchor fluke-soil interaction in clays.” *Proc. Int. Symp. on Numerical Models in Geomechanics (NUMOG VII)*, Graz, Australia, 489-494

Calladine, C. R. (1969). *Engineering plasticity: theory and applications*. Pergamon Press, Oxford, United Kingdom.

Chen, W.F. (1975). *Limit analysis and soil plasticity*. Elsevier Publishing Co., Amsterdam, The Netherlands.

Chen, W. F., and Liu, X. L. (1990). *Limit analysis in soil mechanics*. Elsevier, Science Publishers, BV, Amsterdam, The Netherlands.

Degenkamp, G., and Dutta, A. (1989). “Soil resistances to embedded anchor chain in soft clay.” *Journal of Geotechnical Engineering*, 115(10), 1420-1438.

Dove, P., Treu, H., and Wilde, B. (1998). “Suction embedded plate anchor (SEPLA): a new anchoring solution for ultra-deep water mooring.” *Proc. DOT Conf.*, New Orleans, Louisiana.

D’souza, R. B., Dove, P. G. S., and Kelly, P. J. (1993). “Taut leg spread moorings: a cost-effective stationkeeping alternative for deepwater platforms.” *Proc. Annual Offshore Tech. Conf*., Houston, Texas, 41-55.

Gaudin, C., O’Loughlin, C. D., Randolph, M. F., and Lowmass, A. C. (2006). “Influence of the installation process on the performance of suction embedded plate anchors.” *Geotechnique*, 56(6), 381-391.

Hibbitt, Karlsson & Sorensen (HKS), Inc. (2006). *ABAQUS Version 6.6 user’s manual*. HKS, Inc, Pawtucket, Rhode Island.

Martin, C. M., and Randolph, M. F. (2001). "Applications of the lower and upper bound theorems of plasticity to collapse of circular foundations." *Proc. 10th Int. Conf. Int. Association of Computer Methods and Advances in Geomechnics*, Tucson, 2, 1417-1428.

Merifield, R. S., Sloan, S. W., and Yu, H. S. (2001). "Stability of plate anchors in undrained clay." *Geotechnique*, 51(2), 141-153.

Merifield, R. S., Lyamin, A. V., Sloan, S. W., and Yu, H. S. (2003). "Three-dimensional lower bound solutions for stability of plate anchors in clay." *Journal of Geotechnical and Geoenvironmental Engineering*, ASCE, 129(3), 243-253.

Murff, J. D. (1994). "Limit analysis of multi-footing foundation systems." *Proceedings of the 8th International Conference on Computer Methods and Advances in Geomechanics*, Morgantown, West Virginia, 1, 233-244.

Murff, J. D., Randolph M. F., Elkhatib, S., Kolk, H. J., Ruionen, R. M., Strom, P. J., and Thorne, C. P. (2005). "Vertically loaded plate anchors for deepwater applications." *Proc. Int. Symp. on Frontiers in Offshore Geotechnics, IS-FOG05*, Perth, 31-48.

Murff, J. D. (2006). Plastic limit analysis in geotechnical engineering class notes. Department of Civil Engineering, Texas A&M University, College Station, Texas.

Neubecker, S. R., and Randolph, M. F. (1995). Profile and frictional capacity of embedded anchor chains. *Journal of Geotechnical Engineering*, 121(11), 797-803

O'Neill, M. P., Bransby, M. F., and Randolph, M. F. (2003). "Drag anchor fluke-soil interaction in clays." *Canadian Geotechnical Journal*, 40, 78-94.

Prager, W. (1959). *An introduction to plasticity*. Addison Wesley Publishing Co., Reading, Massachusetts.

Randolph, M. F., Cassidy, M. J., Gourvenec, S. M., and Erbrich, C. (2005). "Challenges of offshore geotechnical engineering." *Proc. 16th Int. Conf. Soil Mech. Geotech. Engng.*, Osaka, 1, 123-176.

Rowe, R. K. (1978). "Soil-structure interaction analysis and its application to the prediction of anchor behavior." PhD thesis, University of Sydney, Australia.

Rowe, R. K., and Davis E. H. (1982). "The behavior of anchor plates in clay." *Geotechnique*, 32(1), 9-23.

Ruinen, R., and Degenkamp, G. (1999). "Advances in the development and operational experience with Stevmanta VLAs in deep water environments." *Moorings & Anchors for Deep and Ultra Deep Water Fields*, Aberdeen.

Ruinen, R. (2000). “The use of drag embedment anchors and vertical loaded anchors (VLAs) for deepwater moorings.” *Continuous Advances in Mooring & Anchorings*, Aberdeen, 1-19.

Song, Z., and Hu, Y. (2005). “Vertical pullout behavior of plate anchors in uniform clay.” *Proc. Int. Symp. on Frontiers in Offshore Geotechnics, IS-FOG05*, Perth, 205-211.

Song, Z., Hu, Y., and Randolph, M. F. (2005). “Pullout behavior of inclined plate anchors in uniform clay.” *Proc. 11th Int. Conf. of International Association of Computer Methods and Advances in Geomechanics*, Rurin, 3, 715-722.

Vivatrat, V., Valent, P. J., and Ponterio, A. A. (1982). The influence of chain friction on anchor pile design. *Proc. 14th Annu. Offshore Technol. Conf., Offshore Technology Conference, Houston, Texas*, 153-163.

Wilde, B. (2005). Program of centrifuge and field tests on the suction embedded plate anchor, *Report to SEPLA JIP*, InterMoor, Inc, Houston, Texas.

Vryhof Anchors (2005). *Anchor manual*. Krimpen ad Yssel, The Netherlands.

APPENDIX

A TYPICAL ABAQUS INPUT FILE

```
*Heading
** Job name: thickness Model name: Model-1
*Preprint, echo=NO, model=NO, history=NO, contact=NO
**
** PARTS
**
*Part, name=Part-bottom
*End Part
*Part, name=Part-inner1
*End Part
*Part, name=Part-inner2
*End Part
*Part, name=Part-middle
*End Part
*Part, name=Part-rigid
*End Part
*Part, name=Part-top
*End Part
**
** ASSEMBLY
**
*Assembly, name=Assembly
**
*Instance, name=Part-bottom-1, part=Part-bottom
       86.4,           0.,          3.2
*Node
      1,         -20.,         -20.,          13.
      2,         -20.,         -16.,          13.
      3,         -20.,         -12.,          13.
      4,         -20.,          -8.,          13.
      5,         -20.,          -4.,          13.
      6,         -20.,           0.,          13.
      7,         -20.,           4.,          13.
      8,         -20.,           8.,          13.
      9,         -20.,          12.,          13.
     10,         -20.,          16.,          13.
     11,         -20.,          20.,          13.
     12,         -20.,         -20.,     7.815439
     13,         -20.,         -16.,     7.815439
     14,         -20.,         -12.,     7.815439
     15,         -20.,          -8.,     7.815439
     16,         -20.,          -4.,     7.815439
     17,         -20.,           0.,     7.815439
                                 :
                                 :
                                 :
    597,          20.,         -12.,           0.
    598,          20.,          -8.,           0.
    599,          20.,          -4.,           0.
    600,          20.,           0.,           0.
    601,          20.,           4.,           0.
    602,          20.,           8.,           0.
    603,          20.,          12.,           0.
    604,          20.,          16.,           0.
    605,          20.,          20.,           0.
*Element, type=C3D8RH
  1,  56,  57,  68,  67,   1,   2,  13,  12
  2,  57,  58,  69,  68,   2,   3,  14,  13
```

```
  3,  58,  59,  70,  69,   3,   4,  15,  14
  4,  59,  60,  71,  70,   4,   5,  16,  15
  5,  60,  61,  72,  71,   5,   6,  17,  16
  6,  61,  62,  73,  72,   6,   7,  18,  17
  7,  62,  63,  74,  73,   7,   8,  19,  18
  8,  63,  64,  75,  74,   8,   9,  20,  19
  9,  64,  65,  76,  75,   9,  10,  21,  20
 10,  65,  66,  77,  76,  10,  11,  22,  21
 11,  67,  68,  79,  78,  12,  13,  24,  23
 12,  68,  69,  80,  79,  13,  14,  25,  24
 13,  69,  70,  81,  80,  14,  15,  26,  25
 14,  70,  71,  82,  81,  15,  16,  27,  26
 15,  71,  72,  83,  82,  16,  17,  28,  27
 16,  72,  73,  84,  83,  17,  18,  29,  28
 17,  73,  74,  85,  84,  18,  19,  30,  29
 18,  74,  75,  86,  85,  19,  20,  31,  30
 19,  75,  76,  87,  86,  20,  21,  32,  31
 20,  76,  77,  88,  87,  21,  22,  33,  32
 21,  78,  79,  90,  89,  23,  24,  35,  34
                                  :
                                  :
                                  :
394, 587, 588, 599, 598, 532, 533, 544, 543
395, 588, 589, 600, 599, 533, 534, 545, 544
396, 589, 590, 601, 600, 534, 535, 546, 545
397, 590, 591, 602, 601, 535, 536, 547, 546
398, 591, 592, 603, 602, 536, 537, 548, 547
399, 592, 593, 604, 603, 537, 538, 549, 548
400, 593, 594, 605, 604, 538, 539, 550, 549
** Region: (Section-soil:Picked)
*Elset, elset=_PickedSet4, internal, generate
   1,  400,    1
** Section: Section-soil
*Solid Section, elset=_PickedSet4, material=Material-soil
1.,
*End Instance
**
*Instance, name=Part-inner1-1, part=Part-inner1
        86.4,           0.,          -3.
*Node
      1,          -4.,           -4.,           3.
      2,          -4.,        -3.84,           3.
      3,          -4.,        -3.68,           3.
      4,          -4.,        -3.52,           3.
      5,          -4.,        -3.36,           3.
      6,          -4.,         -3.2,           3.
      7,          -4.,        -3.04,           3.
      8,          -4.,        -2.88,           3.
      9,          -4.,        -2.72,           3.
     10,          -4.,        -2.56,           3.
     11,          -4.,         -2.4,           3.
     12,          -4.,        -2.24,           3.
     13,          -4.,        -2.08,           3.
     14,          -4.,        -1.92,           3.
     15,          -4.,        -1.76,           3.
     16,          -4.,         -1.6,           3.
     17,          -4.,        -1.44,           3.
     18,          -4.,        -1.28,           3.
```

```
     19,          -4.,        -1.12,           3.
     20,          -4.,        -0.96,           3.
     21,          -4.,         -0.8,           3.
     22,          -4.,        -0.64,           3.
     23,          -4.,        -0.48,           3.
     24,          -4.,        -0.32,           3.
     25,          -4.,        -0.16,           3.
     26,          -4.,           0.,           3.
     27,          -4.,         0.16,           3.
                               :
                               :
                               :
  52009,           4.,         2.24,           0.
  52010,           4.,          2.4,           0.
  52011,           4.,         2.56,           0.
  52012,           4.,         2.72,           0.
  52013,           4.,         2.88,           0.
  52014,           4.,         3.04,           0.
  52015,           4.,          3.2,           0.
  52016,           4.,         3.36,           0.
  52017,           4.,         3.52,           0.
  52018,           4.,         3.68,           0.
  52019,           4.,         3.84,           0.
  52020,           4.,           4.,           0.
*Element, type=C3D8RH
    1,  1021,  1022,  1073,  1072,     1,     2,    53,    52
    2,  1022,  1023,  1074,  1073,     2,     3,    54,    53
    3,  1023,  1024,  1075,  1074,     3,     4,    55,    54
    4,  1024,  1025,  1076,  1075,     4,     5,    56,    55
    5,  1025,  1026,  1077,  1076,     5,     6,    57,    56
    6,  1026,  1027,  1078,  1077,     6,     7,    58,    57
    7,  1027,  1028,  1079,  1078,     7,     8,    59,    58
    8,  1028,  1029,  1080,  1079,     8,     9,    60,    59
    9,  1029,  1030,  1081,  1080,     9,    10,    61,    60
   10,  1030,  1031,  1082,  1081,    10,    11,    62,    61
   11,  1031,  1032,  1083,  1082,    11,    12,    63,    62
   12,  1032,  1033,  1084,  1083,    12,    13,    64,    63
   13,  1033,  1034,  1085,  1084,    13,    14,    65,    64
   14,  1034,  1035,  1086,  1085,    14,    15,    66,    65
   15,  1035,  1036,  1087,  1086,    15,    16,    67,    66
   16,  1036,  1037,  1088,  1087,    16,    17,    68,    67
   17,  1037,  1038,  1089,  1088,    17,    18,    69,    68
   18,  1038,  1039,  1090,  1089,    18,    19,    70,    69
   19,  1039,  1040,  1091,  1090,    19,    20,    71,    70
   20,  1040,  1041,  1092,  1091,    20,    21,    72,    71
   21,  1041,  1042,  1093,  1092,    21,    22,    73,    72
                               :
                               :
                               :
47491, 51959, 51960, 52011, 52010, 50939, 50940, 50991, 50990
47492, 51960, 51961, 52012, 52011, 50940, 50941, 50992, 50991
47493, 51961, 51962, 52013, 52012, 50941, 50942, 50993, 50992
47494, 51962, 51963, 52014, 52013, 50942, 50943, 50994, 50993
47495, 51963, 51964, 52015, 52014, 50943, 50944, 50995, 50994
47496, 51964, 51965, 52016, 52015, 50944, 50945, 50996, 50995
47497, 51965, 51966, 52017, 52016, 50945, 50946, 50997, 50996
47498, 51966, 51967, 52018, 52017, 50946, 50947, 50998, 50997
```

```
47499, 51967, 51968, 52019, 52018, 50947, 50948, 50999, 50998
47500, 51968, 51969, 52020, 52019, 50948, 50949, 51000, 50999
** Region: (Section-soil:Picked)
*Elset, elset=_PickedSet3, internal, generate
     1,  47500,      1
** Section: Section-soil
*Solid Section, elset=_PickedSet3, material=Material-soil
1.,
*End Instance
**
*Instance, name=Part-inner2-1, part=Part-inner2
        86.4,           0.,          0.2
*Node
      1,          -4.,          -4.,           3.
      2,          -4.,        -3.84,           3.
      3,          -4.,        -3.68,           3.
      4,          -4.,        -3.52,           3.
      5,          -4.,        -3.36,           3.
      6,          -4.,         -3.2,           3.
      7,          -4.,        -3.04,           3.
      8,          -4.,        -2.88,           3.
      9,          -4.,        -2.72,           3.
     10,          -4.,        -2.56,           3.
     11,          -4.,         -2.4,           3.
     12,          -4.,        -2.24,           3.
     13,          -4.,        -2.08,           3.
     14,          -4.,        -1.92,           3.
                                  :
                                  :
                                  :
  52010,           4.,          2.4,           0.
  52011,           4.,         2.56,           0.
  52012,           4.,         2.72,           0.
  52013,           4.,         2.88,           0.
  52014,           4.,         3.04,           0.
  52015,           4.,          3.2,           0.
  52016,           4.,         3.36,           0.
  52017,           4.,         3.52,           0.
  52018,           4.,         3.68,           0.
  52019,           4.,         3.84,           0.
  52020,           4.,           4.,           0.
*Element, type=C3D8RH
    1,  1021,  1022,  1073,  1072,     1,     2,    53,    52
    2,  1022,  1023,  1074,  1073,     2,     3,    54,    53
    3,  1023,  1024,  1075,  1074,     3,     4,    55,    54
    4,  1024,  1025,  1076,  1075,     4,     5,    56,    55
    5,  1025,  1026,  1077,  1076,     5,     6,    57,    56
    6,  1026,  1027,  1078,  1077,     6,     7,    58,    57
    7,  1027,  1028,  1079,  1078,     7,     8,    59,    58
    8,  1028,  1029,  1080,  1079,     8,     9,    60,    59
    9,  1029,  1030,  1081,  1080,     9,    10,    61,    60
   10,  1030,  1031,  1082,  1081,    10,    11,    62,    61
   11,  1031,  1032,  1083,  1082,    11,    12,    63,    62
   12,  1032,  1033,  1084,  1083,    12,    13,    64,    63
   13,  1033,  1034,  1085,  1084,    13,    14,    65,    64
   14,  1034,  1035,  1086,  1085,    14,    15,    66,    65
   15,  1035,  1036,  1087,  1086,    15,    16,    67,    66
   16,  1036,  1037,  1088,  1087,    16,    17,    68,    67
```

```
   17,  1037,  1038,  1089,  1088,    17,    18,    69,    68
   18,  1038,  1039,  1090,  1089,    18,    19,    70,    69
                                 :
                                 :
                                 :
47494, 51962, 51963, 52014, 52013, 50942, 50943, 50994, 50993
47495, 51963, 51964, 52015, 52014, 50943, 50944, 50995, 50994
47496, 51964, 51965, 52016, 52015, 50944, 50945, 50996, 50995
47497, 51965, 51966, 52017, 52016, 50945, 50946, 50997, 50996
47498, 51966, 51967, 52018, 52017, 50946, 50947, 50998, 50997
47499, 51967, 51968, 52019, 52018, 50947, 50948, 50999, 50998
47500, 51968, 51969, 52020, 52019, 50948, 50949, 51000, 50999
** Region: (Section-soil:Picked)
*Elset, elset=_PickedSet3, internal, generate
     1,  47500,      1
** Section: Section-soil
*Solid Section, elset=_PickedSet3, material=Material-soil
1.,
*End Instance
**
*Instance, name=Part-middle-1, part=Part-middle
        86.4,           0.,          -3.
*Node
      1,         -20.,          20.,          6.2
      2,          20.,          20.,          6.2
      3,          20.,          20.,           0.
      4,         -20.,          20.,           0.
      5,           4.,           4.,          6.2
      6,           4.,           4.,           0.
      7,          -4.,           4.,           0.
      8,          -4.,           4.,          6.2
      9,           4.,          -4.,          6.2
     10,          20.,         -20.,          6.2
     11,          20.,         -20.,           0.
     12,           4.,          -4.,           0.
     13,         -20.,         -20.,          6.2
     14,         -20.,         -20.,           0.
     15,          -4.,          -4.,          6.2
     16,          -4.,          -4.,           0.
     17,    -14.28571,          20.,          6.2
     18,    -8.571428,          20.,          6.2
     19,    -2.857143,          20.,          6.2
                                 :
                                 :
                                 :
   1003,    -4.904068,    -3.502906,     2.066667
   1004,    -4.904068,    -2.101744,     2.066667
   1005,    -4.904068,   -0.7005812,     2.066667
   1006,    -4.904068,    0.7005812,     2.066667
   1007,    -4.904068,     2.101744,     2.066667
   1008,    -4.904068,     3.502906,     2.066667
*Element, type=C3D8RH
  1,  62, 237, 673, 209,   1,  17, 185,  32
  2, 237, 238, 674, 673,  17,  18, 186, 185
  3, 238, 239, 675, 674,  18,  19, 187, 186
  4, 239, 240, 676, 675,  19,  20, 188, 187
  5, 240, 241, 677, 676,  20,  21, 189, 188
```

```
  6, 241, 242, 678, 677,  21,  22, 190, 189
  7, 242,  70, 223, 678,  22,   2,  23, 190
  8, 209, 673, 679, 210,  32, 185, 191,  31
  9, 673, 674, 680, 679, 185, 186, 192, 191
 10, 674, 675, 681, 680, 186, 187, 193, 192
 11, 675, 676, 682, 681, 187, 188, 194, 193
 12, 676, 677, 683, 682, 188, 189, 195, 194
 13, 677, 678, 684, 683, 189, 190, 196, 195
 14, 678, 223, 224, 684, 190,  23,  24, 196
 15, 210, 679, 279,  49,  31, 191,  30,   4
 16, 679, 680, 280, 279, 191, 192,  29,  30
 17, 680, 681, 281, 280, 192, 193,  28,  29
 18, 681, 682, 282, 281, 193, 194,  27,  28
 19, 682, 683, 283, 282, 194, 195,  26,  27
 20, 683, 684, 284, 283, 195, 196,  25,  26
 21, 684, 224,  69, 284, 196,  24,   3,  25
                                 :
                                 :
                                 :
666,  139,  583,  179,   16,  480, 1003,  667,  153
667,  583,  584,  180,  179, 1003, 1004,  668,  667
668,  584,  585,  181,  180, 1004, 1005,  669,  668
669,  585,  586,  182,  181, 1005, 1006,  670,  669
670,  586,  587,  183,  182, 1006, 1007,  671,  670
671,  587,  588,  184,  183, 1007, 1008,  672,  671
672,  588,   48,    7,  184, 1008,  222,   55,  672
** Region: (Section-soil:Picked)
*Elset, elset=_PickedSet2, internal, generate
   1,  672,    1
** Section: Section-soil
*Solid Section, elset=_PickedSet2, material=Material-soil
1.,
*End Instance
**
*Instance, name=Part-rigid-1, part=Part-rigid
        86.4,           0.,           0.
*Node
      1,         -2.2,          2.2,           0.
      2,         -2.2,         -2.2,           0.
      3,          -4.,          -4.,           0.
      4,          2.2,          2.2,           0.
      5,          -4.,           4.,           0.
      6,           4.,           4.,           0.
      7,          2.2,         -2.2,           0.
      8,           4.,          -4.,           0.
      9,          2.2,         -2.2,          0.2
     10,         -2.2,         -2.2,          0.2
     11,         -2.2,          2.2,          0.2
     12,          2.2,          2.2,          0.2
     13,           4.,          -4.,          0.2
     14,           4.,           4.,          0.2
                                 :
                                 :
                                 :
  13529,    0.9230769,     1.846154,         0.15
  13530,     1.076923,     1.846154,         0.15
  13531,     1.230769,     1.846154,         0.15
```

```
  13532,     1.384615,     1.846154,         0.15
  13533,     1.538462,     1.846154,         0.15
  13534,     1.692308,     1.846154,         0.15
  13535,     1.846154,     1.846154,         0.15
*Element, type=C3D8RH
   1,   309,   997,   953,   310,  4253,  7308,  7264,  4252
   2,   997,   998,   954,   953,  7308,  7309,  7265,  7264
   3,   998,   999,   955,   954,  7309,  7310,  7266,  7265
   4,   999,  1000,   956,   955,  7310,  7311,  7267,  7266
   5,  1000,  1001,   957,   956,  7311,  7312,  7268,  7267
   6,  1001,  1002,   958,   957,  7312,  7313,  7269,  7268
   7,  1002,  1003,   959,   958,  7313,  7314,  7270,  7269
   8,  1003,  1004,   960,   959,  7314,  7315,  7271,  7270
   9,  1004,  1005,   961,   960,  7315,  7316,  7272,  7271
  10,  1005,  1006,   962,   961,  7316,  7317,  7273,  7272
  11,  1006,   104,     1,   962,  7317,  4827,   339,  7273
  12,   308,  1007,   997,   309,  4254,  7318,  7308,  4253
  13,  1007,  1008,   998,   997,  7318,  7319,  7309,  7308
                              :
                              :
                              :
10425, 13528, 13529,  5008,  5009,  7256,  7257,   708,   707
10426, 13529, 13530,  5007,  5008,  7257,  7258,   709,   708
10427, 13530, 13531,  5006,  5007,  7258,  7259,   710,   709
10428, 13531, 13532,  5005,  5006,  7259,  7260,   711,   710
10429, 13532, 13533,  5004,  5005,  7260,  7261,   712,   711
10430, 13533, 13534,  5003,  5004,  7261,  7262,   713,   712
10431, 13534, 13535,  5002,  5003,  7262,  7263,   714,   713
10432, 13535,  5189,   715,  5002,  7263,   803,    22,   714
*Node
  13536,           0.,           0.,           0.
*Nset, nset=Part-rigid-1-RefPt_, internal
13536,
** Region: (Section-soil:Picked), (Controls:Default)
*Elset, elset=_PickedSet9, internal, generate
    1,  6896,     1
** Section: Section-soil
*Solid Section, elset=_PickedSet9, material=Material-soil
1.,
** Region: (Section-soil2:Picked), (Controls:EC-1)
*Elset, elset=_PickedSet11, internal
 6897, 6898, 6899, 6900, 6901, 6902, 6903, 6904, 6905, 6906, 6907, 6908, 6909,
6910, 6911, 6912
 6913, 6914, 6915, 6916, 6917, 6918, 6919, 6920, 6921, 6922, 6923, 6924, 6925,
6926, 6927, 6928
 6929, 6930, 6931, 6932, 6933, 6934, 6935, 6936, 6937, 6938, 6939, 6940, 6941,
6942, 6943, 6944
 6945, 6946, 6947, 6948, 6949, 6950, 6951, 6952, 6953, 6954, 6955, 6956, 6957,
6958, 6959, 6960
 6961, 6962, 6963, 6964, 6965, 6966, 6967, 6968, 6969, 6970, 6971, 6972, 6973,
6974, 6975, 6976
 6977, 6978, 6979, 6980, 6981, 6982, 6983, 6984, 6985, 6986, 6987, 6988, 6989,
6990, 6991, 6992
 6993, 6994, 6995, 6996, 6997, 6998, 6999, 7000, 7001, 7002, 7003, 7004, 7005,
7006, 7007, 7008
 7009, 7010, 7011, 7012, 7013, 7014, 7015, 7016, 7017, 7018, 7019, 7020, 7021,
7022, 7023, 7024
```

```
 7025, 7026, 7027, 7028, 7029, 7030, 7031, 7032, 7033, 7034, 7035, 7036, 7037,
7038, 7039, 7040
 7041, 7042, 7043, 7044, 7045, 7046, 7047, 7048, 7049, 7050, 7051, 7052, 7053,
7054, 7055, 7056
                                  :
                                  :
                                  :
 9001, 9002, 9003, 9004, 9005, 9006, 9007, 9008, 9009, 9010, 9011, 9012, 9013,
9014, 9015, 9016
 9017, 9018, 9019, 9020, 9021, 9022, 9023, 9024, 9025, 9026, 9027, 9028, 9029,
9030, 9031, 9032
 9033, 9034, 9035, 9036, 9037, 9038, 9039, 9040, 9041, 9042, 9043, 9044, 9045,
9046, 9047, 9048
 9049, 9050, 9051, 9052, 9053, 9054, 9055, 9056, 9057, 9058, 9059, 9060, 9061,
9062, 9063, 9064
 9065, 9066, 9067, 9068, 9069, 9070, 9071, 9072, 9073, 9074, 9075, 9076, 9077,
9078, 9079, 9080
** Section: Section-soil2
*Solid Section, elset=_PickedSet11, controls=EC-1, material=Material-soil2
1.,
** Region: (Section-soil:Picked), (Controls:EC-1)
*Elset, elset=_PickedSet10, internal
  7521,  7522,  7523,  7524,  7525,  7526,  7527,  7528,  7529,  7530,  7531,
7532,  7533,  7534,  7535,  7536
  7537,  7538,  7539,  7540,  7541,  7542,  7543,  7544,  7545,  7546,  7547,
7548,  7549,  7550,  7551,  7552
  7553,  7554,  7555,  7556,  7557,  7558,  7559,  7560,  7561,  7562,  7563,
7564,  7565,  7566,  7567,  7568
  7569,  7570,  7571,  7572,  7573,  7574,  7575,  7576,  7577,  7578,  7579,
7580,  7581,  7582,  7583,  7584
  7585,  7586,  7587,  7588,  7589,  7590,  7591,  7592,  7593,  7594,  7595,
7596,  7597,  7598,  7599,  7600
  7601,  7602,  7603,  7604,  7605,  7606,  7607,  7608,  7609,  7610,  7611,
7612,  7613,  7614,  7615,  7616
  7617,  7618,  7619,  7620,  7621,  7622,  7623,  7624,  7625,  7626,  7627,
7628,  7629,  7630,  7631,  7632
  7633,  7634,  7635,  7636,  7637,  7638,  7639,  7640,  7641,  7642,  7643,
7644,  7645,  7646,  7647,  7648
                                  :
                                  :
                                  :
 10353, 10354, 10355, 10356, 10357, 10358, 10359, 10360, 10361, 10362, 10363,
10364, 10365, 10366, 10367, 10368
 10369, 10370, 10371, 10372, 10373, 10374, 10375, 10376, 10377, 10378, 10379,
10380, 10381, 10382, 10383, 10384
 10385, 10386, 10387, 10388, 10389, 10390, 10391, 10392, 10393, 10394, 10395,
10396, 10397, 10398, 10399, 10400
 10401, 10402, 10403, 10404, 10405, 10406, 10407, 10408, 10409, 10410, 10411,
10412, 10413, 10414, 10415, 10416
 10417, 10418, 10419, 10420, 10421, 10422, 10423, 10424, 10425, 10426, 10427,
10428, 10429, 10430, 10431, 10432
** Section: Section-soil
*Solid Section, elset=_PickedSet10, controls=EC-1, material=Material-soil
1.,
*End Instance
**
*Instance, name=Part-top-1, part=Part-top
```

```
       86.4,           0.,         -16.
*Node
      1,         -20.,         -20.,          13.
      2,         -20.,         -15.,          13.
      3,         -20.,         -10.,          13.
      4,         -20.,          -5.,          13.
      5,         -20.,           0.,          13.
      6,         -20.,           5.,          13.
      7,         -20.,          10.,          13.
      8,         -20.,          15.,          13.
      9,         -20.,          20.,          13.
     10,         -20.,         -20.,     11.27181
     11,         -20.,         -15.,     11.27181
                                  :
                                  :
                                  :
    395,          20.,          15.,     5.184561
    396,          20.,          20.,     5.184561
    397,          20.,         -20.,           0.
    398,          20.,         -15.,           0.
    399,          20.,         -10.,           0.
    400,          20.,          -5.,           0.
    401,          20.,           0.,           0.
    402,          20.,           5.,           0.
    403,          20.,          10.,           0.
    404,          20.,          15.,           0.
    405,          20.,          20.,           0.
*Element, type=C3D8RH
  1,  46,  47,  56,  55,   1,   2,  11,  10
  2,  47,  48,  57,  56,   2,   3,  12,  11
  3,  48,  49,  58,  57,   3,   4,  13,  12
  4,  49,  50,  59,  58,   4,   5,  14,  13
  5,  50,  51,  60,  59,   5,   6,  15,  14
  6,  51,  52,  61,  60,   6,   7,  16,  15
  7,  52,  53,  62,  61,   7,   8,  17,  16
  8,  53,  54,  63,  62,   8,   9,  18,  17
  9,  55,  56,  65,  64,  10,  11,  20,  19
 10,  56,  57,  66,  65,  11,  12,  21,  20
 11,  57,  58,  67,  66,  12,  13,  22,  21
                                  :
                                  :
                                  :

249, 388, 389, 398, 397, 343, 344, 353, 352
250, 389, 390, 399, 398, 344, 345, 354, 353
251, 390, 391, 400, 399, 345, 346, 355, 354
252, 391, 392, 401, 400, 346, 347, 356, 355
253, 392, 393, 402, 401, 347, 348, 357, 356
254, 393, 394, 403, 402, 348, 349, 358, 357
255, 394, 395, 404, 403, 349, 350, 359, 358
256, 395, 396, 405, 404, 350, 351, 360, 359
** Region: (Section-soil:Picked), (Controls:Default)
*Elset, elset=_PickedSet4, internal, generate
   1,  256,    1
** Section: Section-soil
*Solid Section, elset=_PickedSet4, material=Material-soil
1.,
```

```
*End Instance
*Nset, nset=_PickedSet491, internal, instance=Part-rigid-1
 13536,
*Nset, nset=_PickedSet519, internal, instance=Part-bottom-1
   1,   2,   3,   4,   5,   6,   7,   8,   9,  10,  11,  12,  13,  14,  15,  16
  17,  18,  19,  20,  21,  22,  23,  24,  25,  26,  27,  28,  29,  30,  31,  32
  33,  34,  35,  36,  37,  38,  39,  40,  41,  42,  43,  44,  45,  46,  47,  48
  49,  50,  51,  52,  53,  54,  55,  56,  57,  58,  59,  60,  61,  62,  63,  64
  65,  66,  67,  77,  78,  88,  89,  99, 100, 110, 111, 112, 113, 114, 115, 116
 117, 118, 119, 120, 121, 122, 132, 133, 143, 144, 154, 155, 165, 166, 167, 168
 169, 170, 171, 172, 173, 174, 175, 176, 177, 187, 188, 198, 199, 209, 210, 220
 221, 222, 223, 224, 225, 226, 227, 228, 229, 230, 231, 232, 242, 243, 253, 254
 264, 265, 275, 276, 277, 278, 279, 280, 281, 282, 283, 284, 285, 286, 287, 297
 298, 308, 309, 319, 320, 330, 331, 332, 333, 334, 335, 336, 337, 338, 339, 340
 341, 342, 352, 353, 363, 364, 374, 375, 385, 386, 387, 388, 389, 390, 391, 392
 393, 394, 395, 396, 397, 407, 408, 418, 419, 429, 430, 440, 441, 442, 443, 444
 445, 446, 447, 448, 449, 450, 451, 452, 462, 463, 473, 474, 484, 485, 495, 496
 497, 498, 499, 500, 501, 502, 503, 504, 505, 506, 507, 517, 518, 528, 529, 539
 540, 550, 551, 552, 553, 554, 555, 556, 557, 558, 559, 560, 561, 562, 563, 564
 565, 566, 567, 568, 569, 570, 571, 572, 573, 574, 575, 576, 577, 578, 579, 580
 581, 582, 583, 584, 585, 586, 587, 588, 589, 590, 591, 592, 593, 594, 595, 596
 597, 598, 599, 600, 601, 602, 603, 604, 605
*Nset, nset=_PickedSet519, internal, instance=Part-middle-1
   1,   2,   3,   4,  10,  11,  13,  14,  17,  18,  19,  20,  21,  22,  23,  24
  25,  26,  27,  28,  29,  30,  31,  32,  84,  85,  86,  87,  88,  89, 103, 104
 105, 106, 107, 108, 117, 118, 119, 120, 121, 122, 123, 124, 125, 126, 127, 128
 129, 130, 131, 132, 161, 162, 163, 164, 165, 166, 167, 168, 169, 170, 171, 172
 185, 186, 187, 188, 189, 190, 191, 192, 193, 194, 195, 196, 417, 418, 419, 420
 421, 422, 423, 424, 425, 426, 427, 428, 443, 444, 445, 446, 447, 448, 449, 450
 451, 452, 453, 454, 565, 566, 567, 568, 569, 570, 571, 572, 573, 574, 575, 576
*Nset, nset=_PickedSet519, internal, instance=Part-top-1
   1,   2,   3,   4,   5,   6,   7,   8,   9,  10,  11,  12,  13,  14,  15,  16
  17,  18,  19,  20,  21,  22,  23,  24,  25,  26,  27,  28,  29,  30,  31,  32
  33,  34,  35,  36,  37,  38,  39,  40,  41,  42,  43,  44,  45,  46,  54,  55
  63,  64,  72,  73,  81,  82,  83,  84,  85,  86,  87,  88,  89,  90,  91,  99
 100, 108, 109, 117, 118, 126, 127, 128, 129, 130, 131, 132, 133, 134, 135, 136
 144, 145, 153, 154, 162, 163, 171, 172, 173, 174, 175, 176, 177, 178, 179, 180
 181, 189, 190, 198, 199, 207, 208, 216, 217, 218, 219, 220, 221, 222, 223, 224
 225, 226, 234, 235, 243, 244, 252, 253, 261, 262, 263, 264, 265, 266, 267, 268
 269, 270, 271, 279, 280, 288, 289, 297, 298, 306, 307, 308, 309, 310, 311, 312
 313, 314, 315, 316, 324, 325, 333, 334, 342, 343, 351, 352, 353, 354, 355, 356
 357, 358, 359, 360, 361, 362, 363, 364, 365, 366, 367, 368, 369, 370, 371, 372
 373, 374, 375, 376, 377, 378, 379, 380, 381, 382, 383, 384, 385, 386, 387, 388
 389, 390, 391, 392, 393, 394, 395, 396, 397, 398, 399, 400, 401, 402, 403, 404
 405,
*Elset, elset=_PickedSet519, internal, instance=Part-bottom-1
   1,   2,   3,   4,   5,   6,   7,   8,   9,  10,  11,  12,  13,  14,  15,  16
  17,  18,  19,  20,  21,  22,  23,  24,  25,  26,  27,  28,  29,  30,  31,  32
  33,  34,  35,  36,  37,  38,  39,  40,  41,  42,  43,  44,  45,  46,  47,  48
  49,  50,  51,  60,  61,  70,  71,  80,  81,  82,  83,  84,  85,  86,  87,  88
  89,  90,  91, 100, 101, 110, 111, 120, 121, 122, 123, 124, 125, 126, 127, 128
 129, 130, 131, 140, 141, 150, 151, 160, 161, 162, 163, 164, 165, 166, 167, 168
 169, 170, 171, 180, 181, 190, 191, 200, 201, 202, 203, 204, 205, 206, 207, 208
 209, 210, 211, 220, 221, 230, 231, 240, 241, 242, 243, 244, 245, 246, 247, 248
 249, 250, 251, 260, 261, 270, 271, 280, 281, 282, 283, 284, 285, 286, 287, 288
 289, 290, 291, 300, 301, 310, 311, 320, 321, 322, 323, 324, 325, 326, 327, 328
 329, 330, 331, 340, 341, 350, 351, 360, 361, 362, 363, 364, 365, 366, 367, 368
 369, 370, 371, 372, 373, 374, 375, 376, 377, 378, 379, 380, 381, 382, 383, 384
 385, 386, 387, 388, 389, 390, 391, 392, 393, 394, 395, 396, 397, 398, 399, 400
*Elset, elset=_PickedSet519, internal, instance=Part-middle-1
```

```
   1,   2,   3,   4,   5,   6,   7,   8,   9,  10,  11,  12,  13,  14,  15,  16
  17,  18,  19,  20,  21, 176, 184, 192, 200, 208, 216, 224, 232, 240, 248, 256
 264, 272, 280, 288, 296, 304, 312, 320, 328, 336, 337, 338, 339, 340, 341, 342
 343, 344, 345, 346, 347, 348, 349, 350, 351, 352, 353, 354, 355, 356, 357, 505
 506, 507, 508, 509, 510, 511, 512, 513, 514, 515, 516, 517, 518, 519, 520, 521
 522, 523, 524, 525
*Elset, elset=_PickedSet519, internal, instance=Part-top-1
   1,   2,   3,   4,   5,   6,   7,   8,   9,  10,  11,  12,  13,  14,  15,  16
  17,  18,  19,  20,  21,  22,  23,  24,  25,  26,  27,  28,  29,  30,  31,  32
  33,  40,  41,  48,  49,  56,  57,  58,  59,  60,  61,  62,  63,  64,  65,  72
  73,  80,  81,  88,  89,  90,  91,  92,  93,  94,  95,  96,  97, 104, 105, 112
 113, 120, 121, 122, 123, 124, 125, 126, 127, 128, 129, 136, 137, 144, 145, 152
 153, 154, 155, 156, 157, 158, 159, 160, 161, 168, 169, 176, 177, 184, 185, 186
 187, 188, 189, 190, 191, 192, 193, 200, 201, 208, 209, 216, 217, 218, 219, 220
 221, 222, 223, 224, 225, 226, 227, 228, 229, 230, 231, 232, 233, 234, 235, 236
 237, 238, 239, 240, 241, 242, 243, 244, 245, 246, 247, 248, 249, 250, 251, 252
 253, 254, 255, 256
*Nset, nset=_PickedSet520, internal, instance=Part-rigid-1
 13536,
*Nset, nset=Set-rigid, instance=Part-rigid-1
 13536,
*Nset, nset=_PickedSet540, internal, instance=Part-rigid-1
   19,   20,   25,   26,  663,  664,  665,  666,  667,  668,  669,  670,  671,
672,  673,  674
  675,  676,  677,  678,  679,  680,  681,  682,  683,  684,  685,  686,  687,
746,  747,  748
  749,  750,  751,  752,  753,  754,  755,  756,  757,  758,  759,  760,  761,
762,  763,  764
                                  :
                                  :
                                  :
 8769, 8770, 8771, 8772, 8773, 8774, 8775, 8776, 8777, 8778, 8779, 8780, 8781,
8782, 8783, 8784
 8785, 8786, 8787, 8788, 8789, 8790, 8791, 8792, 8793, 8794, 8821, 8822, 8823,
8824, 8825, 8826
 8827, 8828, 8829, 8830, 8831, 8832, 8833, 8834, 8835, 8836, 8837, 8838, 8839,
8840, 8841, 8842
 8843, 8844, 8845, 8846
*Nset, nset=_PickedSet558, internal, instance=Part-rigid-1
 13536,
*Elset, elset=__PickedSurf493_S3, internal, instance=Part-rigid-1
 6897, 6898, 6899, 6900, 6901, 6902, 6903, 6904, 6905, 6906, 6907, 6908, 6909,
6910, 6911, 6912
 6913, 6914, 6915, 6916, 6917, 6918, 6919, 6920, 6921, 6922, 7001, 7002, 7003,
7004, 7005, 7006
 7007, 7008, 7009, 7010, 7011, 7012, 7013, 7014, 7015, 7016, 7017, 7018, 7019,
7020, 7021, 7022
 7023, 7024, 7025, 7026, 8873, 8874, 8875, 8876, 8877, 8878, 8879, 8880, 8881,
8882, 8883, 8884
 8885, 8886, 8887, 8888, 8889, 8890, 8891, 8892, 8893, 8894, 8895, 8896, 8897,
8898, 8977, 8978
 8979, 8980, 8981, 8982, 8983, 8984, 8985, 8986, 8987, 8988, 8989, 8990, 8991,
8992, 8993, 8994
 8995, 8996, 8997, 8998, 8999, 9000, 9001, 9002
*Elset, elset=__PickedSurf493_S5, internal, instance=Part-rigid-1
 7183, 7184, 7185, 7186, 7187, 7188, 7189, 7190, 7191, 7192, 7193, 7194, 7195,
7196, 7197, 7198
```

```
 7199, 7200, 7201, 7202, 7203, 7204, 7205, 7206, 7207, 7208, 7287, 7288, 7289,
7290, 7291, 7292
 7293, 7294, 7295, 7296, 7297, 7298, 7299, 7300, 7301, 7302, 7303, 7304, 7305,
7306, 7307, 7308
 7309, 7310, 7311, 7312, 7391, 7392, 7393, 7394, 7395, 7396, 7397, 7398, 7399,
7400, 7401, 7402
                                  :
                                  :
                                  :
 8661, 8662, 8663, 8664, 8691, 8692, 8693, 8694, 8695, 8696, 8697, 8698, 8699,
8700, 8701, 8702
 8703, 8704, 8705, 8706, 8707, 8708, 8709, 8710, 8711, 8712, 8713, 8714, 8715,
8716, 8743, 8744
 8745, 8746, 8747, 8748, 8749, 8750, 8751, 8752, 8753, 8754, 8755, 8756, 8757,
8758, 8759, 8760
 8761, 8762, 8763, 8764, 8765, 8766, 8767, 8768, 8795, 8796, 8797, 8798, 8799,
8800, 8801, 8802
 8803, 8804, 8805, 8806, 8807, 8808, 8809, 8810, 8811, 8812, 8813, 8814, 8815,
8816, 8817, 8818
 8819, 8820, 8847, 8848, 8849, 8850, 8851, 8852, 8853, 8854, 8855, 8856, 8857,
8858, 8859, 8860
 8861, 8862, 8863, 8864, 8865, 8866, 8867, 8868, 8869, 8870, 8871, 8872
*Elset, elset=__PickedSurf493_S1, internal, instance=Part-rigid-1, generate
    1,  1724,     1
*Surface, type=ELEMENT, name=_PickedSurf493, internal
__PickedSurf493_S3, S3
__PickedSurf493_S5, S5
__PickedSurf493_S1, S1
*Elset, elset=__PickedSurf495_S3, internal, instance=Part-inner1-1
     1,     2,     3,     4,     5,     6,     7,     8,     9,    10,    11,
12,    13,    14,    15,    16
    17,    18,    19,    20,    21,    22,    23,    24,    25,    26,    27,
28,    29,    30,    31,    32
    33,    34,    35,    36,    37,    38,    39,    40,    41,    42,    43,
44,    45,    46,    47,    48
    49,    50,   951,   952,   953,   954,   955,   956,   957,   958,   959,
960,   961,   962,   963,   964
                                  :
                                  :
                                  :
 10369, 10370, 10371, 10372, 10373, 10374, 10375, 10376, 10377, 10378, 10379,
10380, 10381, 10382, 10383, 10384
 10385, 10386, 10387, 10388, 10389, 10390, 10391, 10392, 10393, 10394, 10395,
10396, 10397, 10398, 10399, 10400
 10401, 10402, 10403, 10404, 10405, 10406, 10407, 10408, 10409, 10410, 10411,
10412, 10413, 10414, 10415, 10416
 10417, 10418, 10419, 10420, 10421, 10422, 10423, 10424, 10425, 10426, 10427,
10428, 10429, 10430, 10431, 10432
*Surface, type=ELEMENT, name=_PickedSurf496, internal
__PickedSurf496_S5, S5
__PickedSurf496_S3, S3
__PickedSurf496_S2, S2
*Elset, elset=__PickedSurf497_S5, internal, instance=Part-inner2-1
   901,   902,   903,   904,   905,   906,   907,   908,   909,   910,   911,
912,   913,   914,   915,   916
   917,   918,   919,   920,   921,   922,   923,   924,   925,   926,   927,
928,   929,   930,   931,   932
```

```
   933,   934,   935,   936,   937,   938,   939,   940,   941,   942,   943,
944,   945,   946,   947,   948
                                  :
                                  :
                                  :
 47465, 47466, 47467, 47468, 47469, 47470, 47471, 47472, 47473, 47474, 47475,
47476, 47477, 47478, 47479, 47480
 47481, 47482, 47483, 47484, 47485, 47486, 47487, 47488, 47489, 47490, 47491,
47492, 47493, 47494, 47495, 47496
 47497, 47498, 47499, 47500
*Surface, type=ELEMENT, name=_PickedSurf497, internal
__PickedSurf497_S5, S5
*Elset, elset=__PickedSurf501_S1, internal, instance=Part-middle-1
 148, 149, 150, 151, 152, 153, 154, 155, 156, 157, 158, 159, 160, 161, 162, 163
 164, 165, 166, 167, 168, 484, 485, 486, 487, 488, 489, 490, 491, 492, 493, 494
 495, 496, 497, 498, 499, 500, 501, 502, 503, 504, 652, 653, 654, 655, 656, 657
 658, 659, 660, 661, 662, 663, 664, 665, 666, 667, 668, 669, 670, 671, 672
*Elset, elset=__PickedSurf501_S6, internal, instance=Part-middle-1, generate
 169,  329,    8
*Surface, type=ELEMENT, name=_PickedSurf501, internal
__PickedSurf501_S1, S1
__PickedSurf501_S6, S6
*Elset, elset=__PickedSurf502_S1, internal, instance=Part-inner1-1, generate
 46551,  47500,      1
*Elset, elset=__PickedSurf502_S1, internal, instance=Part-inner2-1, generate
 46551,  47500,      1
*Elset, elset=__PickedSurf502_S6, internal, instance=Part-inner1-1, generate
     1,  47451,     50
*Elset, elset=__PickedSurf502_S6, internal, instance=Part-inner2-1, generate
     1,  47451,     50
*Elset, elset=__PickedSurf502_S6, internal, instance=Part-rigid-1
    1,   12,   23,   34,   45,   56,   67,   78,   89,  100,  111,  122,  133,
144,  155,  166
  177,  188,  199,  210,  221,  232,  243,  254,  265,  276,  287,  298,  309,
320,  331,  342
  353,  364,  375,  386,  397,  408,  419,  430,  478,  526,  574,  622,  670,
718,  766,  814
  862,  910, 1725, 1736, 1747, 1758, 1769, 1780, 1791, 1802, 1813, 1824, 1835,
1846, 1857, 1868
                                  :
                                  :
                                  :
 3757, 3768, 3779, 3790, 3801, 3812, 3823, 3834, 3845, 3856, 3867, 3878, 3926,
3974, 4022, 4070
 4118, 4166, 4214, 4262, 4310, 4358, 5173, 5184, 5195, 5206, 5217, 5228, 5239,
5250, 5261, 5272
 5283, 5294, 5305, 5316, 5327, 5338, 5349, 5360, 5371, 5382, 5393, 5404, 5415,
5426, 5437, 5448
 5459, 5470, 5481, 5492, 5503, 5514, 5525, 5536, 5547, 5558, 5569, 5580, 5591,
5602, 5650, 5698
 5746, 5794, 5842, 5890, 5938, 5986, 6034, 6082
*Elset, elset=__PickedSurf502_S2, internal, instance=Part-inner1-1, generate
   1,  950,    1
*Elset, elset=__PickedSurf502_S2, internal, instance=Part-inner2-1, generate
   1,  950,    1
*Elset, elset=__PickedSurf502_S4, internal, instance=Part-inner1-1, generate
    50,  47500,     50
```

```
*Elset, elset=__PickedSurf502_S4, internal, instance=Part-inner2-1, generate
    50,  47500,     50
*Elset, elset=__PickedSurf502_S4, internal, instance=Part-rigid-1
  477,  525,  573,  621,  669,  717,  765,  813,  861,  909,  957,  970,  983,
996, 1009, 1022
 1035, 1048, 1061, 1074, 1087, 1100, 1113, 1126, 1139, 1152, 1165, 1178, 1191,
1204, 1217, 1230
 1243, 1256, 1269, 1282, 1295, 1306, 1317, 1328, 1339, 1350, 1361, 1372, 1383,
1394, 1405, 1416
 1427, 1438, 1449, 1460, 1471, 1482, 1493, 1504, 1515, 1526, 1537, 1548, 1559,
1570, 1581, 1592
                                  :
                                  :
                                  :
 6363, 6376, 6389, 6402, 6415, 6428, 6441, 6454, 6467, 6478, 6489, 6500, 6511,
6522, 6533, 6544
 6555, 6566, 6577, 6588, 6599, 6610, 6621, 6632, 6643, 6654, 6665, 6676, 6687,
6698, 6709, 6720
 6731, 6742, 6753, 6764, 6775, 6786, 6797, 6808, 6819, 6830, 6841, 6852, 6863,
6874, 6885, 6896
*Elset, elset=__PickedSurf502_S3, internal, instance=Part-rigid-1
  419,  420,  421,  422,  423,  424,  425,  426,  427,  428,  429,  910,  911,
912,  913,  914
  915,  916,  917,  918,  919,  920,  921,  922,  923,  924,  925,  926,  927,
928,  929,  930
  931,  932,  933,  934,  935,  936,  937,  938,  939,  940,  941,  942,  943,
944,  945,  946
  947,  948,  949,  950,  951,  952,  953,  954,  955,  956,  957, 1714, 1715,
1716, 1717, 1718
                                  :
                                  :
                                  :
 4399, 4400, 4401, 4402, 4403, 4404, 4405, 5162, 5163, 5164, 5165, 5166, 5167,
5168, 5169, 5170
 5171, 5172, 5591, 5592, 5593, 5594, 5595, 5596, 5597, 5598, 5599, 5600, 5601,
6082, 6083, 6084
 6085, 6086, 6087, 6088, 6089, 6090, 6091, 6092, 6093, 6094, 6095, 6096, 6097,
6098, 6099, 6100
 6101, 6102, 6103, 6104, 6105, 6106, 6107, 6108, 6109, 6110, 6111, 6112, 6113,
6114, 6115, 6116
 6117, 6118, 6119, 6120, 6121, 6122, 6123, 6124, 6125, 6126, 6127, 6128, 6129,
6886, 6887, 6888
 6889, 6890, 6891, 6892, 6893, 6894, 6895, 6896
*Surface, type=ELEMENT, name=_PickedSurf502, internal
__PickedSurf502_S1, S1
__PickedSurf502_S6, S6
__PickedSurf502_S2, S2
__PickedSurf502_S4, S4
__PickedSurf502_S3, S3
*Elset, elset=__PickedSurf508_S5, internal, instance=Part-bottom-1
  31,  32,  33,  34,  35,  36,  37,  38,  39,  40,  71,  72,  73,  74,  75,  76
  77,  78,  79,  80, 111, 112, 113, 114, 115, 116, 117, 118, 119, 120, 151, 152
 153, 154, 155, 156, 157, 158, 159, 160, 191, 192, 193, 194, 195, 196, 197, 198
 199, 200, 231, 232, 233, 234, 235, 236, 237, 238, 239, 240, 271, 272, 273, 274
 275, 276, 277, 278, 279, 280, 311, 312, 313, 314, 315, 316, 317, 318, 319, 320
 351, 352, 353, 354, 355, 356, 357, 358, 359, 360, 391, 392, 393, 394, 395, 396
 397, 398, 399, 400
```

```
*Surface, type=ELEMENT, name=_PickedSurf508, internal
__PickedSurf508_S5, S5
*Elset, elset=__PickedSurf509_S3, internal, instance=Part-inner2-1
     1,     2,     3,     4,     5,     6,     7,     8,     9,    10,    11,
12,    13,    14,    15,    16
    17,    18,    19,    20,    21,    22,    23,    24,    25,    26,    27,
28,    29,    30,    31,    32
    33,    34,    35,    36,    37,    38,    39,    40,    41,    42,    43,
44,    45,    46,    47,    48
    49,    50,   951,   952,   953,   954,   955,   956,   957,   958,   959,
960,   961,   962,   963,   964
   965,   966,   967,   968,   969,   970,   971,   972,   973,   974,   975,
976,   977,   978,   979,   980
   981,   982,   983,   984,   985,   986,   987,   988,   989,   990,   991,
992,   993,   994,   995,   996
                                :
                                :
                                :
 45633, 45634, 45635, 45636, 45637, 45638, 45639, 45640, 45641, 45642, 45643,
45644, 45645, 45646, 45647, 45648
 45649, 45650, 46551, 46552, 46553, 46554, 46555, 46556, 46557, 46558, 46559,
46560, 46561, 46562, 46563, 46564
 46565, 46566, 46567, 46568, 46569, 46570, 46571, 46572, 46573, 46574, 46575,
46576, 46577, 46578, 46579, 46580
 46581, 46582, 46583, 46584, 46585, 46586, 46587, 46588, 46589, 46590, 46591,
46592, 46593, 46594, 46595, 46596
 46597, 46598, 46599, 46600
*Elset, elset=__PickedSurf509_S3, internal, instance=Part-middle-1
   1,   2,   3,   4,   5,   6,   7,  22,  23,  24,  25,  26,  27,  28,  43,  44
  45,  46,  47,  48,  49,  64,  65,  66,  67,  68,  69,  70,  85,  86,  87,  88
  89,  90,  91, 106, 107, 108, 109, 110, 111, 112, 127, 128, 129, 130, 131, 132
 133, 148, 149, 150, 151, 152, 153, 154, 337, 338, 339, 340, 341, 342, 343, 358
 359, 360, 361, 362, 363, 364, 379, 380, 381, 382, 383, 384, 385, 400, 401, 402
 403, 404, 405, 406, 421, 422, 423, 424, 425, 426, 427, 442, 443, 444, 445, 446
 447, 448, 463, 464, 465, 466, 467, 468, 469, 484, 485, 486, 487, 488, 489, 490
 505, 506, 507, 508, 509, 510, 511, 526, 527, 528, 529, 530, 531, 532, 547, 548
 549, 550, 551, 552, 553, 568, 569, 570, 571, 572, 573, 574, 589, 590, 591, 592
 593, 594, 595, 610, 611, 612, 613, 614, 615, 616, 631, 632, 633, 634, 635, 636
 637, 652, 653, 654, 655, 656, 657, 658
*Elset, elset=__PickedSurf509_S2, internal, instance=Part-middle-1, generate
 169,  224,    1
*Surface, type=ELEMENT, name=_PickedSurf509, internal
__PickedSurf509_S3, S3
__PickedSurf509_S2, S2
*Elset, elset=__PickedSurf511_S3, internal, instance=Part-top-1
   1,   2,   3,   4,   5,   6,   7,   8,  33,  34,  35,  36,  37,  38,  39,  40
  65,  66,  67,  68,  69,  70,  71,  72,  97,  98,  99, 100, 101, 102, 103, 104
 129, 130, 131, 132, 133, 134, 135, 136, 161, 162, 163, 164, 165, 166, 167, 168
 193, 194, 195, 196, 197, 198, 199, 200, 225, 226, 227, 228, 229, 230, 231, 232
*Surface, type=ELEMENT, name=_PickedSurf511, internal
__PickedSurf511_S3, S3
*Elset, elset=__PickedSurf512_S5, internal, instance=Part-inner1-1
   901,   902,   903,   904,   905,   906,   907,   908,   909,   910,   911,
912,   913,   914,   915,   916
   917,   918,   919,   920,   921,   922,   923,   924,   925,   926,   927,
928,   929,   930,   931,   932
   933,   934,   935,   936,   937,   938,   939,   940,   941,   942,   943,
944,   945,   946,   947,   948
```

```
   949,   950,  1851,  1852,  1853,  1854,  1855,  1856,  1857,  1858,  1859,
1860,  1861,  1862,  1863,  1864
  1865,  1866,  1867,  1868,  1869,  1870,  1871,  1872,  1873,  1874,  1875,
1876,  1877,  1878,  1879,  1880
                                  :
                                  :
                                  :
 46549, 46550, 47451, 47452, 47453, 47454, 47455, 47456, 47457, 47458, 47459,
47460, 47461, 47462, 47463, 47464
 47465, 47466, 47467, 47468, 47469, 47470, 47471, 47472, 47473, 47474, 47475,
47476, 47477, 47478, 47479, 47480
 47481, 47482, 47483, 47484, 47485, 47486, 47487, 47488, 47489, 47490, 47491,
47492, 47493, 47494, 47495, 47496
 47497, 47498, 47499, 47500
*Elset, elset=__PickedSurf512_S5, internal, instance=Part-middle-1
  15,  16,  17,  18,  19,  20,  21,  36,  37,  38,  39,  40,  41,  42,  57,  58
  59,  60,  61,  62,  63,  78,  79,  80,  81,  82,  83,  84,  99, 100, 101, 102
 103, 104, 105, 120, 121, 122, 123, 124, 125, 126, 141, 142, 143, 144, 145, 146
 147, 162, 163, 164, 165, 166, 167, 168, 351, 352, 353, 354, 355, 356, 357, 372
 373, 374, 375, 376, 377, 378, 393, 394, 395, 396, 397, 398, 399, 414, 415, 416
 417, 418, 419, 420, 435, 436, 437, 438, 439, 440, 441, 456, 457, 458, 459, 460
 461, 462, 477, 478, 479, 480, 481, 482, 483, 498, 499, 500, 501, 502, 503, 504
 519, 520, 521, 522, 523, 524, 525, 540, 541, 542, 543, 544, 545, 546, 561, 562
 563, 564, 565, 566, 567, 582, 583, 584, 585, 586, 587, 588, 603, 604, 605, 606
 607, 608, 609, 624, 625, 626, 627, 628, 629, 630, 645, 646, 647, 648, 649, 650
 651, 666, 667, 668, 669, 670, 671, 672
*Elset, elset=__PickedSurf512_S1, internal, instance=Part-middle-1, generate
 281,  336,    1
*Surface, type=ELEMENT, name=_PickedSurf512, internal
__PickedSurf512_S5, S5
__PickedSurf512_S1, S1
** Constraint: Constraint-5
*Tie, name=Constraint-5, adjust=yes
_PickedSurf509, _PickedSurf508
** Constraint: Constraint-6
*Tie, name=Constraint-6, adjust=yes
_PickedSurf512, _PickedSurf511
** Constraint: Constraint-i-m
*Tie, name=Constraint-i-m, adjust=yes
_PickedSurf502, _PickedSurf501
** Constraint: Constraint-r-i1
*Tie, name=Constraint-r-i1, adjust=yes
_PickedSurf495, _PickedSurf493
** Constraint: Constraint-r-i2
*Tie, name=Constraint-r-i2, adjust=yes
_PickedSurf497, _PickedSurf496
** Constraint: Constraint-rigid
*Rigid Body, ref node=_PickedSet491, tie nset=_PickedSet540
*End Assembly
**
** ELEMENT CONTROLS
**
*Section Controls, name=EC-1, hourglass=RELAX STIFFNESS
1., 1., 1.
**
** MATERIALS
**
*Material, name=Material-soil
```

```
*Elastic
4500., 0.49
*Plastic
10.,0.
*Material, name=Material-soil2
*Elastic
4500., 0.49
*Plastic
5.,0.
**
** INTERACTION PROPERTIES
**
*Surface Interaction, name=IntProp-1
1.,
*Friction, rough
** ----------------------------------------------------------------
**
** STEP: Step-1
**
*Step, name=Step-1
*Static
1., 1., 1e-05, 1.
**
** BOUNDARY CONDITIONS
**
** Name: BC-1 Type: Symmetry/Antisymmetry/Encastre
*Boundary
_PickedSet519, ENCASTRE
** Name: BC-2 Type: Displacement/Rotation
*Boundary
_PickedSet520, 1, 1, 0.3
**
** LOADS
**
** Name: Load-1   Type: Concentrated force
*Cload
_PickedSet558, 3, 570
**
** OUTPUT REQUESTS
**
*Restart, write, frequency=1
**
** FIELD OUTPUT: F-Output-1
**
*Output, field
*Node Output
RF,
*Element Output
PE, S, PEEQ
**
** HISTORY OUTPUT: H-Output-1
**
*Output, history
*Node Output, nset=Set-rigid
RF1, RF2, RF3, RM1, RM2, RM3
*El Print, freq=1
*Node Print, freq=1, nset=Set-rigid, totals=yes
RF,
U3, UR2, UR3,
*End Step
```

VITA

Ming Yang was born in Yuexi, Anhui Province, China. He received his B.S. degree and M.S. degree in geoengineering from Southwest Jiaotong University, Chengdu, China in 1999 and 2002, respectively. He came to the United States in 2003 and received his second M.S. degree in materials engineering from University of Illinois at Chicago in 2005. Ming Yang may be reached at the following address: Department of Civil Engineering, Texas A&M University, MS 3136, College Station, TX, 77843.